1

The Realm of Nanoscience and Molecular Engineering

1.1 Nanoscience and Molecular Engineering

Nanoscience is most ordinarily defined by its scale, the nanometer that is equivalent to 10^{-9} m, or a thousandth of a micrometer. As illustrated in Figure 1.1, the nanometer is multiple times larger than the smallest distance between atoms in crystalline materials, matches roughly the smallest molecular distances in self-assemblies, and is approximately ten thousand times smaller than the thickness of a human hair. Practical material systems, devices, and technologies based on nanoscience are coined *Nanotechnology*.

Certainly, size plays a crucial role in various practical applications related to the nanoscale. But there is more to be said about this technology and its underlying science. Nanoscience and nanotechnology thrive on constraints that alter the boundary conditions of the macro world we are so accustomed to and present us with a world of wonders and surprises. The two employ and highlight, in particular, material interfaces and dimensionally constrained systems that alter molecular and atomistic arrangements and enhance fluctuations that affect the system equilibrium. We realize that most of our current technologies heavily rely on phenomenological bulk properties, often ignoring the fine subtleties that could be gained by involving interfaces in our designs to enhance or alter material properties.

In our world, material properties are important for several reasons, including:

- ensuring the mechanical integrity of devices;
- enabling and facilitating processes to run, such as chemical reactions;
- providing adequate conduction properties for particles and energy (heat) transport;
- customizing interaction interfaces between electromagnetic (EM) radiation and material transport systems toward energy production and communication, among others.

The processes developed to modify the bulk properties of materials have encompassed both mechanical and chemical methods, besides the blending of different materials. Steel, one of humanity's oldest engineered materials, is produced through techniques such as mechanical folding, compressing, and stretching, while simultaneously incorporating carbon into the iron's crystal lattice and removing oxygen through heating and stress. While the chemistry involved in metalworking was largely undertaken unintentionally in ancient times, these trial-and-error methods have been refined over the centuries, leading to a

Principles of Nanoscience and Molecular Engineering, First Edition. René M. Overney.

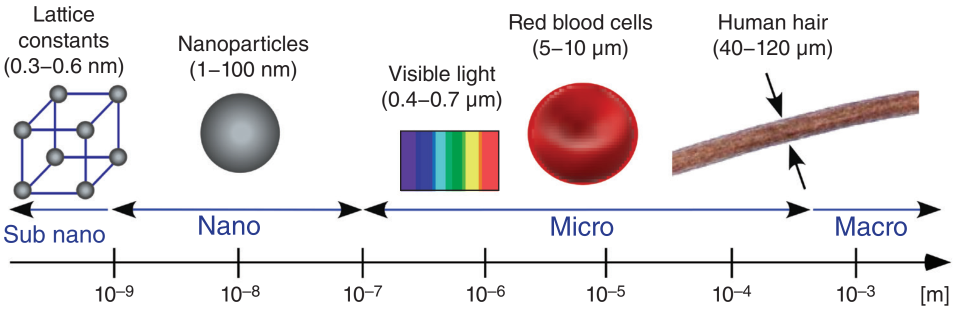

Figure 1.1 The nanoscale, microscale and macroscale. The significant difference between the nanoscale and its two larger cousins is that it exhibits deviating physical properties for condensed materials.

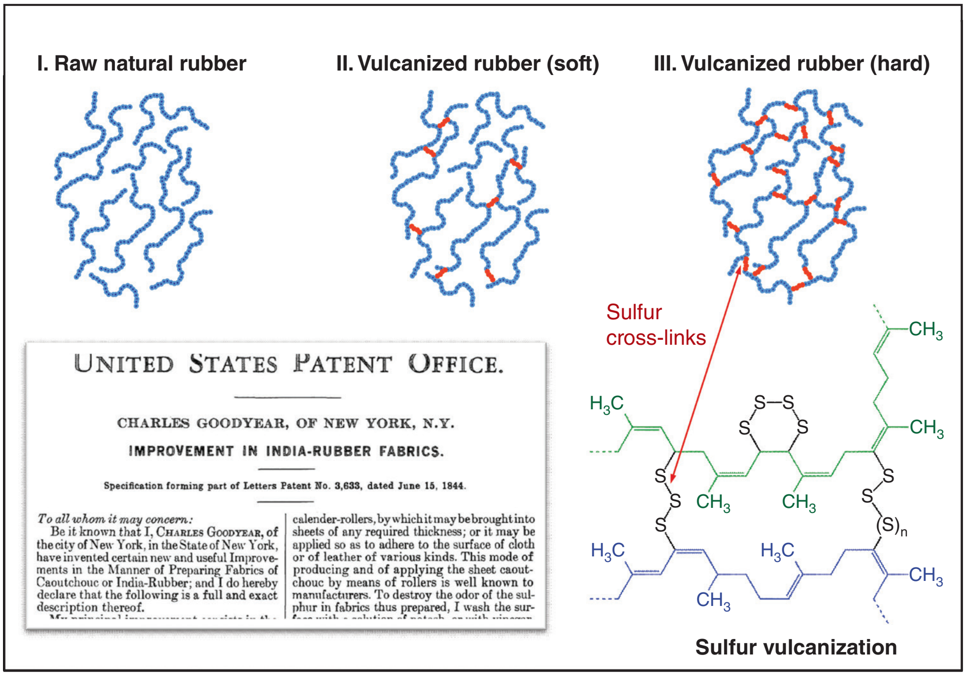

UNITED STATES PATENT OFFICE.

CHARLES GOODYEAR, OF NEW YORK, N.Y.

IMPROVEMENT IN INDIA-RUBBER FABRICS.

Specification forming part of Letters Patent No. 3,633, dated June 15, 1844.

To all whom it may concern:

Be it known that I, Charles Goodyear, of the city of New York, in the State of New York, have invented certain new and useful Improvements in the Manner of Preparing Fabrics of Caoutchouc or India-Rubber; and I do hereby declare that the following is a full and exact description thereof.

calender-rollers, by which it may be brought into sheets of any required thickness; or it may be applied so as to adhere to the surface of cloth or of leather of various kinds. This mode of producing and of applying the sheet caoutchouc by means of rollers is well known to manufacturers. To destroy the odor of the sulphur in fabrics thus prepared, I wash the sur-

Figure 1.2 Trial-and-error discovery: Sulfur vulcanization of natural rubber (patented by Charles Goodyear in 1844). During vulcanization, chemical cross-links are formed between individual polymer chains. The degree of cross-linking density determines if the rubber is soft or hard.

deeper and more fundamental understanding of the processes that occur at the atomistic and molecular levels. Thus, while Charles Goodyear invented the vulcanization process of rubber in the middle of the 19th century, a later generation of scientists recognized the true nature of the process, as chemical cross-linking between the polymer molecules, as sketched in Figure 1.2.

With a fundamental understanding of material engineering, molecules with chemical linkers could be specifically synthesized to bring forward novel materials with properties tailored toward unique processes. This molecule-specific rational approach toward engineering is coined these days as *Molecular Engineering*. Thus, while molecular engineering deals with the rational design of functional molecules, nanoscience focuses on the fundamental understanding of the properties of material if confined to the nanoscale. Even if the two fields are not necessarily inclusive, their sweet spot lies in their shared realm, where we have control over the molecular building blocks, as well as a fundamental understanding of their collective properties under regulated conditions that go beyond far-field controls employed to bulk systems, such as externally applied electric fields, and concentration and temperature gradients.

To illustrate the shared realm between nanoscience and molecular engineering, let us revisit the cross-linking example and assume that the organic polymer molecules are electric conductive and the linkers function as switches that can be activated or deactivated by an external electric field. Notably, there are distinct differences between a bulk system and a nanowire composed of these materials: (1) The nanowires contain significantly fewer switches compared to the bulk system, and (2) the polymer chain molecules in the bulk system exhibit a more isotropic distribution than those in the nanowire. Point (1) emphasizes how a low number of switches in nanowires can significantly affect overall conductivity. In contrast, point (2) focuses on the directional spinning process that aligns polymer chain molecules along the length of the wire, showcasing the transition of electric current flow from three dimensions to one dimension. As a result, we can anticipate a fundamental change in how electric current flows and how we can manipulate it, particularly when confined to the nanoscale. Given that the on-state and off-state of electric current represent a binary signal, it follows that significantly fewer electrons are needed in a nanowire compared to a bulk wire. By utilizing local fields that influence the switches differently along the wire, the nanowire could evolve into a complex network with extensive logical functionalities akin to those found in a computer. Therefore, our molecularly linked nanowire system has the potential to function as a versatile electric conductor with a wide array of applications, often described as a “smart” and “unique” nanosystem.

It is important to note that in this example, the intricate rational design of the molecular building blocks plays a crucial role in determining the functionality of the nanowires. Factors such as the polymer length, the placement of linkers at end groups or side groups, and the linker reversible strength of binding are of equal importance as the physical confinement in dimensions and local fields. The entire system design and its functionality employ both nanoscience and molecular engineering. Through nanoscience, we can tap into the physical world of lower dimensionalities and the quantum world, both substantially different from our macroscopic world. Meanwhile, molecular engineering allows us to move beyond the limitations inherent in traditional material engineering, which is often constrained by the properties of inorganic materials or by trial-and-error methods. Consequently, by combining these two fields, we can unlock future possibilities filled with remarkable innovations in novel materials and device technologies.

1.1.1 Trial-and-Error Approach and Deductive Rational Engineering

Common to both nanotechnology and molecular engineering is the development of novel materials and systems that are based on *deductive rational approach principles*, in contrast to *trial-and-error approach* methodologies. While everything we do involves atoms or molecules, it does not imply that we understand or control what we do on that scale. Take, for example, the process of brewing coffee: it darkens the water and imparts flavor through the interaction of small particles and molecules. However, this does not infer that it involves nanotechnology or molecular engineering. In fact, neither of the two scientific principles is applied in coffee making, which is rooted in the trial-and-error practices of our distant ancestors. This highlights that the advancements we have made over the centuries have largely been incremental, as they were trial-and-error based.

The development of nonsynthetic petroleum-based motor oils offers a more involved example than coffee brewing of incremental trial-and-error improvements over decades. These conventional petroleum oils require extensive distillation processes to remove waxes, sulfur, nitrogen, and oxygen compounds to generate the base stock to make useable lubricants. Many additives have been added to the base stock over the years. They provide lubricant oils with high boiling and low freezing points, high viscosity indices, improved thermal and hydraulic stabilities, demulsibility and corrosion insensitivity, and a high oxidation resistance. An example that required an incremental change of conventional motor oils involved the removal of zinc dialkyldithiophosphate (ZDDP), the most common zinc-based additive added primarily as an antiwear agent to reduce premature engine wear. In an attempt to remove ZDDP in the 1990s to minimize the phosphorous contents in petroleum oils, it was recognized that ZDDP's role was significantly more involved in the performance of the oil-based lubricant than anticipated, reaching beyond corrosion and oxidation protection and also affected the viscometry. Over the years, trial-and-error incremental improvements in the hundreds, if not thousands, brought forward lubricants of such high complexity that it was impossible to phantom the intricate contributions of the single components to the overall performance. Consequently, the trial-and-error approach for the further evolution of motor oils ran out of steam. A new, bottom-up approach was brought forward that culminated in the development of synthetic motor oils. Unlike their crude-oil-distilled and additive-loaded counterparts, synthetic oils are built up in the laboratory, starting with pure phases of molecules, such as ethylene. Instead of distilling down petroleum, crude oil is first broken down into pure chemical substances, followed by organic synthesis that brings forward larger molecules known as poly-α-olefins (PAO). PAO is the molecularly engineered base stock of synthetic motor oil. With the synthetic root, upcoming environmental requirements, such as the reduction in phosphorous compounds, could be quickly resolved, as the interplay between the chemical components was known.

Many more examples could be listed here that illuminate the shortcomings of products based on trial-and-error approaches. While products designed from the bottom up can be quicker and more effectively changed, the shortcomings of the deductive rational approach are typically initial costs and a high risk of failure during the original development phase. Table 1.1 provides a summary assessment of the *pros* and *cons* of the two engineering approaches. The trial-and-error approach applies to most current

Table 1.1 Fundamental approach toward materials/system engineering.

Trial-and-error approach	***Deductive rational approach***
Repeated, varied attempts, continued until success. Typically “hunch” based.	Extracted from a fundamental understanding of the atomic/molecular building blocks and collective phenomena.
PROS	**PROS**
• Relative fast success (fast to market) • Relative inexpensive (at first sight) • Low risk of success	• Highly tunable and flexible to changing requirements • Inexpensive toward further developments
CONS	**CONS**
• Limited fundamental insight • Increasingly expensive toward further development • Adjustment inflexible (e.g., in the removal of environmentally detrimental molecular components)	• Relative slow success (slow to market) • Very expensive (initially) • High risk of failure to deliver initial product
Applies to most current engineering developments of mature and emerging technologies.	More often involves nonengineering targeted fundamental discoveries that lead “after the fact” to products.

engineering developments of both mature and emerging technologies. The deductive rational approach, on the other hand, emerges either first as a curiosity without having the urgent need to find a solution for an engineering challenge, and thus, only leads later to products, or, if motivated by an engineering challenge driving a truly deductive research development from the bottom up. The deductive rational approach is slow to market but, if successful, revolutionary.

1.1.2 Combined Deductive Rational Engineering

One of the greatest triumphs of a deductive rational approach involving nanoscience and molecular engineering has been the development of the vaccine platform for SARS-CoV-2 (COVID-19) that took 2019/2020 less than a year to complete (including federal approval). It is one of the most extraordinary accomplishments of *Synthetic Biology* in combination with *Colloidal Sciences* that provided the sequence of the viral genome and an effective drug delivery system, respectively. Synthetic biology was instrumental in identifying and characterizing the molecular mechanisms that drive COVID-19,[1] which consequently led to the development of the crucial messenger ribonucleic acid (mRNA) precursors.[2] Once transcribed, the mRNA molecules were lipid-encapsulated to shield them from enzymatic

---

[1] COVID-19 stands for the coronavirus disease in 2019.

[2] mRNA is a type of single-stranded RNA that is involved in the production of proteins.

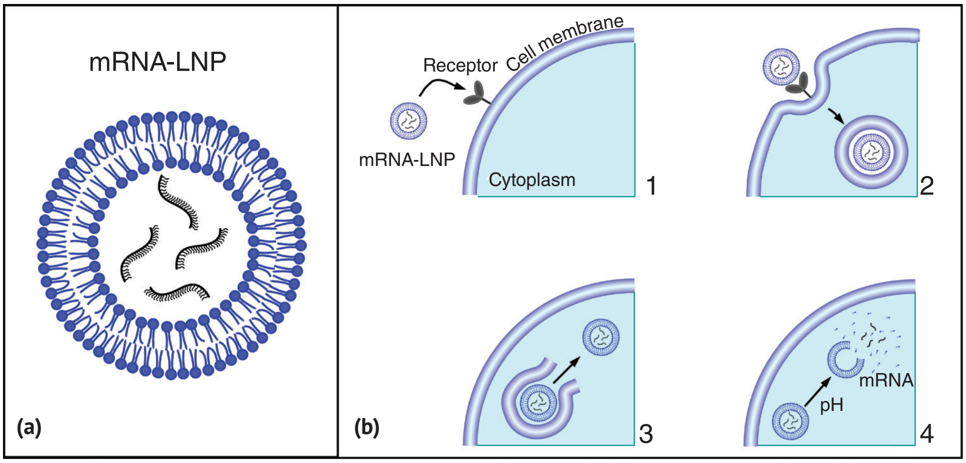

Figure 1.3 (a) LNP delivery system for mRNA payload. (b) 1–4 delivery steps of genetic mRNA material into the cell's cytoplasm, where it is converted into a functional protein.

degradation. With the use of lipid nanoparticles (LNPs), it was possible to transfer the mRNA molecules into the cell cytosol, as shown in Figure 1.3.

Briefly, when a nanoparticle is introduced into a cell's external milieu, it can interact with the outside of the plasma membrane, resulting in the nanoparticle entering the cell via a process called endocytosis, i.e., the invagination of its membrane to form a vacuole, which is pinched off to create membrane-bound vesicles that are routed within the cell to specific locations at which they open up and release the cargo, that is the mRNA-LNP. Once the lipid dissolves under the given pH conditions in the cytoplasm, the drug (here, mRNA) is released.

Clearly, the LNP molecular payload delivery process into living cells encompasses a highly deductive rational engineering methodology with many steps from encapsulation, environmental protection, storage prior to injection, initiation of endocytosis, routing to a specific location in the cell, to releasing the payload.

1.1.3 Perception of Our World – Apparent Unique Behaviors in Small Systems

While we live in a time in which we indulge ourselves with an atomistic and molecular perspective of matter, we are still very much stuck with perceptions derived from bulk material performances. This is self-evident on many occasions when we express our surprise about supposedly "unexpected" material behaviors. For instance, by analyzing the shear flow of ultrathin liquid films, we can observe lateral system response forces that exhibit apparent "unique" stick-slip behavior, while classically, we would expect from a liquid a monotonously constant drag force, as illustrated in Figure 1.4 by contrasting stick-slip to viscous sliding.

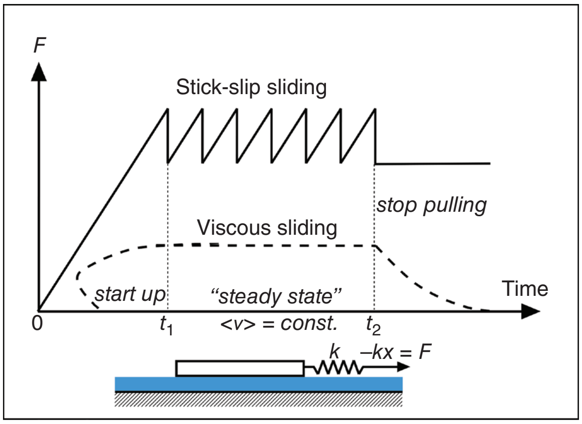

Figure 1.4 "Liquid" films are sheared, and the lateral response force F is measured. Viscous sliding of thick films reveals viscous sliding as expected. For ultrathin films (~1 nm thickness), stick-slip sliding is observed in the "steady-state" regime. The relative force location of the two sliding behaviors is arbitrarily chosen.

1.2 Properties in Lower Dimensionalities

The perception we hold concerning material behaviors is coined by our classical experiences, as well as our bulk phenomenological theories that often neglect interfaces, system inhomogeneities, and intrinsic relaxation times. Furthermore, we readily make steady-state and equilibrium assumptions. Considering the mentioned stick-slip behavior in ultrathin liquids, we hypothesize that we understand the nature of a "liquid" and a "solid." Searching in popular dictionaries, such as Webster's Encyclopedic Unabridged Dictionary, for definitions of these two terms, we find rather peculiar descriptions. For instance, one finds for "solids" the definition "having the interior completely filled up," and for "liquids" the description "composed of molecules, which move freely among themselves but do not tend to separate like those of gases." Thus, based on these definitions, we expect that the molecules in liquid films should be free to move in relation to each other and exhibit diffusive motions, as in a three-dimensional (3D) system at equilibrium. Furthermore, we assume constant drag resistances under a given external stress at steady state. With this perception in mind, we are in no condition to explain the observed stick-slip behavior in ultrathin films, a system constrained dimensionally.

Atoms and molecules at interfaces encounter a complex array of interaction forces, which also involve their surroundings. This situation leads to a reduction in degrees of freedom as we move from our 3D world to lower dimensions. Statistically, lower dimensional systems constrain the number of possible states or configurations for molecules, resulting in decreased entropy. Consequently, the pathways to equilibrium become more restricted, causing local minima or transient states to persist for longer durations. The implications of these phenomena are extensive.

In fluid-like systems,[3] the expected diffusive behavior may be disrupted. For example, while bulk diffusive transport typically involves a random walk scattering process, size-constrained systems, such as a one-dimensional (1D) wire, can exhibit ballistic transport, where the transport carriers move through the system with minimal scattering. Furthermore, the outcomes of natural laws or principles can also differ. For instance, according to Huygens' principle, which postulates that every point on a wave front acts as a source of secondary waves, sound waves that stop emanating demonstrate a well-defined cessation in three dimensions due to the exponential decay of the acoustic wave equation. In contrast, in two-dimensional (2D) systems, no abrupt termination is observed; instead, one experiences a slow logarithmic decay. This distinction has significant ramifications, as acoustic communication in a genuinely 2D environment proves to be considerably more challenging than in our 3D world, primarily due to the temporal overlap of information.

In nanoscience, we must consider two key aspects: the size dimension, which encompasses a range of length scales, and the space dimensionality, which reflects the degrees of freedom within the system. When examining the spatial dimension relevant to nanosystems, we expand our conventional 3D perspective to also include: (a) the zero-dimensional (0D) realm of atoms, small simple molecules, or quantum dots, (b) the 1D domain of long-chain molecules, nanofilaments, and nanotubes, and (c) the 2D space of surfaces, interfaces, and ultrathin films.

While further expansions of dimensionality are possible – particularly into fractal dimensions – we will restrict ourselves in our discussion to the realm of 0D, 1D, 2D, and 3D (bulk) dimensions. We perceive a system that is at least in one dimension size constrained to the nanoscale, a *nanosystem*.

In the following sections, we will explore how these nanoconstraints influence driving forces, transport phenomena, and material properties. We will begin with a simple narrative illustrating how peculiar our world can seem when viewed from a different dimensional perspective, while also reminding ourselves that our understanding of the world is fundamentally shaped by the three dimensions we inhabit.

1.2.1 Flatland – The Uniqueness of Lower Dimensionality

Since mathematicians have introduced us to many dimensions, it has been our desire to strive for more degrees of freedom while seemingly unsatisfied with the three dimensions we live in. Our pursuit of entertaining ourselves with fictions that escape our common senses is documented as early as 1884 in the satire "*Flatland: A Romance of Many Dimensions*" by Edwin A. Abbott (1952). While Abbott's work tries to introduce the reader to the concept of the multidimensional space beyond ours, it chooses fewer dimensions than three as a starting point. By doing so, Abbott came up with imaginary laws of nature that apply in one and two dimensions. Although these laws, for instance, explain how rain is experienced in two dimensions, are unrealistic, they impressively illustrate the mystery of lower dimensionalities.

---

[3] Applicable to molecular fluidic or electronic systems.

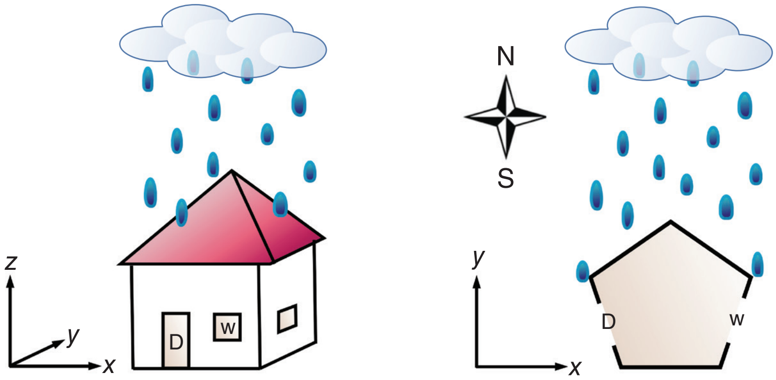

Figure 1.5 Orientation of houses, roofs, and openings in regards to the direction of rain in (*right*) our 3D world and (*left*) Flatland, Abbott's imaginary 2D world.

Let us inspect the example of rain in Abbott's *Flatland* a little further. In our 3D world, rain is coming down from the sky, and we protect our houses from getting wet inside with roofs. How about in Abbott's 2D world? Abbott artificially introduces cardinal directions to compensate for the lack of gravitation and requires rain to "fall" from North to South. Notice in Figure 1.5, the houses are arranged toward the North so that their openings are shaded from the rain. This example illustrates that driving forces, such as here the gravitational potential, familiar to us in our 3D macroscopic world can be put in question in lower dimensions. While Abbott insisted on rain by introducing an artificial cardinal direction that lacks any physical basis, he could have also easily argued that it never rains in *Flatland*, as there is no mass in two dimensions and, thus, no reason for gravitation. The loss but also the gain of driving forces (potentials), or more precisely their relative importance, explains some of the unique behavior of lower dimensional systems.

Thus, based on Abbott's imaginary world, when dealing with nanosystems, we must carefully assess the driving forces or potentials and how they can impact system properties. In the case of Abbott, the house constitutes the system, and its openings signify the relevant properties toward shielding the system from rain. In nanosystems, we consider the molecular structure and the translated mechanical, optical, thermal, and electronic material properties. Abbott's world deals with a single driving force that acts based on an imposed law on rain droplets. In nanosystems, we have to consider the transport involving a variety of corpuscular or non-corpuscular species on which forces are acting based on specific laws. We can assess the species transport in Abbott's world by measuring the rain entering the house over time. In the case of a physical system in nature, we measure the thermal, electric, mass, and momentum transport properties, to name four of the most important transport properties. Abbott's system, as unique as it seems, also possesses an intrinsic response time, which depends on the rate rain droplets move and the angle at which they hit the walls of the house. We can expect there is a critical rate beyond which either no water can enter the house or the opposite. Similarly, we observe, for any physical system, rate-dependent critical phenomena intrinsic to the system.

Going forward, the above aspects will be addressed in greater detail, emphasizing particular facets, such as transport laws, with a distinguishing eye on bulk versus molecular phenomena. We will also illuminate system time responses and dimensional restrictions and provide a classification scheme at the end, in addition to a potential outlook of nanoscience and molecular engineering. Specifically, we will discuss:

- mechanical system responses to stresses from both a bulk and molecular perspective;
- thermal transport, specifically regarding driving forces, bulk laws, statistical aspects, and size effects;
- electronic transport in dimensionally constraint systems;
- acoustic transport in 2D as compared to 3D systems;
- time effects and nanoconstraints;
- miniaturization and scaling;
- overall classification and expectations of nanotechnology.

1.3 Mechanical System Responses

In this section, we illuminate how to go beyond mere perceptions of material behavior and draw our understanding from assessing material responses to external disturbances. It is no surprise that classically tainted observations can obstruct our understanding of small systems. In this context, it is important to recognize that it is not the classical physical laws that impede our understanding but, often, a lack of recognition of the underlying assumptions. While examples are manifold to illustrate how material behaviors can be understood as nondiscriminatory, we will stay with our lubrication example discussed earlier, in which we compared thick film strain responses to the ones found in thin films under shear.

1.3.1 Bulk Rheological Responses

We take another look at the (on first sight) peculiar behavior of a liquid lubricant under shear, as depicted in Figure 1.4. It shall be pointed out that the shear behavior of liquid phases is of great technological importance in many areas, such as lubrication in the automotive and machinery industry, injection processes such as inkjet printing and jet molding, and noise suppression of systems that are exposed to humidity and temperature changes.

Webster's perception of *liquids* and *solids* just toyed with microscopic molecular pictures that go back to the Greek philosophers Leucippus and Democritus. An improved understanding of these two terms is obtained by considering classical rheological laws. In *Rheology*, a traditional branch of physics that deals with the deformation and flow of matter, we distinguish, in the extreme, between a perfect *solid-like* deformation behavior and a perfect *liquid-like* flow behavior. Typically, any practical material response to shear falls in between the two.

Perfect solid-like deformations in one dimension are well expressed via *Hooke's law* as

$$F = -k\Delta x \tag{1.1}$$

where k and Δx reflect the spring constant and the elastic length deformation, respectively. In three dimensions, assuming for simplicity an isotropic material, the equivalent force-deformation expression is given by the stress-strain $\sigma(\varepsilon)$, in relation of the form,

$$\sigma = E\varepsilon \tag{1.2}$$

where $\sigma \equiv F/A$ in units of [Pa] reflects the normal plane stress (force F per unit area A) and $\varepsilon \equiv \Delta L/L_o$ the dimensionless strain (uniaxial deformation ΔL divided by original length L_o) in the material. The proportionality factor, E, a material property, is known as Young's modulus, which also carries pressure units. The basis of Hooke's law is that the deformation energy is elastically stored and can be fully recovered. Considering simple shear, we can rewrite Eq. (1.2) with the elastic shear modulus G,[4] the shear stress τ and shear strain γ (angular shear), leading to the following stress-strain relationship:

$$\tau = G\gamma \tag{1.3}$$

Equation (1.3) reveals a linear increase in the stick-slip behavior in ultrathin films. In other words, ultrathin films can behave solid-like.

Worked Problem 1.3.1

Problem: Carbon nanotubes are cylinders of graphene (single graphite sheets) with diameters ranging from below 1 nm to several nanometers, for single wall carbon nanotubes (SWCNT), with Young's modulus of around 1 TPa (10^{12} Pa) for diameters exceeding 1 nm. It is important to note that SWCNT, because of its finite cross-section, is not truly 1D but rather a rod. A rod that is stretched longitudinally will thin in the center if we assume no structural changes because of mass conservation. The cross-sectional thinning process is captured by the Poisson ratio $\nu \equiv d\varepsilon_{\text{trans}}/d\varepsilon_{\text{comp}}$. $\varepsilon_{\text{trans}}$ is the transversal elongation strain with respect to the amount of axial compression strain $\varepsilon_{\text{comp}}$ under tensile stress $\sigma = F/A$. We shall estimate the shear modulus G based on $\nu = 0.16$.

Solution: We employ the isotropic relation that was introduced earlier in Footnote 4, i.e., $G = E/\left[2(1+\nu)\right]$, which yields for G a value of 0.43 TPa. This value underestimates the value found in the literature, which is around 0.47, indicating that SWCNT is not isotropic.

Switching from elastic deformations to perfect plastic deformations, in which energy is entirely dissipated during the deformation process, we focus on the perfect *viscous* or *perfect plastic* behavior of a system. We can say that a perfect liquid-like flow situation is a perfect plastic deformation. For perfect viscous flow in one dimension, *Newton's law of viscosity* applies, i.e.,

$$\tau_{yx} = -\eta\dot{\gamma}_{yx} \tag{1.4}$$

where x represents the sliding direction, and, y represents the momentum direction normal to the sliding plane. We find in Eq. (1.4) the liquid viscosity η[Pa · s], also a material property, and the strain rate $\dot{\gamma}_{yx}$.[5] As depicted in Figure 1.4 for thick liquid films, viscous sliding yields a constant shear stress as long as the deformation rate is kept constant.

---

[4] The shear modulus can be related to the Young's modulus for isotropic materials via the Poisson ratio ν, as $G = E/\left[2(1+\nu)\right]$.

[5] The strain rate $\dot{\gamma}_{ij}$ of Newtonian (incompressible) fluids is given by $\dot{\gamma}_{ij} \equiv \partial v_i/\partial x_j + \partial v_j/\partial x_i$, with $v_k(k = i, j)$ defining both the flow and the momentum directions.

Having gained an improved understanding of perfectly elastic and viscous shear behaviors, we are now ready to discuss the deviating qualitative shear behavior of thick and ultrathin liquid films. In the thick film, our assumption of strictly viscous Newtonian shear applies. We can assume that there are plenty of degrees of freedom for the molecules to move independently and dissipate the induced shear energy. In the case of ultrathin films, however, interfacial constraints limit the degree of freedom of the liquid molecules and require them to move to some degree in unison during shear deformations. Thus, the change in degree of freedom imposes different response times to stresses in the liquid. In Newtonian liquids, the response time of each individual molecule is so fast that any shear deformation dissipates instantaneously. For ultrathin films, however, even slow shear deformations can exceed the individual response time of a single molecule leading to a collective (cooperative) response phenomenon, as observed in solids. Thus, the stick-slip behavior in ultrathin films can be seen as a manifestation of ordering in the liquid under stress conditions. The sharp drop in the stick-slip phenomena can be interpreted as an instant strain release or as shear-induced "melting," which provides a transitory increase in the degree of freedom and an increase in the molecular response time. From the language employed here, we can infer that the underlying theories to formally describe the stick-slip phenomena lie in *Thermodynamics* and *Statistical Mechanics*.

1.3.2 Molecular Perspective of Mechanical Systems

We chose the stick-slip phenomena above as one of many examples to illustrate the importance of carefully assessing the property law(s) on the macroscale before interpreting small-scale molecular systems. Specifically, there are two aspects to keep in mind:

- statistical ensemble behaviors of molecules under interfacial and size-constrained conditions, exemplarily addressed in this paragraph by considering the flow of a polymer melt in capillaries and,
- the strength and polarity of soft intermolecular interactions that dictate the material structure and property. This aspect will be discussed in some detail in the next section of this chapter.

We shall consider the cylindrical flow in a capillary rheometer of a thermoplastic melt composed of long-chain molecules with many repeat units, known as polymers. As illustrated in Figure 1.6, capillary rheometers are *piston-die* systems with which the viscosity of polymer melts can be determined as a function of temperature and rate of deformation. A small amount of thermoplastic in the form of granules, powder, or flakes is melted by heating and forced to flow out of a cylinder through a capillary die. If the temperature T of the melt significantly exceeds the glass transition T_g (the rule of thumb is $T > T_g + 100\ ^\circ\mathrm{C}$), the liquid viscosity η_o is well represented by the Arrhenius equation,

$$\eta_o(T) = Ae^{E_o/k_BT} \tag{1.5}$$

E_o represents a viscous flow activation energy in joules, $k_B = 1.380649 \times 10^{-23}$ J/K the Boltzmann constant, T is the absolute temperature in Kelvin, and A is a constant. The subscripted nod of the viscosity implies that no shear force is applied. The viscosity in SI units

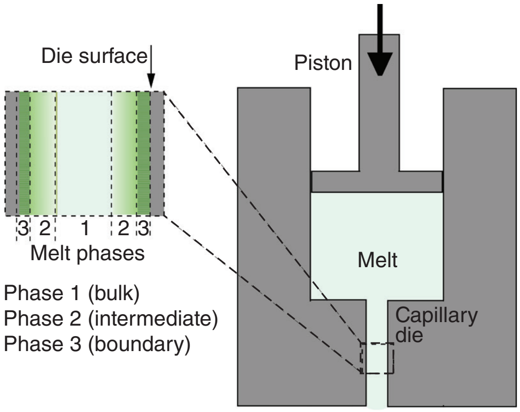

Figure 1.6 Capillary piston-die rheometer. Polymer phase regimes in capillary are highlighted on the left.

is [Pa · s]. The viscous flow activation energy E_o is the energy barrier that has to be overcome for flow to occur. With the Arrhenius equation, only temperature effects on viscosity are considered – time, or strain rate effects are neglected.

The phase system, described with the Arrhenius equation, typically consists of coiled-up chains with little entanglements. Rate effects have to be considered for a bulk polymer system if the system temperature is closer to the glass transition temperature, at which the polymer molecules have the tendency to entangle. The larger the chains, the larger the entanglement.

The Arrhenius expression is inadequate for an entangled polymer melt and must be expanded to reflect the rate effect. One way to do that is to consider the probability for chain motion given by the ratio of two volumes, namely the single diffusion jump volume v_d divided by the average free volume per molecule v_f. The single jump volume originates from a "jump model," in which it is assumed that voids exist in the melt that allows segments of the molecules to move in consecutive jumps along the shear stress direction, Figure 1.7(a). Under zero stress ($\tau = 0$), the activation barrier E_o is related to the jump frequency ν_o as $\nu_\mathrm{o} = (E_\mathrm{o}/2m)^{1/2}$, where m is the mass of the molecular element affected, i.e., the single crankshaft element in the polymer chain.

The melt viscosity is a measure of the rate at which chains can move relative to each other. It depends on the energy E_o involved in local backbone rotation (crankshaft motions) and other mobility resistances, such as the degree of molecular entanglements. For polymer melts closer to the glass transition, the melt viscosity can be expressed as

$$\eta = \eta_\mathrm{o}(T)e^{\alpha(\dot{\gamma})} \tag{1.6}$$

where $\alpha(\dot{\gamma}) \equiv v_d/v_f$ is a parameter that adjusts the Arrhenius expression for chain entanglement resistances during shear. Microscopically, it can be visualized as the ratio between the diffusion jump volume v_d and the free volume v_f per molecule, and as such, $\alpha(\dot{\gamma})$ is strain rate $\dot{\gamma} \equiv d\gamma/dt$ dependent. The jump situation is depicted in Figure 1.7.

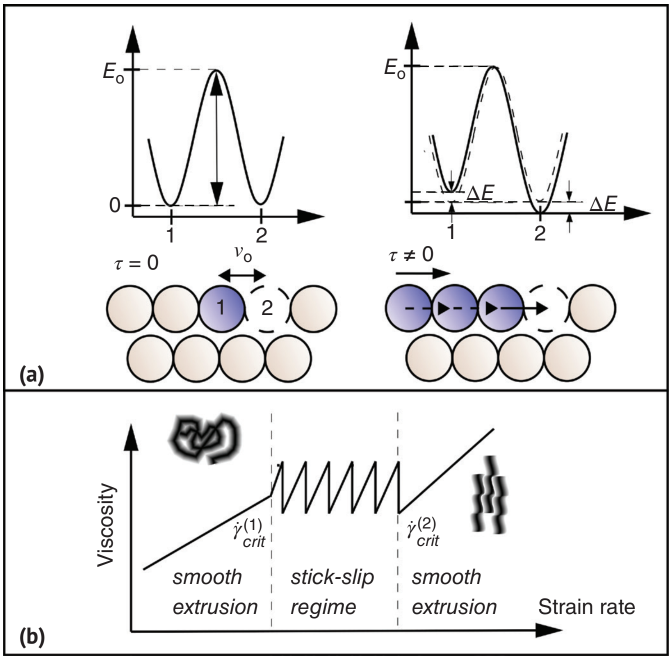

Figure 1.7 (a) Simple jump model: Submolecular activation barrier without stress (E_o) and with stress ($E_o \pm \Delta E$). Unperturbed jump frequency $\nu_o = (E_o/2m)^{1/2}$ with void dimension a. (b) Effect of entanglement and strain rate on flow performance of polymer melt.

Returning to the polymer melt in the capillary rheometer, Figure 1.6, for which we assumed a temperature $T > T_g + 100$ °C, we recognize that within the cylinder core, the polymer is in a *purely coiled phase* (phase I), i.e., its viscosity is only temperature dependent, as the molecular chains are not entangled. However, toward the capillary wall, we find an *intermediate radial regime* (phase 2), within which the polymer chains are entangled, despite the high temperature T, due to loss in free volume. The loss in free volume originates from the interaction with the third phase regime, the polymer *interfacial boundary layer* (phase 3), close to the capillary wall. The polymer molecules in phase 3 experience, with the capillary wall surface, an interface that is repelling toward the polymer molecules, causing them to "shy away" by densifying and, thus, strongly entangling and shear aligning under the flow stress conditions. In turn, due to their natural attraction toward molecules in the intermediate phase, the molecules in phase 2 also deviate from the bulk behavior and are gradually entangled.

Thus, dependent on the strain rate $\dot{\gamma}$, we will either observe smooth melt extrusion or a stick-slip flow phenomena. At low shear rates, the flow in both the bulk regime and the intermediate regime (phases 1 and 2) is very little affected by entanglements and smooth, thus, well described by Eq. (1.5), and captured in Figure 1.7(b). At some point, with increasing strain rate, $\dot{\gamma}$ will reach a critical value, $\dot{\gamma}_{\text{crit}}$, where entanglements in phase 2 become noticeable in a stick-slip kind of hindrance to flow. During the sticking phase, the chains are gradually stretched without local flow, which in turn slows down the overall flow through the capillary. Once the stress exceeds the molecular “static frictional” resistance imposed by the entanglement, the chains disentangle, which results in slippage. After disentangling, the chains release energy and re-entangle in the intermediate region while the shear flow commences at $\dot{\gamma} = \dot{\gamma}_{\text{crit}}$. The stick-slip process repeats itself. Further increasing the strain rate, $\dot{\gamma} > \dot{\gamma}_{\text{crit}}$ will bring forward the same stick-slip phenomenon until the strain rate is so high that it yields a permanently disentangled intermediate (phase 2) regime. Under such high strain rate conditions, the flow is smooth again. In the following Worked Problem, we shall explore the melt viscosity of an entangled polymer system, as found in the intermediate phase 2.

Worked Problem 1.3.2

Problem: We continue our conversation about the capillary piston-die rheometer, Figure 1.6b, and discuss the intermediate phase 2 in light of the core phase 1 at a temperature T that is closer to the glass transition temperature T_g. We shall derive an expression for the molar amount of the activation energy at temperature T for the melt viscosity of an entangled polymer system.

Solution: As we have seen, the Arrhenius expression for the melt viscosity at high temperature includes with E_o an activation barrier that is temperature independent. Considering now Eq. (1.6), we substitute the average free volume per molecule v_f with its molar quantity $V_f = N_A v_f$ and the single diffusion jump volume v_d with its molar equivalent V_d (where $N_A = 6.0221 \times 10^{23}\ \text{mol}^{-1}$ is Avogadro’s number), replace E_o with the molar activation energy Q_o, as $E_o = Q_o/N_A$, introduce the universal gas constant $R = k_B T = 8.31432\ \text{J} \cdot \text{K}^{-1} \cdot \text{mol}^{-1}$, and set $Q(T,v_d/v_f) = Q_o + \text{RT}(V_d/V_f)$, we obtain

$$\eta = Ae^{\frac{Q(T,\dot{\gamma})}{RT}}.$$

We note that with the extended Arrhenius form presented here, we utilized an apparent activation barrier that depends on both temperature and strain rate (via the rate-dependent volume ratio v_d/v_f).

Looking back at the polymer extrusion example, apparent misconceptions or expectations of the flow of a polymer melt above its glass transition could be resolved by considering molecular phenomena and local interactions. For this particular example, the molecular phenomena were based on chain entanglement induced locally by interfacial interactions. The driving force for the polymer extrusion example was a pressure force given by the piston, and our observable was the rate of melt extrusion. In the following section, we explore some of the important driving forces in nature and discuss system responses. The structure is based on the transport mechanism. Having addressed, to some degree, momentum transport with fluid flow, we will give preference in the next three sections to thermal, electronic, and acoustic transport.

1.4 Driving Forces and Responses in Thermal Transport

1.4.1 Classical Thermal Transport

The term "driving force" is not a precisely defined quantity. It describes a *property gradient* that gives rise to a rate of flow of a quantity per unit area, in short, called a flux. For instance, the temperature gradient ∇T in a wall separating two rooms that are at temperatures T_1 and T_2 gives rise to a heat flux $\boldsymbol{q}$, as long as the temperatures are dissimilar. A *constitutive relation* is needed to connect the resulting flux to the driving force. Some constitutive equations are empirical, and others are derived from first principles. The empirical constitutive equation that relates the heat flux $\boldsymbol{q}$ [W · m^{-2}] to the temperature gradient ∇T during conductive heat transfer is *Fourier's law*,

$$\vec{q} = -k_c \vec{\nabla} T; \quad \text{with} \quad \vec{\nabla} = \nabla \quad \text{and} \quad \vec{\nabla} = \left(\frac{\partial}{\partial x}, \frac{\partial}{\partial y}, \frac{\partial}{\partial z}\right) \text{ for } T = T(x, y, z) \tag{1.7}$$

where the material property k_c [W/m · K] is the thermal conductivity. In this simple form of conductive heat transfer, we assume isotropic thermal conductivity, as presented in the Worked Problem below, in which we restrict ourselves to 1D heat transfer.

Worked Problem 1.4.1

Problem: Consider a uniform wall of thickness L that separates two large rooms at temperatures T_1 and T_2. The temperatures at each side of the wall shall match the room temperatures. Our goal is to find an expression for the temperature gradient in the wall.

Solution: First, we notice that the conservation of energy requires the heat flux q_x to be constant throughout the wall. Based on Fourier's law, expressed here in one dimension to match the figure to the left,

$$q_x = -k_c \frac{dT}{dx}$$

and the boundary condition $T = T_1$ at $x = x_1$ and $T = T_2$ at $x = x_2$, we find after integration:

$$q_x(x_2 - x_1) = -k_c(T_2 - T_1)$$

Combining the two equations yields the temperature gradient

$$\frac{dT}{dx} = \frac{T_2 - T_1}{x_2 - x_1} = \frac{T_2 - T_1}{L} = \frac{\Delta T}{L},$$

which is proportional to the temperature difference $\Delta T = T_1 - T_2$, and, inversely dependent on the wall thickness. While ΔT is considered the driving force, $1/L$ is known as the wall resistance for heat conduction.

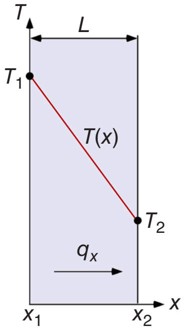

Figure P1.4.1 1D Heat flux through a plane wall.

With Fourier's rate law, we introduced the thermal conductivity k_c, which depends on the temperature and the material of choice. The conduction parameter is material intrinsic and, thus, independent of size or shape of the material. It expresses the ability of the material

Table 1.2 Thermal properties, densities, and speed of sound of selected materials.

Material	Thermal conductivity, k_c [W/m · K]	Specific heat capacity, c_p [J/kg · K]	Density, ρ [kg/m^3]	Speed of sound, v_s [m/s]
Poor conductors				
Glass (Pyrex)	1.005	840	2230	5600
Cork	0.04	2000	200	366
Mica (muscovite) in-plane	0.71	840	2800	2400
Neoprene	0.192	2176	1250	1600
Nylon 6	0.23	1530	1130	1100
Oak (English brown)	0.17	2380	740	2565
Pine wood (with grain)	0.22	2301	670	3960
Polyethylene (LD)	0.331	2092	920	2600
Polyethylene (HD)	0.5	2300	950	2000
Polystyrene (foam)	0.026	1130	46	2350
Rubber (butyl)	0.088	1966	900	1830
Uranium oxide	8.8	300	10970	3850
Teflon	0.25	1000	2200	1400
Good conductors				
Aluminum	226	921	2698	6320
Copper	398	385	8940	4600
Gold	317	128	19300	3240

to conduct heat. The ability to store energy in materials is expressed by the volumetric heat capacity at constant pressure, $C_V = \rho c_p$, where ρ is the mass density and c_p [J/kg · K] is the specific heat per unit mass at constant pressure. Values of the thermal conductivity and specific heat for some selected solids are provided in Table 1.2. The ratio between thermal conductivity and storage capacity defines how fast a material can transfer heat. Thus, we define *the thermal diffusivity* as $\alpha \equiv k_c/\rho c_p$. The SI units for diffusivities here are [m^2/s] and are defined analogously to other diffusion parameters, such as particle diffusivity. With the introduction of the thermal diffusivity, Fourier's law can be expressed as

$$\vec{J} \equiv \frac{\vec{q}}{\rho c_p} = -\alpha \vec{\nabla} T. \tag{1.8}$$

A comparable expression to Fourier's rate law can be found for particle diffusion (e.g., molecular species A diffusing through B) via Fick's law at constant total concentration, $\boldsymbol{J_{AB}} = -D_{AB} \boldsymbol{\nabla} c_A$, where $\boldsymbol{J}$ [mol/m^2 · s] is the diffusive flux of A, D_{AB} [m^2/s] is the binary diffusion coefficient, and ∇c_A represents the driving force, namely, the molar concentration gradient of A. There are many more examples of property gradients that can give rise to fluxes.

1.4.2 Thermal Conductivity Based on Classical Mechanics and Statistics

Let us consider the wall in Problem 1.3.1 to be a vessel of thermal conductivity k_c (with ultrathin vessel walls of infinite conductivity) filled with an "ideal gas" of noninteractive particles (e.g., molecules). The average (statistical) distance the particles can move between collisions is the so-called *mean free path* λ, which we assume to be much smaller than any of the three vessel size dimensions. The mean free path is given as the product between the average particle velocity $\langle v\rangle$ and average time τ of free traveling between collisions:

$$\lambda = \langle v\rangle\tau \tag{1.9}$$

With the mean free path, we can express how the thermal energy is dispersed using the thermal diffusivity α, which is related to λ, as

$$\alpha = \frac{1}{3}\langle v\rangle\lambda \tag{1.10}$$

The factor 1/3 expresses the equal probability of diffusion in a 3D volume V. Considering that the thermal diffusivity α is related to the thermal conductivity k_c as $\alpha = k_c/\rho c$, it follows for a constant volume system,

$$k_c = \frac{1}{3}\langle v\rangle\lambda\rho c_V \tag{1.11}$$

where c_v is the specific heat at constant volume. Note that here, we describe thermal conduction only and do not consider convective heat transfer. In that sense, we consider the gas system to be quiescent.

It is convenient to combine $\rho c_V \equiv C$, known as volumetric heat capacity with SI units $[\mathrm{J} \cdot \mathrm{K}^{-1} \cdot \mathrm{m}^{-3}]$ (not to be confused with the heat capacity at constant volume c_V that carries the units [J/K]). While considering a constant volume system, the gas pressure represents a variable affecting the volumetric heat capacity and the mean free path. It is interesting to note, however, as we will see later, that the product λC is pressure independent, and with it, so is the thermal conductivity k_c, as long as the mean free path is much smaller than the smallest system size L in V (i.e., $\lambda \ll L$). In other words, for a bulk system with a pressure P large enough that molecular collisions are statistically relevant, we can assign to the system a standard pressure-independent conduction coefficient $k_{c,o}$

$$k_{c,o} = \frac{1}{3}\langle v\rangle\lambda C|_{T_o} \tag{1.12}$$

at a given reference temperature $T_o = 0$ °C.

The pressure P of the ideal gas of N molecules of molecular mass m in volume V can be expressed from the perspective of classical mechanics, as

$$P = \frac{1}{3}\rho_N m\langle v^2\rangle \tag{1.13}$$

where $\rho_N = N/V$ is the molecule number density. If we furthermore consider that the kinetic energy per unit volume of the system is given by

$$e_{kin} = \frac{1}{2}\rho\langle v^2\rangle = \frac{1}{2}\rho_N m\langle v^2\rangle \tag{1.14}$$

we find that the pressure is 2/3 of the translational system energy per unit volume, i.e.,

$$P = \frac{2}{3} e_{kin} \tag{1.15}$$

The pressure can be perceived as a static system pressure, as we do not consider convective transport but only random diffusive particle motions.

Lastly, we shall employ the equation of state of an ideal gas based on the Boltzmann constant $k_B = 1.38 \times 10^{-23}$ J/K, which is $PV = Nk_BT$, to express the system pressure as

$$P = \rho_N kT \tag{1.16}$$

Combining Eqs. (1.14)–(1.16) yields

$$\frac{1}{2}m\langle v^2\rangle = \frac{3}{2}k_BT \tag{1.17}$$

which brings forward the average thermal energy of the system that is carried by each microscopic degree of freedom:

$$E = \frac{1}{2}k_BT \tag{1.18}$$

Contemplating, for instance, a monoatomic gas system of N atoms (e.g., helium), the total internal kinetic energy is

$$U = \frac{3}{2}Nk_BT \tag{1.19}$$

where the number three represents the three translational degrees of freedom. In the case of a diatomic gas system (e.g., H_2 or O_2), we have to consider, in addition to translation, also rotations that add two additional degrees of freedom, which brings the total up to 3 + 2 = 5. For a molecular system with f degrees of freedom, we can write

$$U = \frac{f}{2}Nk_BT \tag{1.20}$$

Considering that the heat capacity is defined as the thermal gradient of the internal energy ($\partial U/\partial T$), we find that the volumetric heat capacity $C = N_A c$ can be expressed as

$$C = \frac{\partial U/\partial T}{V} = \frac{f}{2}\frac{N}{V}k_B = \frac{f}{2}\rho_V k_B \tag{1.21}$$

where ρ_v stands for the mass density. Thus, returning to the thermal conductivity

$$k_c = \frac{1}{3}\langle v\rangle\lambda c$$

with $c = \rho c_v$, it follows

$$k_c = \frac{f}{6}k_B\,\rho_N\langle v\rangle\lambda \tag{1.22}$$

According to the Maxwell-Boltzmann distribution, we can express the mean velocity as

$$\langle v\rangle = \sqrt{\frac{8k_BT}{\pi m}} \tag{1.23}$$

where m is the mass of the gas particle. The mean free path between elastic collisions of molecules with diameter d is derived, as

$$\lambda = \frac{1}{\sqrt{2}\rho_N \pi d^2} \tag{1.24}$$

If we substitute these two expressions, Eqs. (1.23) and (1.24), into Eq. (1.22), the thermal conductivity becomes

$$k_c = \frac{f}{3d^2}\sqrt{\left(\frac{k_B}{\pi}\right)^3 \frac{T}{m}} \tag{1.25}$$

The key features of the thermal conductivity with a mean free path substantially smaller than any system size dimension ($\lambda \ll L$), as expressed in Eq. (1.25), are:

- k_c is independent of the number particle density, and thus, the static system pressure, but temperature-dependent (more specifically: $k_c \propto \sqrt{T}$).
- Gases composed of smaller molecules transport heat more effectively than gases with larger particles (i.e., smaller particle gases possess larger k_c values), which is matched and further enhanced by a particle mass comparison between small and large particle systems.

It shall be noted that the gas kinetic theory is restricted to modest pressures, where molecular interactions (i.e., Van der Waals interactions) can be ignored, and the mean free path is significantly smaller than the system size.

For the gas kinetic derivation of k_c, Eq. (1.25), we assumed that the molecules are spherical and move with velocities close to the average velocity. The isotropic spherical assumption is only truly applicable to single-atom molecules. Already, small polyatomic molecules, such as the diatomic molecules, hydrogen H_2, oxygen O_2, or nitrogen N_2 are not well described by Eq. (1.25). The second assumption of a small deviation from the average velocity does not apply to every molecular gas system. For instance, the velocity distribution of argon is narrow, which leads with Eq. (1.25) to a decent estimate of the thermal conductivity. Different is the situation for helium, for which we find a wide distribution, and thus, many molecules with velocities different from the average value. Consequently, Eq. (1.25) yields a poor estimated value for thermal conductivity, an aspect further illuminated in a study problem at the end of this chapter. The sensitivity toward the width of the velocity distribution originates from the thermal transport direction, which is in line with the molecular motion. Thus, a large population of molecules moving substantially different from the mean velocity can greatly affect the thermal transport parameter k_c. As illustrated in the Worked Problem below, the velocity distribution is given by the Maxwell-Boltzmann distribution

$$f(v) = 4\pi v^2 \left(\frac{m}{2\pi k_B T}\right)^{3/2} e^{\frac{-mv^2}{2k_B T}} \tag{1.26}$$

where v stands for the molecule velocity. The probability density function $f(v)$ gives the probability, per unit velocity, of finding particles with a velocity near v. We can infer from the Worked Problem that the distribution is skewed to the right, which shifts the mean value to the right, i.e., faster-moving molecules – an aspect that we did not consider in the development of our gas kinetic theory.

To remedy the situation, we shall consider the relationship between the heat and momentum transport coefficients, k_c, and η, the dynamic viscosity. The two quantities can be expressed in terms of molecular number density and mean free path as $k_c = 1/3\ \rho_N\langle v\rangle m\ c_V\lambda$ and $k_c = 1/3\ \rho_N\langle v\rangle m\lambda$, which yields the relation

$$\frac{k_c}{\eta} = \frac{c_V}{m} \tag{1.27}$$

This relationship is challenged when the velocities between the two transport phenomena differ.

To address the issue, Arnold Eucken[6] considered first to separate the specific heat into two components, i.e., $c_v = c_{v,t} + c_{v,r}$, in which $c_{v,t}$ reflects the heat capacity component attributed to molecular translation, and $c_{v,r}$, the heat capacity component attributed to molecular rotation. He then modified the transport coefficient relation for ideal gases, $k_c = \eta\left(2.5c_{v,t} + c_{v,r}\right)$. Returning with this expression to the gas kinetic theory and introducing the heat capacity ratio $\gamma = c_p/c_v$, where c_p is the heat capacity at constant pressure, we obtain after some tweaking the Eucken's gas kinetic formula for the thermal conductivity for ideal gases:

$$k_c = \eta c_v\left(\frac{9\gamma - 5}{4}\right) \tag{1.28}$$

While Eucken's formula has been adjusted further over the years by incorporating a dimensional constant that accounts for differences in the molecules' internal degrees of freedom, it provides a reasonably good estimate for the thermal conductivity of many pure gases at modest pressures and temperatures. This is shown in the Worked Problem below based on gas properties summarized in Table 1.3.

Returning to the gas kinetic derivation of k_c, Eq. (1.25), we introduced with f a parameter that captures the molecular degrees of freedom. The most obvious of them are the three translational degrees of freedoms, f_{trans}, a molecule possesses in a bulk gas system. Molecules of more than one atom also have the ability to rotate visually around rotational axes. While linear molecules, such as carbon monoxide (CO), possess two axes and hence, $f_{\text{rot}} = 2$ rotational degrees of freedom, nonlinear molecules, e.g., carbon dioxide (CO_2), have $f_{\text{rot}} = 3$ rotational degrees of freedom. Lastly, ignoring electronic degrees of freedom,[7] intermolecular bond vibrations provide additional degrees of freedom with $f_{\text{vib}} = 3N - 5$ (for linear molecules) or $f_{\text{vib}} = 3N - 6$ (for nonlinear molecules), where N stands for the number of atoms in the molecule. In total, molecules can have up to $f = f_{\text{trans}} + f_{\text{rot}} + f_{\text{vib}} = 3N$ degrees of freedom, regardless of the molecular shape. Monoatomic molecules, such as helium (He), possess with $f = f_{\text{trans}} = 3$, only translational degrees of freedom. Diatomic molecules, such as CO can exhibit up to $f = f_{\text{trans}} + f_{\text{rot}} + f_{\text{vib}} = 3 + 2 + 1 = 3N = 3 \times 2 = 6$ degrees of freedom.

The degrees of freedom are also referred to as thermal modes that can be dormant or active. With increasing temperature, the thermal modes in a gas are turned on. For very low finite temperatures, only translational modes are active. The molecular scattering events do not transfer enough energy to activate rotational modes. Once a critical temperature

---

[6] A. Eucken, Ceramic Abstracts, **11**, 353 (1932).

[7] The impact of electronic degrees on heat conduction is small in comparison to the other three.

Table 1.3 Properties of selected gases at 300 K and 1 bar.

Molecules	c_V [kJ/kg · K]	γ	η [μ Pa · s]	M [g/mol]	d [Å]	k_c [mW/m^2 · K]
Monoatomic						
Helium (He)	3.12	1.667	19.6	4.00	1.4	149
Argon (Ar)	0.31	1.667	22.3	39.948	1.88	17.7
Krypton (Kr)	0.15	1.667	25.4	83.798	2.02	9.5
Diatomic						
Hydrogen (H_2)	10.2	1.4	9.0	2.016	2.4	186.6
Nitrogen (N_2)	0.74	1.4	17.8	28.013	3.0	25.8
Oxygen (O_2)	0.66	1.4	20.6	31.999	3.0	26
Linear						
Carbon dioxide (CO_2)	0.66	1.28	15.0	44.01	3.3	16.8
Nonlinear						
Ammonia (NH_3)	1.64	1.32	10.1	17.03	2.6	25.1
Methane (CH_4)	1.70	1.31	11.1	16.05	3.8	34.4

threshold is reached, the temperature-induced kinetic energy is sufficient to free rotational modes, and thus, system internal energy changes involve molecular translations and rotations. With further temperature increases, the thermal disturbances will reach a point where bond vibrational modes in polyatomic molecules are activated. The addressed mode activation temperatures are strongly dependent on the inner structure and shape of the molecules, as well as, at high pressures, on intermolecular interactions.

Worked Problem 1.4.2

Problem: We shall determine the thermal conductivity for argon (Ar), methane (CH_4), and oxygen gas (O_2) at 1 bar and 300 K and compare the values to the experimental values of 0.0177 W/m · K, 0.0344 W/m · K, and 0.026 W/m · K, respectively.

Solution: We employ first Eq. (1.25)

$$k_c = \frac{f}{3d^2}\sqrt{\left(\frac{k_B}{\pi}\right)^3 \frac{T}{m}}$$

and set $f_{\mathrm{Ar}} = f_{\mathrm{trans}} + f_{\mathrm{rot}} + f_{vib} = 3 + 0 + 0 = 3$ for argon, $f_{\mathrm{CH_4}} = f_{\mathrm{trans}} + f_{\mathrm{rot}} + f_{\mathrm{vib}} = 3 + 3 + 0 = 6$ for methane, a nonlinear molecule, and, $f_{\mathrm{O_2}} = f_{\mathrm{trans}} + f_{\mathrm{rot}} = 3 + 2 + 0 = 5$ for oxygen, a diatomic molecule. The activation of the vibrational mode requires much larger temperatures above 1000 K. From Table 1.3, we substitute approximate values for the molecular diameters ($d_{\mathrm{Ar}} = 1.4$ Å, $d_{\mathrm{CH_4}} = 3.8$ Å and $d_{\mathrm{O_2}} = 3.0$ Å) and molecular masses, $m = M \times N_{\mathrm{A}}$ ($m_{\mathrm{Ar}} = 6.634 \times 10^{-26}$ kg, $m_{\mathrm{CH_4}} = 2.66 \times 10^{-26}$ kg and $m_{\mathrm{O_2}} = 5.631 \times 10^{-26}$ kg) into Eq. (1.25), which yields

$$k_{c,\mathrm{Ar}} = 0.0175\ \mathrm{W/m \cdot K}$$

$$k_{c,\mathrm{CH_4}} = 0.0135\ \mathrm{W/m \cdot K}$$

$$k_{c,\mathrm{O_2}} = 0.0128\ \mathrm{W/m \cdot K}$$

for the respective thermal conductivities. As expected, only for argon the thermal conductivity is estimated well with Eq. (1.25). The calculated methane value is off the literature value by about a factor of 2.5, and the one for oxygen is off by a factor of about 2. The discrepancy for oxygen originates most prominently from the non-isotropy of the molecular shape, while the even larger discrepancy for methane comes from the wide-skewed velocity distribution, as highlighted in the Maxwell-Boltzmann graph further below.

Employing Eucken's gas kinetic formula, Eq. (1.28),

$$k_c = \eta c_v \left(\frac{9\gamma - 5}{4} \right)$$

yields for the respective conductivities:

$$k_{c,\mathrm{Ar}} = 0.0174\ \mathrm{W/m \cdot K}$$

$$k_{c,\mathrm{CH_4}} = 0.032\ \mathrm{W/m \cdot K}$$

$$k_{c,\mathrm{O_2}} = 0.026\ \mathrm{W/m \cdot K}$$

After having substituted experimental data for (η, c_v, γ) from Table 1.3, the calculated values compare well with the experimental thermal conductivity values.

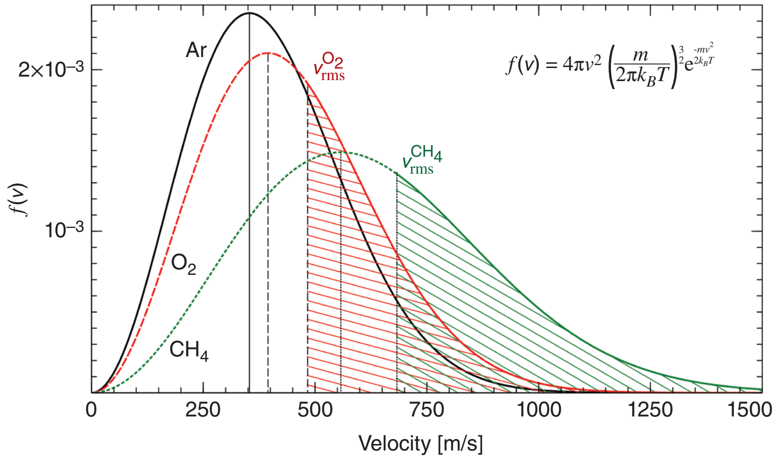

Figure P1.4.2 Maxwell-Boltzmann distribution of Ar, O_2, and CH_4 gas at 1 bar and 300 K. The root-mean-square (*rms*) velocities are shown for O_2 and CH_4, highlighting with the shaded areas, the degree of which the distributions are screwed to faster velocities.

Side note to Eq. (1.25) calculations: If we had also considered the vibrational degrees of freedom that yield an additional nine and one degree(s) of freedom for methane and oxygen, respectively, both calculated values for k_c would be closer to the actual values of the thermal conductivity. While for oxygen the discrepancy would shrink to a factor of 1.6, for methane, the calculated k_c value would match the literature value of 0.034 W/m · K. This is a surprising result and should be considered coincidental. For oxygen to reach the observed experimental value, the degrees of freedom in Eq. (1.25) would have to be raised to 10, which cannot be justified.

While we restricted our discussion of the thermal conductivity above to ideal gas particle collisions, we can extend the kinetic theory of gases also to amorphous (noncrystalline) solids, such as oxides or polymers, in which heat conduction is predominantly carried via atomic positional oscillations that move through the material. The energy quanta moving through solids are known, quantum mechanically, as *phonons*. This leads to the so-called "dominant phonon approximation" of the thermal conductivity of a solid that involves a *phonon gas*, which is described analogously to what was discussed above for ideal gases. The mean free path of the phonons, λ_{ph}, is given by phonon scattering at imperfections (defect sites) in the solid that are abundant in amorphous materials. As for ideal gases above, the phonon approximation for heat conduction, expressed with Eq. (1.25), requires that $\lambda \ll L$.

The requirement for the mean free path of gases and amorphous solids to be much smaller than any system size dimension is not met for

- gases at ultralow pressures, where particle collisions are statistically sparse,
- systems with critical size(s) on the nanoscale (e.g., nanoporous materials with pore sizes below 50 nm), and
- and solids with a low defect number density.

In all three cases, the mean collision or scattering length is on the order of the system size dimension. In the extreme, scattering occurs only at the system boundary, and thus, the thermal conductivity within the material reaches zero. We shall discuss this aspect next.

1.4.3 Size Effect on Thermal Energy Transfer

Classical non-convective heat conduction based on the kinetic dilute gas theory requires that any critical system size exceeds the mean free path by at least one to two orders of magnitude. The theory breaks down for mean free paths on the order of 10 L ($\lambda \sim 10\ L$), as illustrated in Figure 1.8 for a nanoporous system with air-filled pores of diameter D (D is a system-specific L, more generally known as the characteristic length for the gas, the gas volume), where the thermal conductivity falls dramatically. The ratio between the mean free path and the characteristic length of the gas volume, here λ/D, is known as *Knudsen number Kn*. Thus, for $Kn \equiv \lambda/D \ll 1$, the earlier, pressure-independent, kinetic gas theory applies. As a rule of thumb, we consider that for $Kn > 0.1$, adjustments or extensions to the classical bulk theory are necessary.

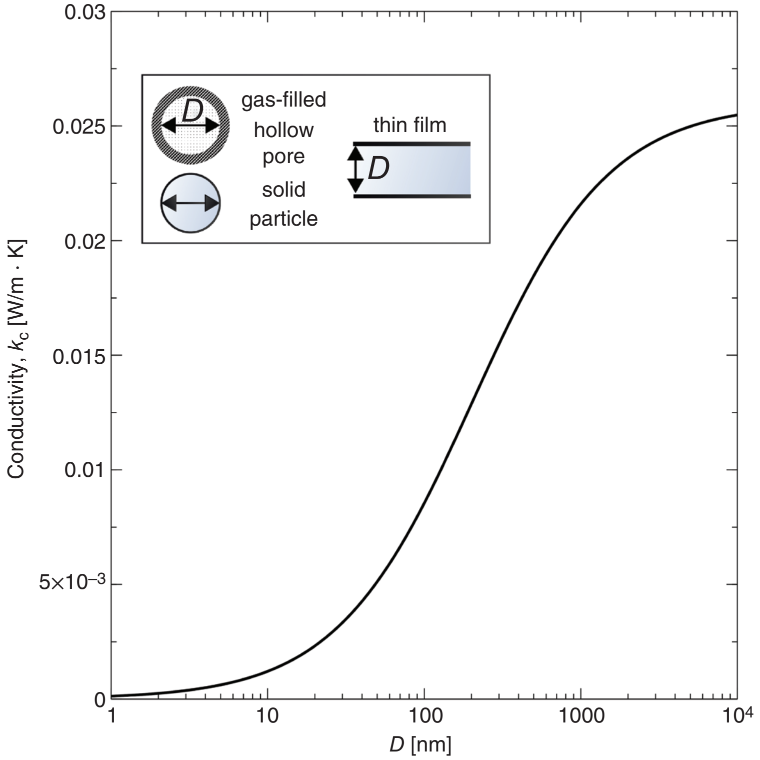

Figure 1.8 Thermal conductivity as a function of the critical size $L = D$ for a mean free path $\lambda \sim 10D$ or smaller based on *Knudsen kinetic theory*. Data used for this plot are from ambient air: $k_{c,o} = 0.026$ W/m · K, $\lambda = 68$ nm. $\beta = 1.5$ (arbitrary choice in the range of 1.5 to 2 for air). Inset: Air-filled hollow pores (e.g., found in porous polymers) are consistent with the plot presented. Qualitatively similar $k_c(L)$ behaviors can be found for thin films and solid particles.

Here we introduce the well-known *Knudsen's extension* of the gas theory applicable to confining dimensions, where the thermal conductivity for gases is expressed as

$$k_c = \frac{k_{c,o}}{1 + 2\beta\left(\frac{\lambda}{D}\right)} \tag{1.29}$$

The parameter $k_{c,o}$ represents the classical thermal conductivity for $\lambda \ll L(Kn \ll 1)$ at standard condition (1 atm, 20 °C) while β denoting a dimensionless coefficient that is dependent on the type of gas and temperature. For air, β is within the range of 1.5 and 2. It reflects the material-specific scattering quality at the pore interface, which becomes increasingly more prominent for smaller pores. In the limit of single-digit nanometer pore sizes, gas molecular collisions are unlikely, and mostly boundary scattering is observed. At this point, gases seize the ability to carry thermal energy effectively, reducing the thermal conductivity to close to zero.

A similar expression as Eq. (1.29) is used for amorphous solids with

$$k_c = \frac{k_{c,\text{bulk}}}{1 + \left(\frac{\lambda_{ph}}{L}\right)} \tag{1.30}$$

where $k_{c,\text{bulk}}$ is the bulk thermal conductivity, and λ_{ph} is the mean free path of phonon scattering at defect sites in the solid. The mean free path can be expressed as

$$\lambda_{ph} = \frac{3k_{c,\text{bulk}}}{Cv_g} \tag{1.31}$$

In terms of the phonon group velocity v_g, which expresses the overall collective wave velocity.

Worked Problem 1.4.3

Problem: The local size reduction to the nanometer scale in materials that reduce diffusion based on molecular collisions or phonon transport with boundary scattering resulted in insulating materials that can reduce the thermal conductivity by up to two orders of magnitude. We compare the heat transfer coefficients between an insulating double sheet wall with a macroscopic air gap of volume V with a porous wall of a pore size of 5 nm and 100 nm, assuming the same gas volume V within the wall as in the porous system.

Solution: We employ Eq. (1.29)

$$k_c = \frac{k_{c,o}}{1 + 2\beta\left(\frac{\lambda}{L}\right)}$$

and use the values $k_{c,o} = 0.026$ W/m · K, $\lambda = 68$ nm. $\beta = 1.5$ for ambient air in the gas-filled volume V. Substituting the values into the equation yields a thermal conductivity through the pores in the porous wall of 0.0006 W/m · K and 0.0086 W/m · K for 5 nm and 100 nm size pores, respectively. The comparative ratio between the bulk system and the porous system is

$$\frac{k_{c,o}}{k_c} k_c = \frac{0.026}{0.0086} = 3 \text{ (for 5 nm pores)}$$

$$\frac{k_{c,o}}{k_c} k_c = \frac{0.026}{0.0006} = 43 \text{ (for 100 nm pores)}$$

Ignored in this comparison was the heat conduction through the solid mesh around the pores.

Our focus in this last section has been on size-constrained transport, making interfaces more prominent in defining the transport phenomena. Going a step further and reducing any of the size dimensions, such as the cross-sectional area of a wire or the thickness of a film, to the mean free path of the heat carriers, phonons, and electrons, the thermal conductance G^{th} can show limiting quantum effects. As we discuss in greater detail in the next section for electrical transport, 1D transport systems reveal minimum conductance quanta if the transport of phonons or electrons can be considered ballistic (scattering-free). For quantum effects to occur, nanoscale dimensions and a close to zero Kelvin temperature are required. The conduction quantum for 1D heat conduction (equivalent to thermal conductivity per unit length L) was, for single polarization, theoretically predicted[8(a)] and experimentally[8(b)] confirmed to be

$$G_{\mathrm{o,1D}}^{th} \equiv \frac{k_{c,\mathrm{1D}}}{L} = \frac{\pi^2 k_B^2 T}{3h} \left[\frac{\mathrm{J}}{\mathrm{s \cdot K}} = \frac{\mathrm{Watt}}{\mathrm{K}}\right] \tag{1.32}$$

Most notable is that the thermal conduction quantum is independent of any material properties and only dependent on temperature. While for 1D systems, the thermal quantum conductance shows a linear temperature dependence, for 2D polar nanofilms, a quadratic temperature dependence has been suggested.[9] As we will see in the next section, the quantum conductance depends on the density of states that distinctly differ based on the system's dimensionality.

1.5 Electronic Transport of Lower Dimensional Systems

So far, we have focused on the impediment of transport due to size constraints that led to effective properties, such as the Knudsen thermal conductivity. Effective properties invite scaling laws, as they will be discussed in Section 1.8. Here, our interest goes beyond just constraining the size, but in effect to reduce a dimension entirely and discuss aspects of a system of lower dimensionality. While we illustrated size constraints in Section 1.4 with thermal transport, we chose in this section the transport of electrons, as our expository transport system.

Material properties, such as the ability to conduct heat, electric current, and absorb light, are closely related to the material's atomistic or molecular structure. The most dramatic changes in material structures occur by entirely removing a dimension from the system. This leaves us with 2D, 1D, and 0D materials. Respectively in practice, we deal with *quantum wells* or ultrathin films (e.g., metal films of <2 nm thickness and graphene); quantum wires, nanotubes, or nanofilaments (e.g., metal nanowires of <2 nm diameter, and single wall carbon nanotubes); and *quantum dots* or nanoclusters (e.g., metal nanoparticles with <2 nm diameter, and Buckminster fullerenes such as C_{60}), Figure 1.9. The term "quantum" is employed for systems for which the electronic properties are of interest.

In Figure 1.10(a), the electric conductance in units of [A/V] is plotted schematically as a function of the electric potential [V], for a bulk 3D, 2D, 1D, and 0D system. The bulk system follows the classical Ohm's law, i.e.,

$$G_e \equiv 1/R_e = I/V\ [\mathrm{S = Siemens}] \tag{1.33}$$

---

[8] (a) L.G.C. Rego et al., Phys. Rev. Lett., **81**, 232 (1998); (b) K. Schwab et al., Nature, **404**, 974 (2000).

[9] Y.Y. Guo et al., Phys. Rev. B, **104**, L201407 (2021).

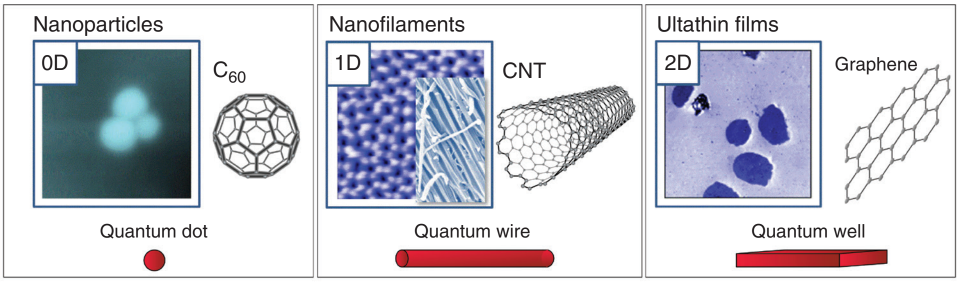

Figure 1.9 Zero, one-, and two-dimensional systems: Nanoparticles (0D), nanofilaments (1D) in nanoconduits, and ultrathin films (2D). Provided are examples of carbon allotropes (C_{60} fullerenes, single wall carbon nanotubes (CNT), graphene).

that sets the conductance, which is equivalent to the inverse of the electric resistance $R_e[\Omega = \mathrm{V/A}]$, equal to the ratio of the resulting electric current, I [A], and the applied voltage V [V]. Thus, in the bulk, an altered voltage (i.e., driving force) changes the current proportionally so that the electric conductance stays constant, as depicted in Figure 1.10(a). The conductance is an extensive property, depending on the cross-sectional area A and the length L of the wire. Its intrinsic property is known as conductivity σ_e, defined macroscopically as $\sigma_e = G_e L/A$, and carries the SI units [S/m]. The conductivity relates the current density $\vec{j}$ to the electric field $\vec{E}$, as $\vec{j} = \sigma_e \vec{E}$. In analogy, the intrinsic property of the electric resistance, the resistivity ρ_e, is $\rho_e = 1/\sigma_e = R_e A/L$. Ohm's law deviating behaviors are found for lower dimensionalities, Figure 1.10(b,c).

Quantum point contacts (2D), Figure 1.10(b), and quantum wire connections (1D) between electron reservoirs can exhibit a staircase conductive behavior if the transport can be considered 1D ballistic (no scattering). This staircase behavior originates in the unconstrained flow direction of the contraption that connects the reservoirs due to dimensional quantum constraints in either one or both perpendicular system directions. The quantum constraint is on the order of h/mv (inverse of the particle linear momentum $p = mv$, times the Planck constant h), also known as the *de Broglie wavelength* of the electrons. We will address this unique behavior in greater detail below.

With Figure 1.10(c), we added an electronic transport system, the *single electron box* that features a classically forbidden element, namely, the *tunnel junction*. This aspect will be discussed in greater detail in a later chapter. Here, we shall provide just a brief teaser of what is coming. The tunnel junction manifests a very narrow insulating gap on the order of several Ångstrom (0.1 nm), small enough for an electron to travel through. The *single electron box* in Figure 1.10(c) features a close 0D conductor or semiconductor particle of <2 nm diameter, known as a *quantum dot* (QD). The QD is separated from the electron source by the tunnel junction of tunnel-resistant R_t. The distance between the QD and the gate, however, is chosen to be large to eliminate the possibility of tunneling. Thus, electrons that reach the QD through the tunnel junction are trapped. The QD behaves like an *artificial atom and can be depicted*, in accordance with Bohr's model, as a particle with discrete energetic "electron orbitals" that fulfill Pauli's exclusion principle. We will learn more about these aspects related to single electron transistors later. The point here is that

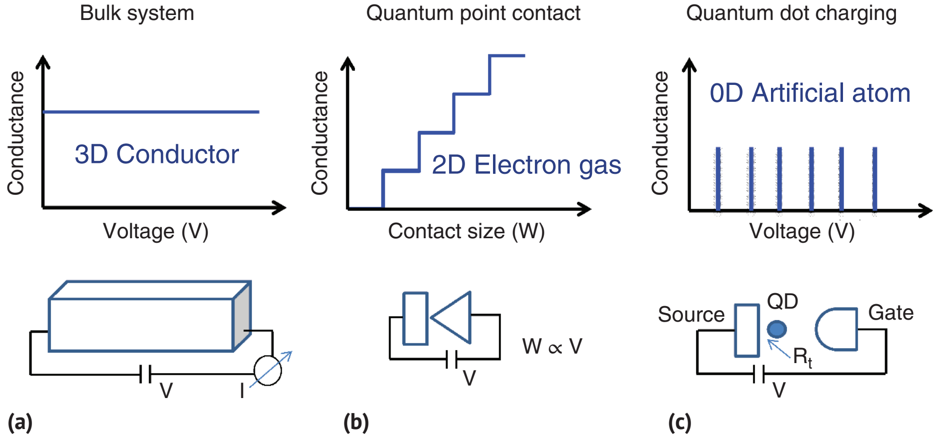

Figure 1.10 (a) Constant conductance (Ohm's law) in bulk systems. (b) Quantum point contacts and ballistic electron transport show voltage-dependent conductance staircase due to contact size increase and mode discretization. (c) Single electron conduction through tunnel junction resistance R_t from a source electrode to a QD (QD → artificial atom) that exhibits well-defined electron levels.

a well-defined energy quantum is required to move a single electron from the source to an uncharged QD. If the QD is already loaded with uncompensated charges, ne (n being the number of elementary charges $e = 1.6022 \times 10^{-19}$ C), then the energy necessary to charge the QD is

$$E_c = \frac{(ne - Q_e)^2}{2C_{dot}}; \text{ with } Q_e \equiv VC_o \tag{1.34}$$

where the charge buildup (polarization) toward the gate, Q_e, lowers the Coulomb barrier. C_{dot} represents the total charge capacitance of the dot that includes also the gate polarization capacity C_o. Figure 1.10(c) shows the resulting single electron conductance of the charge $\Delta Q_e = e$ at discrete bias voltage steps of $\Delta V = e/C_o$.

1.5.1 Drude Model – Microscopic Model for Macroscopic Electron Transport

To obtain a microscopic description of the bulk electronic transport, we shall consider the semi-classical model of charge transport introduced by Paul Drude (1900)[10] that treated electrons are not unlike gas particles. Drude conceived for metals an electron gas in equilibrium with a positive metal ion structure. According to the effective mass m of an electron in its environment, we can express the drift velocity v_d of the electron in an electric field as $v_d = p/m$, where p is the linear momentum. Considering next that the electron experiences flow resistances due to scattering with other electrons, as well as the metal ion structure, Drude required that the rate at which electrons gain momentum

---

[10] P. Drude, Anal. Phys., **1**, 566 (1900).

Table 1.4 Properties of selected metals.

		Valency	u^1	ρ^2 [g/mol]	$n_e{}^3$ [10^{28} m^{-3}]
Alkali metals					
Lithium	Li	1	6.941	0.534	4.631
Potassium	K	1	39.0983	0.89	1.370
Cesium	Cs	1	132.9055	1.873	0.848
Alkaline earth metals					
Beryllium	Be	2	9.0122	1.85	24.715
Magnesium	Mg	2	24.305	1.74	8.619
Calcium	Ca	2	40.078	1.54	4.626
Transition metals					
Nickel	Ni	2	58.6934	8.90	18.259
Copper	Cu	1	63.546	8.96	8.488
Zinc	Zn	2	65.38	7.134	13.138
Post transition metals					
Aluminum	Al	3	26.9815	2.70	18.079
Gallium	Ga	3	69.723	5.91	15.308
Indium	In	3	114.818	7.31	11.498

1. Atomic mass unit: National Institute of Standards and Technology (NIST), Experimental data, Computational Chemistry Comparison and Benchmark Database Release 22 (May 2022) Standard Reference Database 101.
2. Molar density: Royal Society of Chemistry, Periodic Table.
3. Number density: Calculated based on the numbers provided (see Study Problems to Chapter 1).

from the electric field E, i.e., $\mathrm{d}p/\mathrm{d}t = eE$ (where e is the elementary charge) is balanced by the rate of momentum scattering losses, $\mathrm{d}p/\mathrm{d}t = mv_d/\tau_m$. With τ_m, Drude introduced an arbitrary scattering time,[11] which will be further discussed below. We can express the electron current density j by the product of the charge, e, the electron number density, n_e (see Table 1.4) and the drift velocity, v_d, i.e.,

$$j = en_e v_d \tag{1.35}$$

Substituting v_d from $eE = mv_d/\tau_m$ into Eq. (1.35), yields for the current density, $j = \left(ne^2\tau_m/m\right)E$. Finally, using Ohm's law of the electrical conductivity $\sigma = j/E$, which denotes the ratio of the current density and the electric field, Drude deduced, based on what was said above, the following microscopic model expression for the conductivity:

$$\sigma_e = \frac{n_e e^2 \tau_m}{m} \tag{1.36}$$

---

[11] τ_m is known as relaxation time.

Drude's model describes the diffusive current flow in macroscopic systems phenomenologically described by Ohm's law. While lacking any quantum mechanical consideration of electrons, it proved surprisingly accurate on the macroscopic scale. On the nanoscopic scale, however, the model breaks down when the conductor dimensions meet characteristic length scales, specifically, the *de Broglie wavelength*, λ, the *electron mean free path* (scattering length), L_m, and the *phase coherence length*, L_ϕ that are discussed next.

1.5.2 Characteristic Length Scales for Electron Transport

Louis de Broglie's thesis in 1924 brought forward the *wave-particle duality theorem* that assigned a corpuscular particle of mass m and velocity v a wavelength $\lambda = h/mv$, employing Planck's constant $h = 6.626 \times 10^{-34}$ J · s. The expression originated from Einstein's energy relation $E = h\nu = pc$ of the photon, where ν and c are the frequency and speed of light, respectively. Based on de Broglie's relation, particles confined to a scale λ behave like standing waves that discretize the energy spectrum. In other words, continuous classical mechanics breaks down, and kinetic energy is discretized. An example of a quantum-confined system is an electron trapped by the attractive potential in an atom. The electron can only exist at discrete places around the atom, also known as electron shells. In a conductive wire, the length scale to compare the de Broglie wavelength to is the circumference G of the wire. If G ~ λ, the circumferential transport is quantized, and hence, the transport along the wire is reduced to one dimension. Such a thin wire is named a *quantum wire*.

The second characteristic length scale to consider for electron conduction in a wire referred to as the *electron mean free path* L_m, is the average length an electron can freely travel without collisions. For a wire length $L < L_m$, the electron transport is called *ballistic*. Scattering can occur between electrons but also within the atom lattice. The former scattering process is known as electron-electron scattering, and the latter as electron-phonon scattering caused by lattice vibrations. Other scatters are impurities and defects. For $L \gg L_m$, the transport is *diffusive*. In the ballistic regime, $L < L_m$, the smallest possible conductance for any dimensional conductor is

$$G_o = 2e^2/h \tag{1.37}$$

known as *conductance quantum*. Equation (1.37) is derived in the Worked Problem below for a quantum wire. Most notable is that the conductance quantum is constant (7.72×10^{-5} S), independent of the size of the conductor. So is also its corresponding resistance, the *resistance quantum*

$$R_o \equiv 1/G_o = h/2e^2 \tag{1.38}$$

with 12.95 kΩ. Following this section, we will discuss further the implication of dimensional constraints on electric transport.

Worked Problem 1.5.1

Background: For quantum systems, the linear momentum p is expressed by h/λ, where h is the Planck constant. Introducing the wavenumber $k = 2\pi/\lambda$, which is a measure of how many times the wavelengths fit into 2π, we can rewrite the linear momentum as

$p = \frac{h}{2\pi}\frac{2\pi}{\lambda} = \hbar k$, having introduced the symbol $\hbar$ for $h/2\pi$. As the velocity is $v = p/m$, it follows $v = \hbar k/m$.

Problem: We shall derive the conductance quantum $G_o = 2e^2/h$ for a quantum wire given that (a) in a metal, the kinetic energy of electrons in the current is close to the Fermi energy, and (b) in 1D, the relation between the number density n (of a spin-1/2 system) and the Fermi wave number k_F is $n = 2k_F/\pi$.

Solution: We express the conductance of a 1D system in terms of the conductivity σ, as

$$G_e = \frac{\sigma}{L} = \frac{n_e e^2 \tau}{mL} \tag{1}$$

according to Drude's ballistic model for $L \leq L_m$. The mean free path is given by the drift velocity of the electron (here, the electron Fermi velocity $v_F = \hbar k/m$), and the scattering time τ, as

$$L_m = v_F \tau = L$$

that we equated with the system length L. Substituting for $n_e = 2k_F/\pi$ and $\tau = L/v_F$ into (1) yields

$$G_e = \frac{2k_F}{\pi}\frac{e^2}{mL}\frac{L}{v_F} = \frac{2}{\pi}e^2\frac{k_F}{v_F m} = \frac{2}{\pi}e^2\frac{k_F}{\left(\frac{\hbar k_F}{m}\right)m} = \frac{2}{\pi}e^2\frac{2\pi}{h} = \frac{4e^2}{h}$$

Now, this expression for the conductance is off by a factor of two, as we have to consider two scattering sites, at $x = 0$ and $x = L$. Thus, the final solution reduces to the conductance quantum

$$G_e = \frac{2e^2}{h} \equiv G_o$$

The third and final characteristic length scale to compare the system size L with is the phase coherence length L_ϕ. L_ϕ is the largest of the three characteristic length scales. If L is between L_m and L_ϕ the scattering processes are considered elastic and the particles move coherently, not unlike synchronized swimmers. For $L > L_\phi$, the electron scattering process is predominantly inelastic, which results in incoherent, diffusive, electron transport. The concept of phase behavior is most effectively illustrated by following the path of corpuscular particles through two parallel slits in an impenetrable wall, and recording the intensity impact on a screen, positioned at a large distance after the slits, as illustrated in Figure 1.11. We contrast the intensity impact, which is equivalent to the probability of particles impacting the screen at a particular screen location, with the intensity of a wave (e.g., light) that travels through the same slit contraption.

We find that the particle intensity $I_{1,2}$ on the screen is initially more prominent right behind the two slits until, after an extended period, a single convoluted intensity maximum establishes itself in the center of the screen, between the two slit projections. If we covered up one of the two slits and measured the intensity of impacts of the screen for one and the

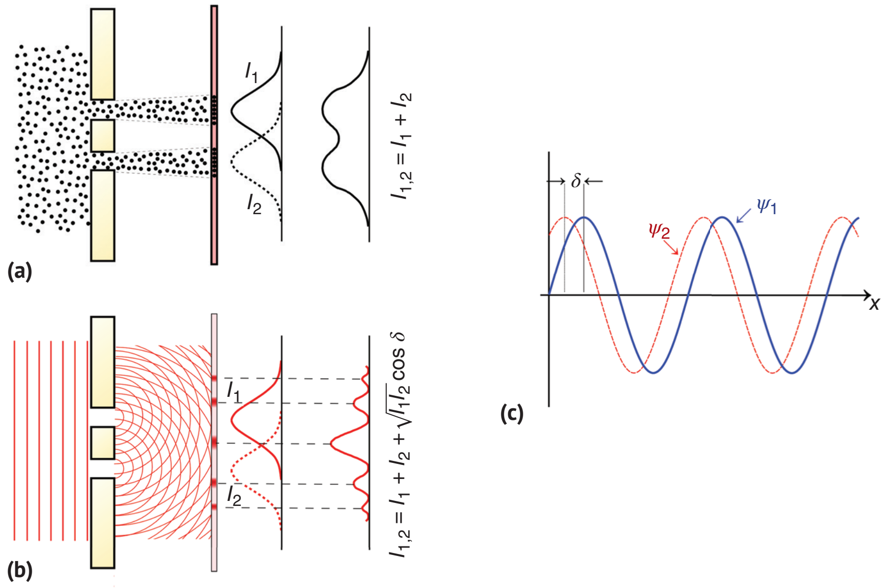

Figure 1.11 Double slit experiment of (a) corpuscular particles, and (b) waves. The wave diffraction in (b) is caused by (c), the phase relation of the two emanating waves from the slits.

other slit behind each slit, i.e., I_1 and I_2, we would find that the convoluted intensity $I_{1,2}$ is simply the sum, i.e.,

$$I_{1,2} = I_1 + I_2 \ \ \text{(for corpuscular particles)} \tag{1.39}$$

as illustrated in Figure 1.11(a).

Different is the situation for a wave that is passing through the slits. The two waves are expressed according to their wave functions, $\psi_i(x,t) = A_i\cos(kx - \omega t + \varphi_i)$,[12] $i = 1,2$, where A_i and ϕ_i represent their respective amplitude and phase. The intensity of a beam from a single slit is $I_i = |\psi_i|^2$ per unit area, while for the superimposed wave, the intensity is obtained from $I_{1,2} = |\psi_1 + \psi_2|^2$, which yields

$$I_{1,2} = I_1 + I_2 + 2\sqrt{I_1 I_2}\cos\delta \ \ \text{(for waves)} \tag{1.40}$$

We observe for waves a refractive pattern, Figure 1.11(b). The phase discrepancy of the two superimposed waves is captured with the relative phase δ. In the case of $\delta = (2n + 1)\pi/2$, $n = 0,\pm1,\pm2,\ldots$, the two waves superimpose incoherently, which results in an intensity pattern $I_{1,2}$ found for corpuscular particles, expressed by Eq. (1.53). Thus, we can say that classical particles behave intrinsically incoherently to each other. Waves, on the other hand, are capable of exhibiting any interference behavior, from constructive to destructive ones, that culminates in the intensity line pattern in Figure 1.11.

---

[12] $k \equiv 2\pi/\lambda$ is the wave number (λ, the wave length), and $\omega \equiv 2\pi\nu$ is the angular frequency (ν, the wave frequency).

This brings us back to the particles at hand, namely electrons. Electrons are not classical particles but quantum particles that are both particles and waves. As such, the probability of finding them on the screen behind the two slits yields a similar refractive pattern as for waves, Figure 1.11(b) found for light or water. In other words, electrons can move coherently, as we argued for electrons in the ballistic flow regime in a 1D wire. Elastic scattering also leaves the phase relation intact. Inelastic scattering, however, breaks the phase relation, and the particles move incoherently, typically referred to as diffusively.

1.5.3 One-dimensional Electron Transport

Electrical current transport through a quantum wire requires, like any transport, a driving force. For electrical transport, the driving force is given by a difference in the electrochemical potential, $\Delta\mu = \mu_1 - \mu_2$, measured at its leads of the conductor to two electron reservoirs. The resulting current of electrons with charge e can be expressed qualitatively by

$$I \propto e \sum_{n=1}^{N} \int_{\mu_1}^{\mu_2} D_{s,n}(E) f_n(E,\Delta\mu,T) v_n(E) T_n(E)\, dE \tag{1.41}$$

as derived in the Worked Problem below. We find with $D_{s,n}(E)$, the number of states in the conductor that can be populated with electrons, with $f_n(E,\Delta\mu,T)$, the probability of populating states with electrons, with $v_n(E)$, the electron velocities, and, with $T(E)$ the transmission probability. Assuming otherwise ballistic transport within the wire, the transition probability $T_n(E)$ takes into account that electrons can backscatter from the lead boundaries. With the sum from $n = 1, 2, 3, \ldots N$, it is indicated that the process is discrete due to the cross-sectional confinement.

Quantum confinements bring forward distinguishable states. On the macroscopic scale, where we find a continuous infinite number of states, we are typically ignorant of the fact that it requires a state for electrons to exist in a system. We can think of an electrical conductor that connects two electron reservoirs as a train that connects two locations. It requires seats in the train to transport passengers between two locations. The train is typically made up of a series of wagons. In a bulk system, the wagons are connected so that the passengers can populate the entire train. In a quantum-constrained system, the wagons are in the interior isolated from each other.

Let us fine-tune our train model. First, we consider a bulk system. In Figure 1.12(a), we replace a train composed of multiple wagons that are all accessible from the inside with a single wagon that can be expanded. This allows us to increase the capacity of the train, more or less, continuously. We introduce a loading potential $E_{\text{pot}} = ½\, kx^2$, where x stands for the length of the wagon, and k represents a system intrinsic stiffness that is visualized with horizontal springs along the wagon that can be extended. Ignoring that people and chairs come quantized, our train can increase its passenger loading capacity linearly with potential changes, Figure 1.12(b). Now we switch to the quantum perspective of our train composed of N rigid and isolated wagons. We assume our train station to be a dead-end railway station, where trains can only enter and exit from one end. To penetrate into the station and reach the passengers on the platform, the train has to do work against a spring, as depicted in Figure 1.12(c, d). Consider now that based on the applied force (equivalent

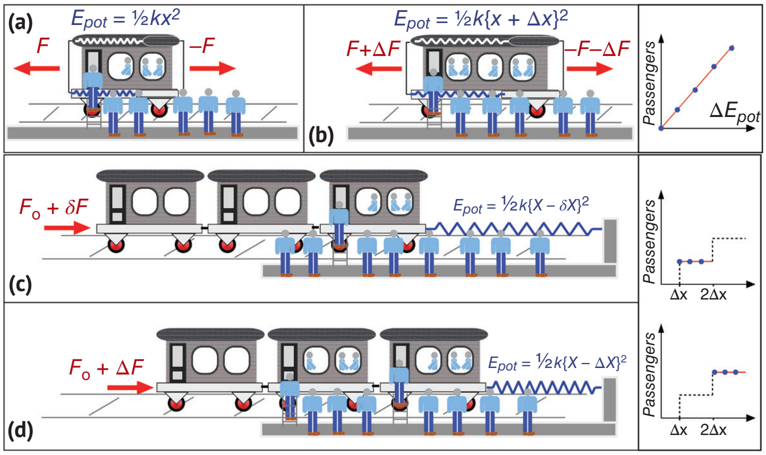

Figure 1.12 Train model to contrast bulk transport to quantized transport. (a) Single wagon train that can be (b) continuously extended. (c–d) Multiple size-defined isolated wagons, mimicking a discrete quantized system. Loading is restricted to one wagon for (c) and to two wagons for (d).

to the applied voltage in an electrical system), only a limited number of wagons can reach the passengers. This is shown in Figure 1.12c, d, where only one or two wagons reach the passenger platform, respectively. Thus, as each wagon can only be loaded from the outside, only the seats (called *states*) of the wagons (*modes*) at the platform can be populated with passengers (*electrons*). With increasing force (bias), a critical value, ΔF, can be reached that allows for an additional wagon to be loaded. The sudden availability of a new mode (also called subband) abruptly changes the number of passengers (electrons) that can be transported. Thus, it comes as no surprise that the current-voltage curves, as discussed further below, show discontinuities. In the case of a 1D wire (or contraption), the current-voltage relation reveals qualitatively a staircase behavior.

After working through the details (see Worked Problem below), the resulting current-voltage relation for ballistic transport through a 1D quantum contraption is

$$I = \left(\frac{2e^2}{h}N\right)V \tag{1.42}$$

providing a system size-independent conductance,

$$G_e = \frac{I}{V} = \left(\frac{2e^2}{h}\right)N = NG_o \tag{1.43}$$

This result, known as the *Landauer formula*, is the total mode multiple (N-multiple) of the conductance quantum G_o, derived earlier. It applies to ballistic 1D electrical systems, such as nanowires, point contacts, and devices with 1D contraptions. Should the transition be hindered by scattering, most specifically, reflective scattering at the leads, the expression (Eq. (1.43)) can be extended with the mode-dependent transmission probability $T_n(E)$ to yield

$$G_e = \frac{2e^2}{h}\sum_{n=1}^{N} T_n(E) \tag{1.44}$$

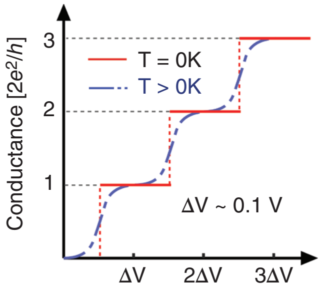

Figure 1.13 Quantized staircase-like conductance for 1D quantum wires at zero Kelvin. The conductance increases in increments of the conductance quantum for every ΔV increase and is constant in between. The step function smears out with increasing temperature.

More details about $T_n(E)$ are found in the Worked Problem below. Figure 1.13 provides an illustration of the staircase-like conductance for fully transmitting modes ($T_n(E) = 1$) at zero absolute temperature. For finite increasing temperatures ($T > 0$ K), the staircase behavior washes out, until it is no longer recognizable at room temperature. The reason for it are scattering effects inside the wire that we discussed earlier, which brings forward a diffusive electron transport.

Worked Problem 1.5.2

Problem: We shall derive the current-voltage relation for a 1D quantum wire at absolute zero Kelvin. The conduction shall be ballistic.

Solution: Let us return to our earlier expression for the electron current density, Eq. (1.35), and express the current for a 1D quantum wire as[13]

$$I = e\left(n_e^{1D}\right)v_d \tag{1.45}$$

The electron number density $n_e^{1\text{D}}$ can be expected to depend on the number of available states in the wire, as well as the probability of being populated. Both terms of $n_e^{1\text{D}}$, as well as the electron drift velocity $v_d = v(E) = (\hbar)^{-1}\partial E/\partial k$ depend on the total energy $E = E_n(k)$ of the electron, which is given by the sum of the kinetic energy $E_{kin} = p^2/2m = \hbar^2k^2/2m$, attributed to the unconstrained directional flow in z along the wire, and the quantized potential energy $E_{\text{pot}} = (n + ½)h\nu$, with the quantum number or mode number $n = 0, 1, 2, 3, \ldots,$[14] accredited to the cross-sectional xy confinement. For a given quantum state n, we rewrite the product $n_e^{1\text{D}}v_d$ as $n_{e,n}^{1\text{D}}(E)\,v_n(E_n)$.

The electron number density is given by the sum of the filled electronic states per wire length. We express this with an integral over the product of the *density of states* $D_s(E)$ and the Fermi-Dirac distribution function $f(E - \mu, T)$, i.e, $n_e^{1\text{D}}(E) = \int D_s^{1\text{D}} f(E)\,dE$.

Combining the terms in Eq. (1.45) yields for a single-mode wire.

$$I_n = \frac{1}{2}e\int_{\mu_1}^{\mu_2} D_{s,n}^{1\text{D}}(E)[f(E - \mu_1, T) - f(E - \mu_2, T)]_n v_n(E_n)\,dE \tag{1.46}$$

---

[13] We absorbed the cross-sectional area in the electron number density.

[14] A derivation of this expression will be provided in a later chapter.

In so doing, the two reservoirs are represented by their electrochemical potentials $\mu_i (i = 1, 2)$, and with $f(E - \mu_1, T) - f(E - \mu_2, T)$ corresponding probabilities to add or remove electrons from states in the wire. The two potentials define the bias voltage of $V = (\mu_1 - \mu_2)/e$. The prefactor of ½ originates from the electron spin. So far, we have considered the electron transport to be perfectly ballistic.

Next, we consider N electron transfer modes and consider a backscattering probability $T_n(E)$ at the two boundaries to the reservoir, $T_n(E)$, that is

$$I = \frac{1}{2} e \sum_{n=1}^{N} \int_{\mu_1}^{\mu_2} D_{s,n}^{1\mathrm{D}}(E)[f(E - \mu_1, T) - f(E - \mu_2, T)]_n v_n(E_n) T_n(E)\, dE \tag{1.47}$$

For small voltages, we can consider the backscattering probability to be independent of energy, i.e., $T_n(E) = T_n(E_F)$, which let us move $T_n(E_F)$ outside the integral:

$$I = \frac{1}{2} e \sum_{n=1}^{N} T_n(E_F) \int_{\mu_1}^{\mu_2} D_{s,n}^{1\mathrm{D}}(E)[f(E - \mu_1, T) - f(E - \mu_2, T)]_n v_n(E_n)\, dE \tag{1.48}$$

As the probability of backscattering vanishes for long distances, i.e., $T(E_F) \to 1$ for $L \gg \lambda_B$, where λ_B stands for the backscattering mean free path, and L the wire length, $T(E_F)$ is well described by

$$T(E) = \frac{\lambda_B(E)}{\lambda_B(E) + L} \tag{1.49}$$

Considering that the probability of populating the states with electrons (spin ½ particles, also known as Fermions), is given by the Fermi-Dirac distribution

$$f(E - \mu, T) = \frac{1}{1 + e^{(E-\mu)/k_B T}} \tag{1.50}$$

we find for ultralow temperature that $\int f(E - \mu_1, T) - f(E - \mu_2, T)\, dE \to 1$ for $T \to 0$ K, and thus, the current expression rewrites to:

$$I = \frac{1}{2} e \sum_{n=1}^{N} T_n(E_F) \int_{\mu_1}^{\mu_2} D_{s,n}^{1\mathrm{D}}(E) v_n(E)\, dE \tag{1.51}$$

Now, we substitute for the 1D density of states[14]

$$\begin{aligned} D_s^{1\mathrm{D}}(E) &= \frac{2}{\pi}\sqrt{\frac{m}{2\hbar^2}}\frac{1}{\sqrt{E}} \\ &= \frac{2}{\pi}\frac{dk}{dE} \end{aligned} \tag{1.52}$$

and for the drift velocity

$$v(E) = \frac{1}{\hbar}\frac{dE}{dk}$$

which yields:

$$I = \frac{2e}{h} \sum_{n=1}^{N} T_n(E_F) \int_{\mu_1}^{\mu_2} dE = \frac{2e^2}{h} \sum_{n=1}^{N} T_n(E_F) V \tag{1.53}$$

Rooted on the definition of the conductance as the ratio I/V, it follows

$$G_e = \frac{2e^2}{h}\sum_{n=1}^{N} T_n(E_F) = G_o \sum_{n=1}^{N} T_n(E_F) \tag{1.54}$$

that is a multitude of the conductance quantum G_o. In the case of fully transmitting modes, i.e., $T_n(E_F) = 1$ for all n up to N, the electrical conductance is

$$G_e = \frac{2e^2}{h}N \tag{1.55}$$

Based on our discussion in this section, we found that electronic transport differs substantially in quantum-confined systems from bulk systems, as contrasted in Figure 1.10 with the qualitative behavior of conductance. While pure dimensionality plays a role in transport quantization, i.e., via the electron number density, it is not the sole responsible factor. One should also consider the size dimension through which transport occurs (e.g., the diameter D of a wire) with respect to the electron wavelength λ. In narrow contacts (known as quantum point contacts), as depicted, for instance, in Figure 1.10(b), at which an electron transport conduit is opened up that is smaller than the characteristic *de Broglie* wavelength of the electrons, we found scattering within the phase conduit becomes negligible compared to scattering at the conduit boundaries. This changes the underlying transport principle from ohmic diffusive scattering to ballistic mode-dependent transport through the quantum contraption. The dual concept of describing a corpuscular particle, like the electron, also as a wave, is inherent for small particles and forms the basis for describing quantum mechanical systems. We will discuss this aspect in greater detail in later chapters, such as the working principle of electronic switching devices involving quantum dots, Figure 1.10(c), which we briefly address here.

1.6 Acoustic Transport and Dimensionality

In our discussion involving electronic quantum point contacts, we addressed aspects of wave propagations under dimensional constraints. Similarly to charge transfer involving electrons, dimensionality also plays an important role in wave propagations involving light (i.e., photons) and energy and momentum transport via acoustic waves (phonons). Under nanoconfinement, fundamental laws and principles are again put to the test. For instance, one of the fundamental laws of wave propagation that works for sound, more specifically phonon waves, is the Huygens principle, which is put into question in lower dimensions, as hinted at earlier.

While Christiaan Huygens' focus in his treatise in 1678 was on optics, its implications apply to many wave propagation phenomena. Huygens–Fresnel principle states that every point on a wave front may be considered a source of secondary spherical wavelets that spread out in the forward direction at the same speed as the overall wave front. The new wave front is the tangential surface to all of these secondary wavelets, Figure 1.14. The principle is understood to apply equally to any point of constant phase. Based on Huygens, we expect from an incident involving a wave propagation event with a well-defined beginning

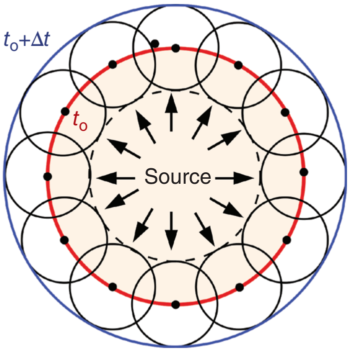

Figure 1.14 Huygens principle: A wave propagates through a medium where each point on the advancing wave front (red solid line) acts as a new point source of the wave.

and end, such as transmitting a signal that starts at t_o and ends at t_1, that the duration of the event is experienced the same at any point in space. This is true for light that emanates from a light bulb. It shines for the same time period regardless of the observer's distance from its source.

How about a surface wave in water that was initiated by dropping a pebble in it? Huygens' principle does not apply. The closer the observer is to the pebble the longer the incident occurs. The reason is the difference with which the wave dies out at a given location. The light emanating from the light bulb possesses a well-defined trailing edge at $t = t_2$ that moves as fast as the wave front, after which there is no signal. On the other hand, the waves on the water surface possess a highly defuse trailing boundary that has the observer theoretically experience the wave over an infinite period of time, although at a very small amplitude. Why that difference? The answer to this question is rather stunning.

The reason for the observed difference in behavior is found neither in the wave source nor the medium through which the waves travel, but plainly in the mathematical solution of the $N = 1, 2, 3, \dots$ N-dimensional wave equations of a scalar field[15] ψ, given as

$$\sum_{n=1}^{N} \frac{\partial^2 \psi}{\partial x_n^2} = \frac{1}{c^2}\frac{\partial^2 \psi}{\partial t^2};\ \psi(x_1, \dots x_N, t) \tag{1.56}$$

in which c represents the wave velocity. The scalar field is explicitly dependent on time t. It turns out that Huygens' principle of "memory annihilation" behind the trailing edge of a disturbance only applies to odd dimensions (e.g., 1D and 3D waves) but is invalid for even-dimensional space (e.g., 2D waves). The practical consequences can be significant. It would mean for our fictitious 2D world, *Flatland*, addressed earlier, that listening to sound (e.g., a radio) would be very challenging, as the accumulated remnants of prior sound messages would generate substantial background noise.

Lord Rayleigh discovered that acoustic waves, propagating over the surface of a body with a small penetration distance into the interior of the body, travel with a velocity independent of the wavelength and slightly smaller than the velocity of equivoluminal waves propagating through the body. It has been found that the so-called Rayleigh waves,

---

[15] Scalar waves are frequently described as standing waves, implying they do not move through space but exist as stationary patterns of energy.

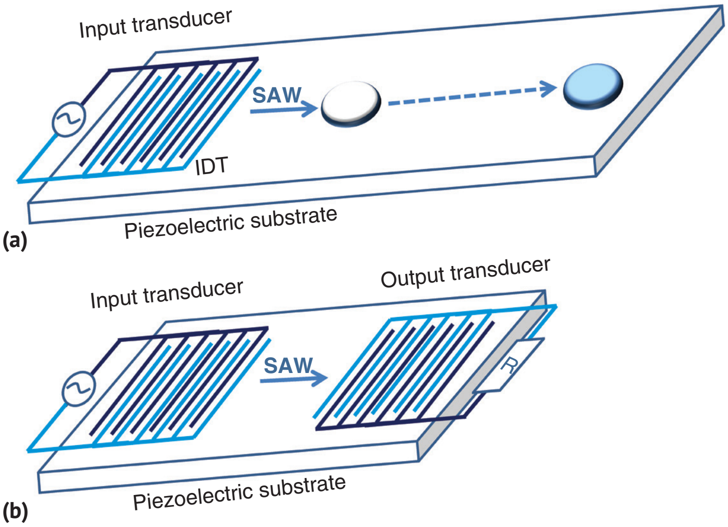

Figure 1.15 Surface acoustic wave (Rayleigh wave) applications in (a) microfluidics as fluid actuators illustrated here with moving a water droplet, and in (b) telecommunication devices as signal transducers.

which diverge in two dimensions only, acquire a continually increasing preponderance at great distances from the source.[16] This two-dimensional effect of wave propagation is very important in the study of seismic phenomena.

The so-called surface acoustic waves (SAW) have found applications in actuators (i.e., for pumping, mixing, and jetting) in small-scale systems of microfluidics, as illustrated in Figure 1.15(a) and are part of electronic devices in telecommunications products, depicted in Figure 1.15(b). Based on the transduction of acoustic waves, SAW devices are employed as signal filters, oscillators, and transformers. The generation of SAW involves an oscillating electrical signal applied to the interdigitated transducer (IDT) using a *radio frequency* (*rf*) signal generator and power amplifier. The SAW that propagates across the substrate, as a Rayleigh wave, possesses a wavelength λ in accordance with the dimension of the IDT finger width and spacing, both of which are $\lambda/4$.

The wave equation, Eq. (1.56), introduced above, has wide applications. It also applies to EM waves, as well as waves involving atomistic particles, such as electrons.

1.7 Critical Molecular Response Times in Nanoconstrained Systems

In our prior discussion on material behavior under shear (Section 1.3.1), we pointed out that intrinsically a material can respond to an external force instantaneously (i.e., elastically) or time-delayed (i.e., viscously or plastically) depending on the material phase

---

[16] A. E. H. Love, *A Treatise on the Mathematical Theory of Elasticity*, Dover Publications New York, 2011.

behavior or structure. We established that a perfect elastic response is rate-independent, while any viscous response is rate-dependent. Furthermore, we argued that the response underlying material properties can be altered by the introduction of interfaces that consequently reduce the degrees of freedom of the molecules to move and adjust to imposed stresses.

In this section, we tie the relevant macroscopic material properties, such as the elastic modulus, to molecular parameters that capture molecular mobility. More specifically, we illuminate intrinsic molecular response times. As our interest is in nanometer-constrained systems, we pick here, as the instructive process example, an interfacial process that has been relevant to mankind for millennia, namely frictional dissipation between two solid interfaces. The interface through which energy is actively dissipated is on the single-digit-nanometer scale. Within this size regime, unlubricated "dry friction" and ultrathin film lubricated friction occurs. As a film with a thickness on the nanometer scale shows predominantly solid-like behavior, we shall dub the field in focus here "solid friction." While bulk lubricated friction, involving fluids with thickness on the micrometer scale (or thicker), has been understood phenomenologically with Reynolds' adjusted Navier Stokes equation since the end of the 19th century,[17] a proper, as well as theoretical understanding of solid friction has evaded mankind until the second half of the 20th century. That is up to the early 1950s when Frank Bowden and David Tabor developed the *adhesion theory of friction*.[18] In the following decades, experimental and molecular modeling tools were developed that allowed nanoscopic experiments and interpretations.[19,20]

Typically, friction manifests a force that counteracts dissipatively the motion of two solids in dry or lubricated contact. A century ago, it was assumed that the sliding friction force involving dry contacts was independent of the sliding velocity (Amonton's third law). Over time, however, considering the plasticity of solid interfaces, rate dependences were considered. With the development of a scanning contact tool known as the *Atomic Force Microscope* (AFM) in the late 1980s, Figure 1.16(a), the friction rate dependence could be traced down to molecular dissipation interactions, known as Van der Waals (VdW) interactions. In other words, it was recognized that plasticity in the interface was not necessary for friction forces to be rate-dependent, as illustrated in Figure 1.16. We will discuss in the following an excerpt of the frictional shear behavior of a thin polymer film, and find the molecular intrinsic molecular response time to external stresses of significant relevance.

Here in Figure 1.16(b), the oppositely directed dissipative force response $F(x)$ to contact sliding of an AFM tip over a molecularly corrugated lipid surface is shown. Its qualitative behavior, at low velocity on the order of 1–10 nm/s, manifests a stick-slip solid-like phenomenon. In Figure 1.16(c), an amorphous glassy polymer that was scanned similarly to the molecular system with an AFM tip, Figure 1.16(b), reveals a dissipative force response distribution $F(v)$ in velocity v. The $F(v)$ distribution captures with its peak a material-specific relaxation mode, or, a combination of modes. As we will see in our

---

[17] O. Reynolds, Phil. Trans. Royal Soc. of London, **177**, 157 (1886).

[18] F. P. Bowden and D. Tabor, "Friction and Lubrication of Solids, Part I," Oxford Univ. Press, London, 1954.

[19] Nanoscopic experiments on thin films: R.M. Overney et al., Nature, **359**, 133 (1992).

[20] Combined experiment and modelling: B. Bhushan, J.N. Israelachvili, U. Landman, Nature **374**, 607 (1995).

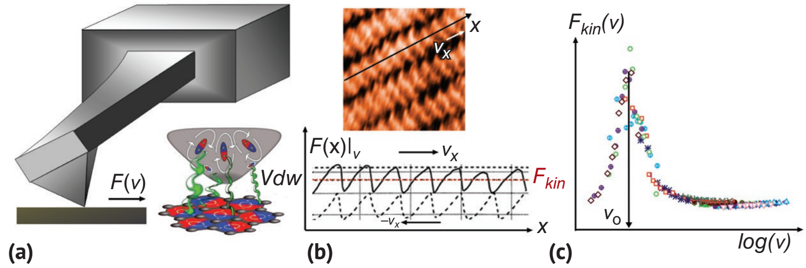

Figure 1.16 (a) AFM friction setup. Illustrated is the tip-apex/sample-surface VdW interaction. (b) Constant velocity, v, sliding over self-assembled lipid molecules, whose corrugated surface yields stick-slip friction forces, $F(x)|_v$, as a function of location x. Macroscopically observed static friction F_{stat} and kinetic (sliding) friction F_{kin} are matched to local molecular friction. (c) Frequency-dependent kinetic friction is shown around the critical material response velocity, v_o.

discussion that follows more generally, the peak is observed at a velocity at which the AFM spring deflection mode is locked with the intrinsic force gradient. At velocities decades higher, the friction-velocity behavior is logarithmic and as such, resembles an activated process with a well-defined activation barrier that can be attributed to specific molecular modes within the polymer.

1.7.1 Longitudinal Response to Stress – Maxwell Model

Any condensed matter system possesses intrinsic response times that can either be attributed to molecular or submolecular responses. Examples are molecular translations and side-group rotations. Furthermore, also collective molecular responses impact the response time, such as the earlier addressed stick-slip phenomena. Most of these conceivable feedbacks to mechanical stresses can be described phenomenologically in simplistic form with a network of springs and dashpots. The spring reflects a particular solid-like response and, the dashpot, a liquid-like system response. One of the most basic spring-dashpot combinations is the Maxwell model, depicted in Figure 1.17. With the Maxwell model, the material behaves *viscous* under very slow distortions, and, *elastic* for fast disturbances. At a moderate rate of deformation, the material will behave viscoelastic. To get a better understanding of the viscoelastic behavior of Maxwell solids, we analyze in the Worked Problem below the creep-recovery response of the depicted single spring-dashpot model, Figure 1.17.

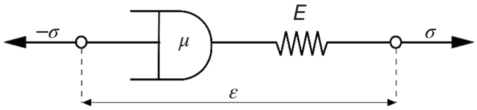

Figure 1.17 Maxwell model for longitudinal deformation: Combines a viscous damper of viscosity μ with an elastic “spring” of stiffness (Young’s modulus) E linearly. The external stress σ (force by unit area) and the material response (strain: ε length extension/original length) are related via the constitutive expression, $\dot{\varepsilon} = \dot{\sigma}/E + \sigma/\mu$, where the dot stands for the time derivate of the stress σ and the strain ε.

Worked Problem 1.7.1

Problem: We explore the strain versus time response (also called creep) to an instantaneous constant stress using Maxwell's viscoelastic model. (a) First, we derive the constitutive equation. (b) Next, we consider a stress $\sigma(t) = \sigma_o \varepsilon(t)$ of constant magnitude σ_o that is applied suddenly at time $t = t_o$ and then kept constant until entirely removed at $t = t_1$.

Solution:

a. We start with Newton's law, which is given as

$$F^e = k\Delta x^e$$

for the 1D distortion in x-direction of an ideal spring that is elastically extended or compressed by Δx^s. The proportionality factor k is a spring property known as spring stiffness. To extend Newton's law to uniaxial deformation, for instance, of a rod, we normalize the equation by the cross-sectional area A, i.e., introduce the stress $\sigma = F/A$, and by introducing the strain $\varepsilon = \Delta x^e/L$ as the original object length L normalized distortion, which leads to the stress-strain relationship

$$\sigma = E\varepsilon$$

The stiffness of the system is now expressed in terms of modulus, known as the elastic modulus E (also known as *Young's modulus*), and carries the units of pressure. For a fully viscous system, we use Newton's law of viscosity, i.e., consider the time derivative of the force law, i.e.,

$$\dot{F}^v = \mu\Delta\dot{x}^v$$

The material property to consider for a fully viscous process, as implied by the dashpot, is the viscosity μ. It shall be noted that the two x-distortions carry a different upper index, e or v, depending on whether the deformation is elastic or viscous respectively.

We consider next the Maxwell series model, as depicted in Figure 1.17, which yields for a given force (or stress) a total displacement of

$$\Delta x = \Delta x^e + \Delta x^v$$

or displacement rate of

$$\Delta\dot{x} = \Delta\dot{x}^e + \Delta\dot{x}^v$$

Substituting in the appropriate expressions from above, let us express the displacement rate as,

$$\Delta\dot{x} = \frac{\dot{F}^s}{E} + \frac{F^v}{\eta}, \text{ or}$$

$$\dot{\varepsilon} = \frac{\dot{\sigma}}{E} + \frac{\sigma}{\mu}$$

which is the sought-out constitutive equation for Maxwell's viscoelastic model.

b. Next, we explore the constitutive expression within the time interval $[-\Delta t, \Delta t]$ around the onset of a sudden stress, here expressed in integral form:

$$\int_{-\Delta t}^{\Delta t} \frac{\partial \varepsilon(t)}{\partial t} dt = \frac{1}{E} \int_{-\Delta t}^{\Delta t} \frac{\partial \sigma(t)}{\partial t} dt + \frac{1}{\mu} \int_{-\Delta t}^{\Delta t} \sigma(t)\, dt$$

which we can write as,

$$\varepsilon(+\Delta t) - \varepsilon(-\Delta t) = \frac{1}{E}(\sigma(+\Delta t) - \sigma(-\Delta t)) + \frac{1}{\mu} \int_{-\Delta t}^{\Delta t} \sigma(t)\, dt$$

We consider now $\Delta t \to 0$ for a sudden stress σ_o applied (or removed). As $\sigma(t)$ is finite, it follows

$$\int_{-\Delta t}^{\Delta t} \sigma(t)\, dt = 0$$

While for or a sudden applied stress $\varepsilon(-\Delta t) = \sigma(-\Delta t) = 0$, we can disregard $\varepsilon(+\Delta t)$ and $\sigma(+\Delta t)$ for a sudden stress removal. Thus, our constitutive equation reduces to

$$\varepsilon(\Delta t \to 0) = \frac{1}{E}\sigma(\Delta t \to 0)$$

for a sudden applied stress, which is equivalent to

$$\varepsilon(0) = \frac{\sigma_o}{E}$$

This manifests our initial condition when integrating the constitutive equation with respect to time. For a sudden applied stress σ_o that is kept constant over time, the constitutive equation simplifies to

$$\dot{\varepsilon} = \frac{\sigma_o}{\mu}$$

as $\dot{\sigma} = 0$. Integration yields

$$\varepsilon(t) = \frac{\sigma_o}{\mu} t + \text{const}$$

Considering the initial condition, the constant can be replaced by σ_o/E, which yields a linear strain-stress (or creep) function of the form,

$$\varepsilon(t) = \left(\frac{t}{\mu} + \frac{1}{E}\right)\sigma_o$$

that is depicted in Figure 1.18. We infer from the so-called *creep-recovery response function* of the Maxwell model that at the onset of sudden stress at $t = 0$, the strain increases instantaneously to σ_o/E due to the distortion of the spring. When later, the stress is suddenly removed at $t = t_2$, the energy stored in the spring is fully regained, seen as an instant drop in strain of magnitude σ_o/E, while the viscous strain is not recovered at all. We can divide the strain $\varepsilon(t)$ by the constant stress σ_o, and obtain the so-called *creep function* $J(t)$, i.e.,

$$J(t) = \left(\frac{1}{\mu} t + \frac{1}{E}\right)$$

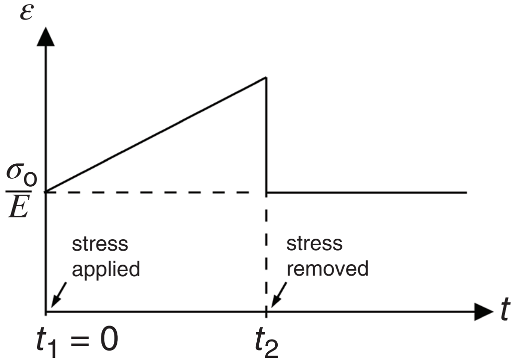

Figure 1.18 Maxwell creep-recovery response.

Instead of keeping the stress σ constant, as discussed in the Worked Problem above, the Maxwell model can also be explored by keeping the strain ε constant. Under constant strain ε_o, the constitutive equation simplifies to an ordinary differential equation in time of $\dot{\sigma}/E + \sigma/\mu = 0$, with the solution $\sigma = E\varepsilon_o \exp(-t/t_R)$, whereby we introduced the relaxation time $t_R \equiv \mu/E$. The relaxation time is a characteristic time of the viscoelastic material to relax after being stressed. In analogy to the definition of the *creep function* in the Worked Problem, we obtain the *relaxation function* of the Maxwell material, $G(t) = E \exp(-t/t_R)$, by dividing our solution of relaxation by the constant strain ε_o.

1.7.2 Shear Response to Stress

Moving now from longitudinal displacements to shear, let us consider a simple shear deformation of an isotropic material. The strain deformation is captured by the tangent of the shear angle, abbreviated simply as γ. For the shear stress, we will use the symbol τ. Considering elastic simple shear deformation, the constitutive equation is $\tau = G\gamma$, where G stands for the elastic shear modulus.[21] The stress-strain-rate relation is given by $\tau = \mu\dot{\gamma}$. Considering again the Maxwell model, the creep and relaxation functions are, $J(t) = (t/\mu + 1/G)$ and $G(t) = G \exp(-t/t_R)$, correspondingly, with the shear response time $t_R \equiv \mu/G$.[22]

A viscous response to a deformation manifests itself in a time delay in response, while the ideal fully elastic response is instantaneous. Thus, any realistic material will exhibit, to some degree, a time-delayed viscous response. To test the dynamic response, the material is typically strained with a cyclic history by employing a time-harmonic deformation. For shear-strained material, we consider the sinusoidal shear strain function $\gamma(t) = \gamma_o \sin(\omega t)$, where ω is the angular frequency. We keep the magnitude of strain γ_o small so that we can employ the *linear viscoelastic theory*, in which we consider the total deformation to stress as

---

[21] It can be shown that the longitudinal (Young's) modulus E is related to the shear modulus G for isotropic materials via the simple expression: $E = 3G$.

[22] G is known as *elastic shear modulus* and should not be confused with the relaxation function $G(t)$.

a simple sum of elastic and viscous deformations. Reworded, we express the corresponding stress, by a linear combination of elastic and plastic stresses. The Maxwell model provides one of the simplest examples. Accordingly, we introduce the single prime elastic stress component $\tau'(t) \equiv G\gamma_o \cos(\omega t)$ and the double prime viscous stress component $\tau''(t) \equiv \mu\dot{\gamma} = \mu\gamma_o\omega\,\sin(\omega t)$. By recognizing that $\sin(\omega t) = \cos(\omega t + \pi/2)$, we can rewrite the viscous stress component, as $\tau''(t) = \mu\gamma_o\omega\,\cos(\omega t + \pi/2)$. Comparing now the harmonic function of the strain $\gamma(t)$ with the corresponding harmonic stress $\tau(t)$, once steady state is reached, we find them to move synchronized in time, as shown in Figure 1.19(a), but shifted in-phase by an angle $\delta = \pi/2$. The two components formally manifest an instant elastic response and a time-delayed, fully viscous response. The time-delayed response is known in the literature as *time retarded response*.

For viscoelastic material, time retardation is captured by the phase lag δ, which is between $-\pi/2$ and 0, as illustrated by the dashed line in Figure 1.19(a). It is convenient to express with Euler's formula[23] the strain and the stress in complex notation that is,

$$\begin{aligned} \gamma^*(t) &= \gamma_o e^{i\omega t} \\ \tau^*(t) &= \tau_o e^{i(\omega t+\delta)} \end{aligned} \tag{1.57}$$

The amplitudes of both strain and stress carry the lower index "o" with $\delta \in (0, \pi/2)$.[24]

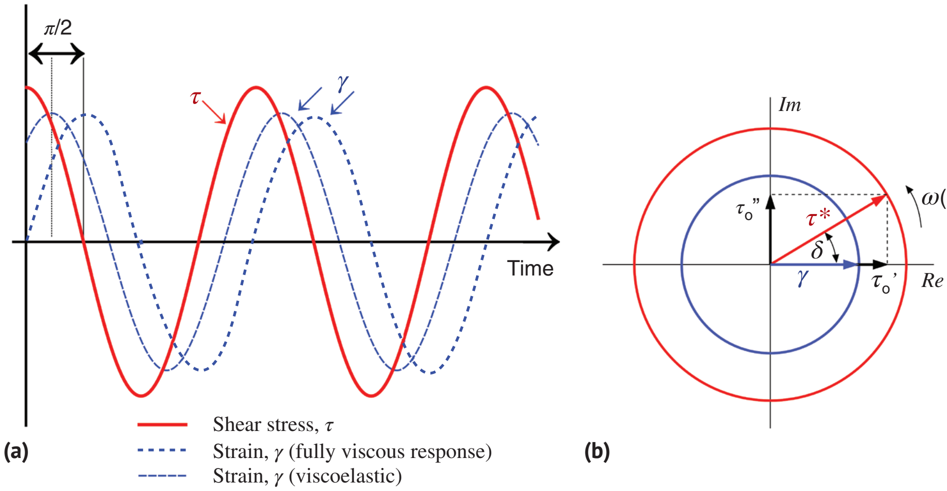

Figure 1.19 (a) Shows the synchronized by time-delayed (phase-shifted) response between the harmonic strain and stress. (b) Mathematical Euler construct of (a) with the real axis *Re* expressing ideal elastic and the imaginary axis *Im* fully viscous responses. A viscoelastic response is shown with the vector τ^* defined by (τ, δ) or (τ_o', τ_o'').

---

[23] Euler's formula: $e^{ix} = \cos(x) + i\,\sin(x)$ with $x = \omega t$, where ω is the angular frequency in [rad/s] and t is the time.

[24] We shifted the strain and stress harmonic function so that the strain is zero at $t = 0$, with the stress harmonic function to be zero at $t = -\delta/\omega$. As only the relative position of the two harmonic functions matters, the zero value of the time axis can be chosen arbitrarily.

The situation is depicted in Figure 1.19(b) for an arbitrary viscoelastic material by the complex stress vector τ^*, which can be expressed in Cartesian coordinates (τ_o', τ_o''), as $\tau^* = \tau_o' + i\tau_o''$, and polar coordinates (τ, δ), as provided in Eq. (1.57).

Accordingly, we can introduce the *complex linear viscoelastic modulus*, $G^* = G' + iG''$, with the elastic in-phase response, $G' = (\tau_o'/\gamma_o) = (\tau_o/\gamma_o)\ \cos\delta$ and the viscous out-of-phase response, $G'' = \tau_o''/\gamma_o = (\tau_o/\gamma_o)\ \sin\delta$. From these expressions, as well as by inspection of Figure 1.19(b), we find with the so-called *loss tangent*, $\tan\delta = G''/G'$, a relationship between the storage modulus G', the loss modulus G'', and the phase angle or phase lag δ.

In the Worked Problem above, we derived the constitutive equation for the Maxwell model as

$$\dot{\varepsilon} = \frac{\dot{\sigma}}{E} + \frac{\sigma}{\mu} \tag{1.58}$$

for a longitudinal deformation, which we can rewrite for simple shear, as

$$\dot{\gamma} = \frac{\dot{\tau}}{G} + \frac{\tau}{\mu} \tag{1.59}$$

If we now substitute the complex stress and strain expression from Eq. (1.57), we obtain, after some algebraic work, the following expressions for the storage and loss moduli:

$$G' = \frac{G(\mu\omega)^2}{G^2 + (\mu\omega)^2} = G\left(1 + \left(\frac{G}{\mu\omega}\right)^2\right)^{-1} = G\left(\frac{(\omega t_R)^2}{1 + (\omega t_R)^2}\right) \tag{1.60}$$

$$G'' = \frac{G^2\mu\omega}{G^2 + (\mu\omega)^2} = G\left(\frac{G}{\mu\omega}\Bigg/\left(1 + \left(\frac{G}{\mu\omega}\right)^2\right)\right) = G\left(\frac{\omega t_R}{1 + (\omega t_R)^2}\right) \tag{1.61}$$

where we substituted μ/G with the relaxation time t_R.

1.7.3 Dissipative Two-Dimensional Shear Response

Continuing with our discussion on shear by transitioning to the nanoscopic process of interfacial friction, we introduce the Deborah number, $De \equiv t_R/t$, the ratio between the relaxation time, t_R, and the time of observation t. The observation time is equivalent to the time the system is perturbed by frictional sliding. The dimensionless Deborah number quantifies the capability of a material to react to an external disturbance. This leads back to our discussion of a viscoelastic response that lies between an instantaneous solid-like response and a sluggish, time-delayed, out-of-phase fluid-like response.

To connect friction to our discussion on viscoelastic responses, we recognize that friction is a dissipative process, which it has in common with the viscoelastic loss modulus G''. If we substitute for $\omega = 2\pi/t$ into Eq. (1.61), we can express the loss modulus in terms of the Deborah number, i.e.,

$$G'' = G\frac{(2\pi)De}{1 + (2\pi)^2 De^2} \tag{1.62}$$

Considering next a uniformly exerted stress velocity v, which is applied to a spring-dashpot system, we can model the loss modulus for the relative sliding motion of two opposing surfaces in either direct contact or separated by a condensed lubricant film, as

$$G'' = \frac{F_o}{A}\left(\frac{De}{1 + De^2}\right) \tag{1.63}$$

with redefined $De = v/v_R$, the intrinsic material response velocity v_R, and $G = F_o/A$. While F_o represents a conservative intrinsic force of the interface or the lubricant that resists deformation, A is the corresponding shear area over which the force is acting. The product $G''A$ is found to dominate the nonconservative, dissipative sliding force, known as friction force F, as shown in Figure 1.20, as long as the sliding velocity v is within the vicinity of v_R, i.e., $De \sim 1$. We can consider $G''A$ for $De \sim 1$, as the "macroscopic intrinsic" response to sliding motion.

If the sliding velocity v is removed from the relaxation peak, viscous forces are more prominent, and we consider the rate dependence of the friction force. In the case of an ideal liquid, i.e., a perfectly viscous system, the force rate dependence is linear, as discussed

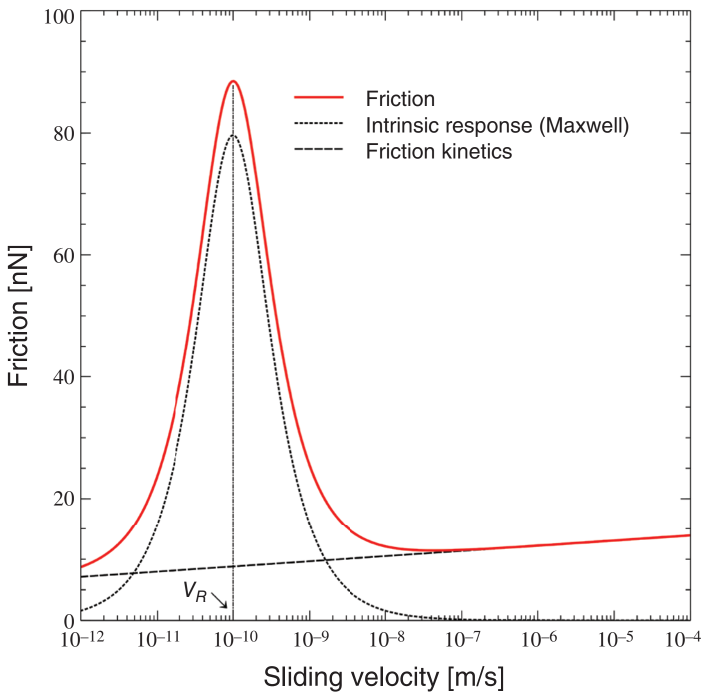

Figure 1.20 Friction on glassy PtBA at a reference temperature of 315 K modeled based on Eq. (1.65). Parameters: $a = 0.846$ N, $b = 17.277$ N, $V_R = 1.0 \times 10^{-8}$ m/s, $F_o = 159.37$ N. Sliding occurred at constant normal force of 2.05×10^{-8} N at close zero humidity (adapted from [26]).

earlier. For a realistic solid system, however, the dynamic portion of the friction force F_d is best described by[25]

$$F_d = a\ \ln(v) + b \tag{1.64}$$

which takes into account that frictional sliding is an activated process, not unlike a reaction with its distinct reaction kinetics. This is similar to our discussion earlier, when we introduced a simple jump model to describe the stick-slip phenomenon, Figure 1.7(c). The dynamic portion of friction is characterized by jump distances ξ and jump rates v, and thus, by temporary microscopic jump velocities $v_o = \xi v$. Based on its stochastic nature of dynamic friction, we can expect that material phase structures can have a significant impact on the magnitude of the jump parameters, as shown in Table 1.5.

For crystalline (highly structured) materials, such as self-assembled monolayers of octadecylphosphonic acid (ODPA), the jump velocity can be expected on the order of 100 m/s. That is by three orders of magnitude exceeding the one of solid polymer glasses, such as poly(tert-butyl acrylate) (PtBA).[26] In the glassy state, the polymer backbone can relax via local individual crankshaft rotations of chain segments, known as a-relaxation. The glassy solid phase is found in polymers at temperatures below the glass transition temperature T_g. Above T_g but below melting, the polymer is in a solid rubbery phase, for which the jump velocity v_o reduces by orders of magnitude from the one of the glass. The origin of the rubbery behavior of the polymer above T_g is the collective occurrence of the rotational crankshaft motion in polymer chains that allow the entire chains to move (reptiles) through the matrix. Its relaxation mode is known as ɑ-relaxation.

If we now add the kinetic portion of friction F_d, Eq. (1.64), to the macroscopic Maxwell component $G''A$, Eq. (1.63), the total friction force is

$$F_F = G''A + F_d = F_o\left(\frac{De}{1 + De^2}\right) + a\ \ \ln(v) + b \tag{1.65}$$

an expression that was confirmed experimentally with glassy polymer PtBA at a reference temperature of 315 K, Figure 1.20.

Table 1.5 Intrinsic jump parameters of solids based on material structure.

Solid material phases	Crystal*	Amorphous glass*	Rubber*
Jump velocity, v_o	~100 m/s	~0.1 m/s	~10^{-5}–10^{-4} m/s
Jump distance, ξ	~1 nm	~1 nm	~10–10^2 nm
Jump frequency, $\nu = v_o/\xi$	~100 GHz	~0.1 GHz	~0.1–10 kHz

*Order of magnitude.

---

[25] F. Heslot et al., Phys. Rev. E., **49**, 4973 (1994); S.E. Sills and R.M. Overney, Phys. Rev. Lett., **91**, 095501 (2003).

[26] D.B. Knorr et al. J. Chem. Phys., **134**, 104502 (2011).

We see that when the sliding velocity v matches the local backbone crankshaft velocity (α-relaxation) of $v_R = 0.1$ nm/s, the Maxwell component of friction dominates. Away from v_R, F_d dictates the friction response, or more accurately, the "lateral" response to shear. It shall be noted that by changing the velocity, we change the time of perturbation. As a change in the time observation window can be perceived as a change in temperature, based on the *time-temperature superposition principle*,[27] we can rescale time with temperature, and vice versa. In other words, by moving to faster and faster sliding velocities, the temperature of observation can be driven beyond the glass transition temperature. At this point, the cooperative motion of crankshafts, the γ-relaxation mode, becomes available. As a consequence, we will be able to couple with the shear displacement to the γ-relaxation mode, and thus, can expect a similar increase in friction as observed at 0.1 nm/s with the α-relaxation. The critical sliding velocity for PtBA to reach the γ-relaxation mode can be expected in the range of 1–10 nm/s.

The difference between changing the sliding velocity to mimic an increase in temperature versus actually increasing the temperature to above T_g is found in the parameters of F_d. The two parameters a and b in Eq. (1.64) are dependent on the molecular interactions in the polymer, which are significantly changed if a polymer transitions from a glass to a rubber state. On a structural level, the change manifests itself by an increase in free volume that allows the individual molecule to reptile through the polymer matrix. Thus, while our simple shear model can distinguish between the "static" and "dynamic" effects of friction, capturing the structural change is beyond its scope.

1.8 Miniaturization, Scaling, and System Constraints

The physical performance of a system is dependent on external parameters as well as on intrinsic properties and typically scales with changes in the dimension. To have a true measure of performance, it is common to consider the intrinsic performance, i.e., the volume normalized performance. An example is the power density of an engine. Volume normalization does, however, not imply that the physical performance of interest is size scale independent.

Let us look at a simple comparison of the power density of two engines that differ in volume size 1000-fold. The question to ask is, how do 1000 small engines perform compared to a single large engine of the same volume, V? Is their power density smaller, larger, or the same? The power P at a particular instant in time is given as the product between the force F and the velocity, v, that is,

$$P = Fv \tag{1.66}$$

To evaluate the scaling of the two system parameters F and v with the size dimension, we introduce the characteristic length dimension L. Considering the units of the force ($\text{kg} \cdot \text{m/s}^2$) and the velocity (m/s), we find that both F and v scale with L (i.e., $F \sim L$ and $v \sim L$) and consequently, we find the scaling law for the power, as

$$P \sim L^2 \tag{1.67}$$

---

[27] M.L. Williams, R.F. Landel, J.D. Ferry, Am. Chem. Soc., **77**, 3701–3707 (1955).

As we are interested in the power density, i.e., the power per unit volume P/V, we have to include the dimensional scaling of the volume, $V \sim L^3$, which results in the following scaling law

$$\frac{P}{V} \sim \frac{L^2}{L^3} = \frac{1}{L} \tag{1.68}$$

for the power density. As the length dimension, L, of a single small engine is $\sqrt[3]{1000} = 10$-fold smaller than the one of the large engine, the power density of 1000 small engines is

$$\frac{P}{V/1000} \sim \frac{1}{L/10} = \frac{10}{L}$$

10-fold the power density of a large engine. Thus, while conventional engines cannot be scaled down substantially, motors based on electrostatic forces are likely systems that could be miniaturized to produce ultrahigh power densities.

It is important to note that with the example above, we

- treated the material properties (i.e., the mass m, or more specifically, the material density $\rho \sim L^{\text{o}}$), as size-independent, and
- assumed that there are no other parameters affected by the change in volume.

Shrinking a system to the nanoscale, however, will, as we will see, impact the material properties and, thus, lead to changes in the scaling law upon miniaturization.

1.8.1 Phenomenological Shortcoming of the Scaling Analysis

1.8.1.1 Terminal Velocity of Liquid Droplets and Solid Particles

Let us briefly discuss an example that illustrates how changes in properties assumed to be constant can spoil the scaling analysis. We consider a rainwater droplet of radius r and density ρ_{H_2O} in the earth's gravitational field. Due to drag forces caused by the air, its velocity falling from a cloud quickly reaches a terminal velocity v_t. We shall assume, as per *Stokes' law*,[28] the terminal velocity can be obtained from

$$v_t^{st} = \frac{2gr^2\left(\rho_{H_2O} - \rho_{air}\right)}{9\mu_{air}} \tag{1.69}$$

where $g = 9.81\ \text{m/s}^2$ stands for the gravitational constant, and μ_{air} and ρ_{air} represent the dynamic viscosity and density of air, respectively. As we shall only be concerned with the size of the droplet that is captured by its radius, the terminal velocity scales as $v_tst \sim L^2$. Hence, if we compare a $r = 10\ \mu\text{m}$ droplet with an agglomerate of a thousand microdroplets of radius $r_a = 100\ \mu\text{m}$, the ratio of the terminal velocity

$$\frac{v_{t,a}^{st}}{v_t^{st}} = \frac{r_a^2}{r^2} = \left(\frac{100}{10}\right)^2 = 100$$

The comparison yields a 1000-fold increase in the terminal velocity for the droplet agglomerate compared to the microdroplet, which is further discussed in the Worked Problem below.

---

[28] The Stokes' law is an empirical observation for the frictional drag of a rigid object moving through a fluid.

Worked Problem 1.8.1

Problem: We compare the terminal velocity of microdroplets of $r = 10$ μm with that of rain droplets of $r_a = 100$ μm at 20 °C, assuming creeping flow.

Solution: Based on Stokes' Law, Eq. (1.69), with $\rho_{H_2O} = 998.2\ \text{kg/m}^3$ and $\mu_{\text{air}} = 1.825 \times 10^{-5}\ \text{Pa} \cdot \text{s}$ and $\rho_{\text{air}} = 1.02\ \text{kg/m}^3$, respectively, the terminal velocities are

$$v_t^{st} = \begin{cases} 0.012\ \text{m/s (microdroplet)} \\ 1.2\ \text{m/s (rain droplet)} \end{cases}$$

The average cloud droplet in heavy clouds has a terminal velocity of around 0.013 m/s. Without updraft, it would take such a droplet approximately 10 hours to reach the ground, assuming a typical low cloud base of 500 meters. With ascending air currents, microdroplets can stay for a very long time in clouds without producing rain.

The first assumption we made for our scaling law of the terminal velocity of raindrops is that we assumed that the streamlines that form in the air in the course of a falling raindrop are symmetrically surrounding (engulfing) the drop, as illustrated in Figure 1.21(a). This assumption holds for very slow velocities, known as *creeping flow*. At higher, more realistic velocities, we find a separation of the streamlines from the raindrop at the downstream region of airflow (i.e., after the equator toward the top of the raindrop) that results in the generation of two vortices at this location, Figure 1.21(b). The critical velocity at which streamline separation is obtained from the critical *Reynolds number* of Re = 8/5. The dimensionless Reynolds number is obtained from:

$$\text{Re} \equiv \frac{\rho_{air} v_t D}{\mu_{air}} \tag{1.70}$$

where D is the drop diameter, and v_t, the moving drop velocity observed from far away of the drop.

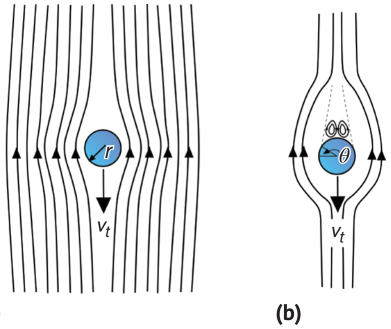

Figure 1.21 (a) Re < ~0.1: Stokes' potential flow around a sphere in a gravitational field passing through a fluid (air) at rest. The streamlines engulf the sphere in symmetric perfect alignment. (b) Re ∈ (10, 100): In the Oseen regime, the streamlines separate at an angle θ at the top of the sphere in the air fluid downstream region. Two symmetrical vortices form on top of the spheres that reduce the kinetic energy of the sphere and, with it, the terminal velocity.

For a microdroplet of 10 μm radius, we are in the limit of Stokes limit of $\mathrm{Re} < 0.1$, in the creep flow regime. However, for a droplet with a 100 μm radius and a roughly determined v_t of 1.2 m/s (based on Stokes), we are with $\mathrm{Re} \sim 10$, far exceeding the creep flow regime, as well as the streamline separation limit of $\mathrm{Re} = 8/5$. Taking streamline separation into account for larger droplets, which results in the generation of vortices, Figure 1.21(b), the terminal velocity has to be reevaluated. Based on *Oseen's law*, which is an extension of Stokes' law valid for $\mathrm{Re} > 1$, the following expression for the terminal velocity v_t was developed:[29]

$$\begin{aligned} &\frac{v_t}{v_t^{st}} = 1 + \frac{Ar}{96}\left(1 + 0.079Ar^{0.749}\right)^{-0.755} \\ &\text{with } Ar \equiv \frac{D^3 g\rho\Delta\rho}{\mu^2} \end{aligned} \tag{1.71}$$

The dimensionless number Ar is known as the Archimedes number. Oseen's expression above spans from $1.68 < \mathrm{Re} < 65$. Recent efforts[30] that considered a wide range of correlations covering solid spherical particles brought forward an explicit equation for the terminal velocity, applicable to micrometer and millimeter-scale particles in Newtonian fluids, as well as non-Newtonian fluids. In dimensionless form, the explicit expression of the terminal velocity[31] is:

$$\begin{aligned} v_t^* &= \left[\left(\frac{18}{\left(D^*\right)^{1+n}}\right)^{\frac{0.824}{n}} + \left(\frac{0.321}{D^*}\right)^{0.412}\right]^{-1.214} \\ &\quad n = 1 \text{ for Newtonian fluids (e.g., air)} \\ v_t^* &\equiv v_t\left(\frac{\rho_{\text{air}}^2}{g\mu\Delta\rho}\right)^{\frac{1}{3}} \text{ and } D^* \equiv D\left(\frac{g\rho\Delta\rho}{\mu^2}\right)^{\frac{1}{3}} \end{aligned} \tag{1.72}$$

Thus, while the expression above captures the complexity of the raindrop surrounding airflow, there is still another shortcoming of Stokes' scaling law that has to be addressed. It lays in our assumption that the water droplet's spherical shape is considered invariant at even fast flow velocities. In other words, we assumed water droplets to be non-deformable. Based on wind tunnel experiments, this assumption was shown to be far from valid when droplets reach millimeter size dimensions. Up to about 0.8 mm, the droplets are spherical. But for larger drops, the bottoms of the drops flatten out due to the air inertial resistance, which in turn increases the air frictional drag resistance that reduces the terminal velocity. This has been accurately recorded empirically with experiments by Ross Gunn and Gilbert Kinzer in 1948.[32] A fit to Gunn and Kinzer's data is plotted in Figure 1.22 and contrasted to both the terminal velocity of Stokes assuming potential flow around a sphere without streamline separation, Eq. (1.69), and for flow around non-deformable solid particles of spherical shape, Eq. (1.72).

---

[29] A.V. Nuyen et al., Int. J. Miner. Process, **50**, 53 (1997).

[30] V.C. Kelessidis, Chem. Eng. Sci, **59**, 4437 (2004).

[31] We express dimensionless quantity of the terminal velocity and the particle diameter with the * symbol.

[32] R. Gunn and G.D. Kinzer, **6**, 243 (1949).

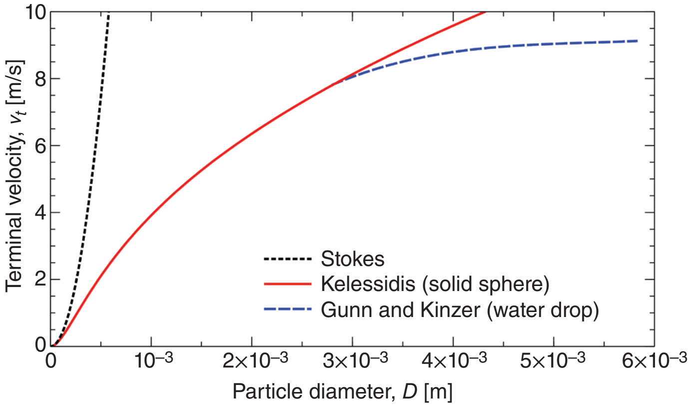

Figure 1.22 Terminal velocities for creeping flow (Stokes, Eq. (1.69)), and faster flow velocities for solid spheres (solid line, Eq. (1.72)) and rain droplets (dashed line fit to Gunn–Kinzer data) as a function of the droplet diameter. Deformations of droplets become effective for sizes above ~3 mm.

Beyond rain droplets, it shall be pointed out that the knowledge of the terminal settling velocity of solids in liquids plays an important role in many industrial applications, for instance, for fluidization processes, mineral processing, and mixing. Concerning mixing, the settling velocity plays an important role in the break-up of agglomerated nanoparticles and their phase dispersion. Further parameters that affect the terminal viscosity are particle coatings with respect to the passing fluid, as well as the shape of the particles. If it involves nanoparticles and tailored organics coatings, both nanotechnology and molecular engineering come into play.

1.8.1.2 Interfacial Constraints and Nanocomposite Membrane Permeability

When and how exactly a scaling law fails is sometimes hard to predict. Let us look at the example of small particles, or the inverted equivalent, the material matrix surrounding small particles. In the case of spherical silver metal particles, the atomistic structure remains bulk-like down to a diameter of $D \sim 1$ nm. Thus, we can expect the size-dependent properties of silver, for instance, to scale with a scaling law perceived from classical phenomenological laws and theories. For instance, the mechanical strain-stress relationship, given by the strain expression

$$\varepsilon = -\frac{4f}{3K}\frac{1}{D} \tag{1.73}$$

where f is the free surface stress and K the bulk modulus, is valid for silver nanoparticles down to the nanometer scale.

Taking an inverted view of nanoparticles by focusing on the change in the surrounding property, we consider silica (SiO_x) nanoparticles embedded in a dense polymer matrix. A thin SiO_x/polymer film that is open to both sides manifests a nanocomposite that, if exposed to a gas stream in crossflow, will exhibit membrane properties by allowing some of the gas molecules to sorb into the polymer phase and diffuse through it. Molecular sorption, as well as adhesion into polymers, is assisted by the free volume in polymers.

The gas mass transport through dense polymers is statistical, that is, driven mainly by concentration differences at two membrane sides. If we now consider that the embedded nanoparticles are non-permeable by the gas, the permeability of a homogeneous polymer matrix will depend on the volume or mass fraction φ of the implanted particles. This invites a scaling law for the permeability, with the scaling parameter φ. Based on a more detailed discussion in the Worked Problem below, the gas permeation flux J_A of the permeate A through a polymer-particle composite can be expressed, based on Fick's first law of diffusion, as

$$\begin{aligned} J_A &= -D\frac{dC_A}{dx} \\ &\approx -D\frac{C_{A,1}-C_{A,2}}{L_{\text{eff}}}\Bigg|_{L_{\text{eff}}=L\left(1+\frac{\varphi}{2}\right)} \\ &\approx -DS\frac{p_{A,1}-p_{A,2}}{L_{\text{eff}}}\Bigg|_{\substack{C_A=S(p,T)p_A \\ S\approx\text{const. (Henry's law)}}} \end{aligned} \tag{1.74}$$

The two material-specific coefficients, D and S, stand for the diffusion and the sorption coefficient, respectively. The product $P = DS$ with mass units $[\text{kg}\cdot\text{m}^{-1}\cdot\text{s}^{-1}\cdot\text{Pa}^{-1}]$ is also known as the gas permeability of the membrane.[33] More details on the Fick's law expression of the permeation flux in terms of the gas partial pressures p_A, and the scaling law of the effective diffusion length L_{eff} through the membrane of thickness L, are provided next.

Worked Problem 1.8.2

Problem: We shall estimate the effective distance it takes for a gas molecule to travel through a thin nanocomposite membrane in terms of the filler (nanoparticle) volume or mass fraction φ. Thereby, we consider spherical nanoparticles of diameter D, a membrane thickness L much smaller than any of its two plane dimensions allowing us to consider a 1D mass transfer system, as depicted here. Furthermore, we assume uniformly distributed particles in the membrane, as shown, and an expected value for the number of filler particles that a penetrating gas molecule A encounters, as[34]

$$\langle N\rangle = \left(\frac{L}{D}\right)\varphi$$

Solution: Based on Fick's first law, the mass flux is given by the concentration gradient of A, ∇CA, as

$$J_A = -D\nabla C_A$$

---

[33] On a molar basis, the permeability of a single gas species A is obtained from $P_A = \frac{V_A}{RT}\frac{\Delta p_A}{\Delta t A(p_F - \Delta p/2)}l$, where V_A is the constant permeate volume [m^2], R and T the gas constant ($8.314\ \text{Pa}\cdot\text{m}^3\cdot\text{mol}^{-1}\cdot\text{K}^{-1}$) and absolute temperature, respectively, Δt is the time for the permeate partial pressure to increase in the membrane from $p_{A,1}$ to $p_{A,2}$, $\Delta p_A = p_{A,1} - p_{A,2}$ is the partial pressure change from the start to the end of the pressure increase, p_F is the feed pressure and l and A are the thickness (direct transport length for permeation flux) and area of the membrane, respectively.

[34] J. Macher et al., Polymers, **14**, 3327 (2022).

where D is the diffusion coefficient or diffusivity. The concentration can be expressed in terms of the local partial gas pressure p_A and the sorption coefficient $S(p,T)$, as $C = S(p,T)p_A$. The sorption coefficient S can be assumed constant (Henry's law) if we limit ourselves to dense polymers with high free volume (such as poly(1-trimethylsilyl-1-propyne) (PTMSP) or polymers above the glass transition temperature), which lets us write for the permeation flux of A,

$$J_A = -DS\nabla p_A \approx -DS\left(\frac{p_1 - p_2}{L}\right) \equiv -P\left(\frac{p_1 - p_2}{L}\right)$$

in our 1D approximation. Note that we introduced the partial pressure at the upstream and downstream side of the membrane, p_1 and p_2, respectively, and the permeability $P = DS$. With the introduction of flux impermeable particles, the diffusion path L_{eff} is extended by the path tortuosity τ, as $L_{\mathrm{eff}} = \tau L$. The tortuosity τ is dependent on the filler volume or mass fraction φ. We can express the effective diffusion length through the membrane, as

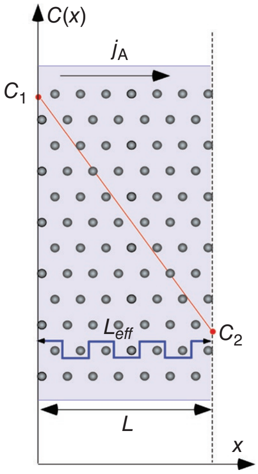

Figure P1.8.2 1D Mass flux through a polymer composite membrane.

$$L_{\mathrm{eff}} = L + \langle N\rangle \frac{D}{2}$$

by adding the evading distance of the particle radius times the number of encounters to the membrane thickness. We can rewrite this expression, as

$$L_{\mathrm{eff}} = L + \left(\frac{L}{D}\right)\varphi\frac{D}{2} = L\left(1 + \frac{\varphi}{2}\right)$$

With this, we can express the tortuosity as follows:

$$\tau(\varphi) = \left(1 + \frac{\varphi}{2}\right)$$

It is common to leave the external membrane parameters, as well as the partial pressures at the upstream and downstream regions of the membrane, untouched. The effect of tortuosity of the permeation flow due to the incorporated impermeable particles is incorporated into the diffusivity and sorption properties, i.e.,

$$\begin{aligned} D_{\mathrm{eff}} &= \frac{D_{\mathrm{o}}}{1+\varphi} \\ S_{\mathrm{eff}} &= S_{\mathrm{o}}(1-\varphi) \end{aligned} \tag{1.75}$$

where D_{o} and S_{o} reflect the diffusion and sorption properties for the particle-free (virgin) polymer membrane. The relative change in flux between a composite membrane and the homogeneous polymer membrane, $J_{\mathrm{eff}}/J_{\mathrm{o}}$, is given accordingly by the ratio of permeabilities, i.e.,

$$\left(\frac{P_{\mathrm{eff}}}{P_{\mathrm{o}}}\right)_{\mathrm{Maxwell}} = \frac{1-\varphi}{1+\frac{\varphi}{2}} \tag{1.76}$$

where $P_{\mathrm{eff}} \equiv D_{\mathrm{eff}}S_{\mathrm{eff}}$. This is one of several scaling laws employed for gas permeation in polymer composites and has been introduced by Nielsen (1967), partially motivated by Maxwell's treatise on electricity and magnetism.[35] It is for this reason, the scaling law is referred to as *Maxwell's model* for gas permeation. The Maxwell model yields, as per Eq. (1.76), a decreasing gas permeability with increasing volume fraction φ of particles in the polymer composite, as shown in Figure 1.23.

We will now come to the shortcoming of the above scaling model. With Maxwell's model, we assume that the particles only displace the polymer molecules but do not affect the polymer phase in the vicinity of the particle. This assumption is challenged by experimental permeation results involving fumed silica (SiO_x) nanoparticles of 12 nm diameter that show strong deviations from the Maxwell model for PTMSP nanocomposites, Figure 1.23, for nitrogen, hydrogen, and propane.[36]

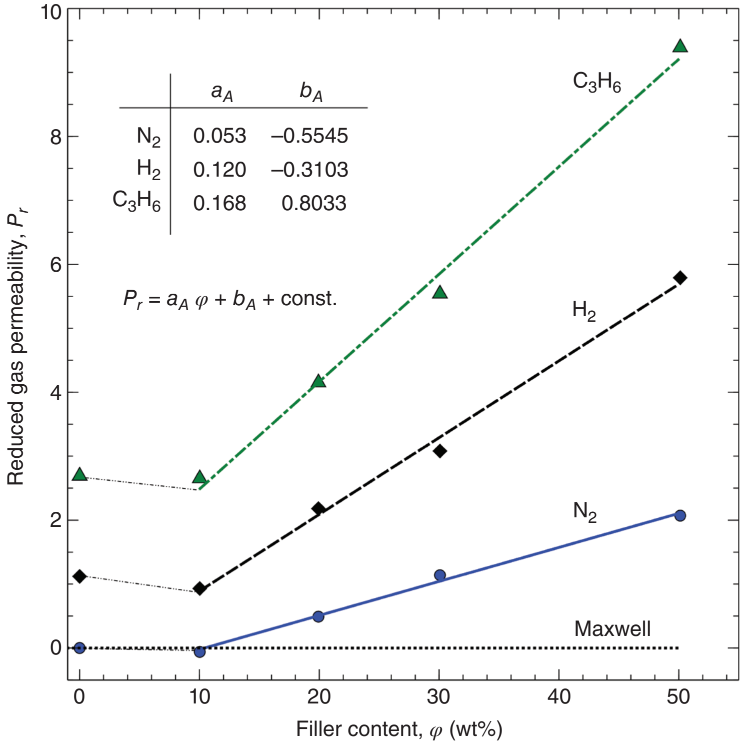

Figure 1.23 Linear fits of reduced relative gas permeabilities of N_2, H_2, and C_2H_6 through nanocomposite membranes of spherical SiO_x nanoparticles in PTMSP, as a function of the filler mass fraction, based on experimental data (adapted from [36]). The offset constant in the linear fit of the reduced permeation is provided in Eq. (1.78).

---

[35] L.E. Nielsen, J. Macromol. Sci. Part A Chem., **1**, 929 (1967). J.C. Maxwell, A. Treatise on Electricity and Magnetism, Oxford Univ. (Clarendon Press Series), Oxford, UK, **1** (1873).

[36] De Sitter et al., J. Memb. Sci., **278** (2006).

The data presented in Figure 1.23 are based on experimental permeation P_A results[36] involving the permeate A that, in relative notation, normalized by the permeability of nitrogen through the virgin homogeneous phase of PMTS, $P_{N_2}\big|_{\varphi=0}$, defines the relative permeability, $P_{\mathrm{rel}} \equiv P_A / P_{N_2}\big|_{\varphi=0}$. By subtracting the effect of gas transport screening silica particles, we obtain the reduced relative gas permeability of gas A, as

$$P_{r,A} \equiv P_{r,A} - \left(\frac{P_{\mathrm{eff},A}}{P_{\mathrm{o},A}}\right)_{\mathrm{Maxwell}} = \frac{P_A}{P_{N_2}\big|_{\varphi=0}} - \frac{1-\varphi}{1+\frac{\varphi}{2}} \tag{1.77}$$

that is presented in Figure 1.23 for N_2, H_2 and C_2H_6. The plot shows that there is a drop in permeation at low loading densities up to ~10 wt%, followed by a linear increase in the reduced permeability for $\varphi > 10$ wt%, i.e.,

$$P_{r,A}(\varphi) \approx a_A\varphi + b_A + \frac{P_A(\varphi)}{P_{N_2}(\varphi)}\bigg|_{\varphi=0} \left(\frac{1-\varphi^*}{1+\frac{\varphi^*}{2}}\right)^{-1} \tag{1.78}$$

with the gas and membrane-specific constants a_A and b_A, provided for N_2, H_2, and C_2H_6 in the table inset of Figure 1.23. The lengthy second offset in Eq. (1.78) originates from the initial drop of the permeability in Figure 1.23 up to a particle filler concentration of 10 wt%. The expression contains the inverted Maxwell function with filler content φ^*. By inspection of the data, we find that φ^* is around 25 wt%, i.e., significantly exceeding the 10 wt% for both hydrogen and propane. This is an indication of a complex composite system in the low filler content regime, with inhomogeneities of different sorts.

Thus, based on the gas permeation results presented in Figure 1.23, Maxwell's scaling law is not only off in magnitude, but also qualitatively, with an increase in gas permittivities above a critical particle loading weight percentage. Another interesting feature is that the permittivity of the heavier element, propane, surpasses that of nitrogen and even hydrogen. This surprising observation cannot be explained by diffusion – a mechanism that is molecule size-selective, but it can be explained by changing the sorption properties of the nanocomposite membrane with increasing particle loading density. Inspecting the case of SiO_x/PTMSP (Figure 1.23) closer, the permeation flux first decreases before it increases above ~10 wt% of the filler content. If we assume constant diffusivity ($D \neq f(\varphi)$), the increase in the permeability can be attributed to a change in the sorption coefficient S.[37] The question is how? We should consider that an interface between two solid/condensed substances can affect the bulk properties of each phase over a specific penetration depth δ, measured from the interface. This is illustrated in the sketch of Figure 1.24.

In Figure 1.24(a, b), a planar interface is contrasted to a spherical interface in that each affects the polymer bulk phase within a vicinity measured by the length scale δ. As a side note, not shown in the sketch, it shall be noted that high curvatures imposed by small particles can increase δ substantially, and thus, any interfacial effects would be even more

---

[37] We assume that there are no other effects, such as particle aggregation within the membrane or membrane crack formations by increasing the filler content in the membrane.

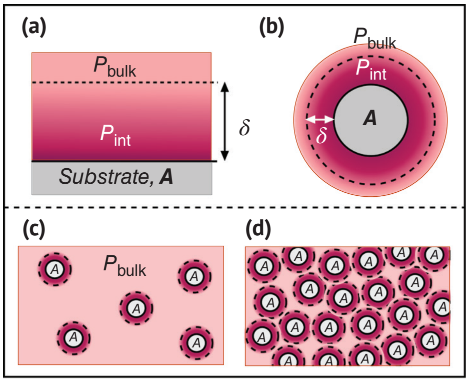

Figure 1.24 Interface between a solid substrate *A* and a polymer. Distinguished are the polymer bulk phase P_{bulk} from the gradually changing polymer phase P_{int} at the interface over a length scale δ. (a) planar geometry, (b) spherical geometry of substrate/nanoparticle material *A*. (c) Low filler density: The prominent transport phase is the P_{bulk} phase. (d) High filler density: The interfacial phase P_{int} is effective.

impactful. The polymer regime altered by the interface, labeled as P_{int}, varies locally from the bulk material and transport properties. Typically, the free volume in the polymer is increased, particularly for polymers with rigid backbones, such as PTMSP, which in turn can impact both the diffusion, as well as the sorption properties.[38] In regards to the permeation flux through nanocomposite membranes, the interfacial distorting impact is further enhanced with increasing filler content, as a more prominent portion of the transfer medium exhibits altered transport properties, illustrated in Figure 1.24(c, d).

In the case of PTMSP, a lower limit estimate of the range, δ, over which the bulk phase is altered by the presence of a SiO_x interface is ~100 nm. This is based on ultrathin film studies involving significantly more flexible polymer chains, such as polystyrene.[39] Thermally assisted, interfacial debonding studies of SiO_x nanoparticles from PTMSP revealed the presence of mobile polymer chains at the particle interface, which is an indication of enhanced free volume in the interfacial region and explains the bulk deviating permeation properties in PTMSP-silica composites.

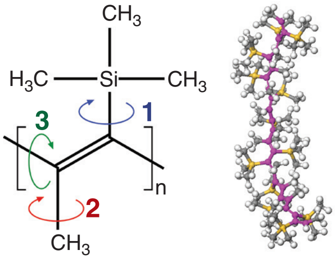

Figure 1.25 PTMSP chemical structure. Numbered are (1) the trimethyl-silyl rotation, (2) the methyl rotation, and (3) the backbone single bond rotation.

PTMSP, depicted in Figure 1.25, is a high free volume glassy polymer. It exhibits extraordinarily high gas permeability coefficients and high organic-vapor/permanent-gas selectivities. These unusual transport

---

[38] I. Pinnau and L.G. Toy, J. Membr. Sci., 116, 199 (1996); T.C. Merkel et al., Science, **296**, 519 (2002); L.S. Kocherlakota et al., Polymer, **54**, 5986 (2013).

[39] S. Sills et al., J. Chem. Phys., **120**, 5334 (2004).

properties in PTMSP are attributed to its high fractional free volume of about 0.34, caused by the inefficient chain packing involving rigid carbon-carbon double bonds, bulky trimethylsilyl, and methyl constituent groups, coupled with poor inter-chain cohesion. Comparing hydrogen with propene, we see that PTMSP can exhibit an inverted transfer rate if compared to the size of the molecules involved. This sorption-dominated selective transport behavior is often referred to as *reverse selective*.

Besides the generation of free volume, also local intrachain and sidechain mobilities have to be considered. Of the three rotational modes in PTMSP, depicted in Figure 1.25, the thermally active mode at room temperature is the rotation of methyl groups along the PTMSP backbone.[40] For PTMSP, interfacial constraints on local mobilities were, however, found to be insignificant compared to the free volume effect on the permeability.[40]

Typically, based on our common perception, we assume that the selective component transport of a gas mixture of A and B, where A shall be the smaller constituent, dictates that A transports faster through the membrane than B. In other words, we imply for the membrane's selectivity $\alpha_{A/B}$ follows the diffusivity ratio D_A/D_B, which, as we set it, exceeds unity. It is, however, important to note that the selectivity is not given by the diffusivities alone but determined by the permeability ratio, which also contains the ratio of the sorption properties, i.e.,

$$\alpha_{A/B} = \frac{P_A}{P_B} = \left(\frac{D_A}{D_B}\right)\left(\frac{S_A}{S_B}\right) \tag{1.79}$$

In the case of PTMSP and the binary mixture H_2/C_3O_6 that yields reverse selectivity, we find that the sorption properties dominate the diffusion properties that is $P_A/P_B < 1$, and thus, favor the larger constituent to flow faster through the membrane.

The example discussed here highlights the origin of the failure of Maxwell's classical scaling law for nanocomposite membranes, where the bulk phase is significantly altered due to interfacial effects. It illustrates the challenges in anticipating the shortcomings a scaling law can bear, as well as the complexity of pinpointing the specific origin for failure. The situation, particularly for PTMSP, is even more challenging than illustrated. We omitted the fact that PTMSP spontaneously degrades, shows swelling if exposed to some gases, such as carbon dioxide, and can exhibit a change in transport mechanism toward Knudsen diffusion and pressure-driven transport by forming pinholes.

1.8.2 Dimensional Constraints and Thermal Conductivity

As discussed, in heat transfer through solid materials, the bulk intrinsic property is the thermal conductivity, k_c. It determines how fast thermal energy can conduct through a material. Assuming isotropy and diffusive heat transfer with a constant thermal

---

[40] D.B. Knorr et al., J. Membr Sci., **346**, 302 (2010).

conduction coefficient k_c (i.e., $k_c \sim L^{\mathrm{o}}$), Fourier's law provides us for macroscopic systems with the following scaling law for the rate of heat conduction $Q = qA$ through area A:

$$Q = -k_c A \frac{\Delta T}{\Delta x} \sim L^{\mathrm{o}} L^2 \frac{L^{\mathrm{o}}}{L^1} = L \tag{1.80}$$

This scaling law breaks down, however, on the micrometer scale, as the intrinsic material property, k_c, becomes size-dependent. For 1D systems (quantum wires), with two of the dimensions confined to the nanoscale, the thermal conductivity is found to be well described by a power law of the form $k_c \sim L^{\beta}$ with $0 \geqq \beta < 1$, where for $\beta = 0$, we observe normal diffusion, and for $0 < \beta < 1$ anomalous diffusion. Consequently, the scaling law for heat conduction, introduced above with Eq. (1.80) for 3D bulk systems, changes from $Q \sim L$ to

$$Q \sim L^{\beta+1} \tag{1.81}$$

for 1D systems.

The power law exponent β for anomalous diffusion heat transfer has been theoretically estimated as 0.45 for a 1D chain of nonlinear oscillators (molecules or atoms).[41] β is found to be strongly dependent on the material and the conduction direction. For single-walled armchaired carbon nanotubes (CNT) with predominant heat transfer in the longitudinal direction at room temperature, Figure 1.26, values for β were found theoretically to be between 0.3 and 0.4.

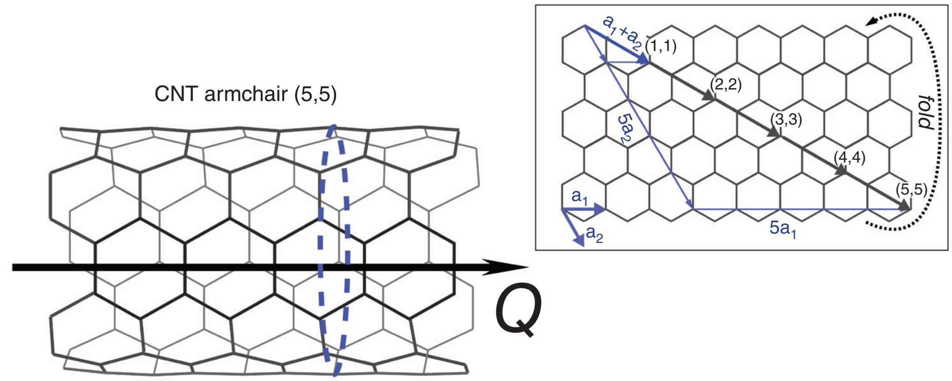

Figure 1.26 Single-walled (5,5) CNT with longitudinal heat conduction, as depicted with heat flow rate Q along the tube. $k_c \sim L^{\beta}$ with $\beta \approx 0.3$–0.4. The armchair (5,5) structure is explained with the graphene sheet in the inset. From the set of values $(n,m) = (5,5)$, we can determine the tube diameter $d = \frac{\sqrt{3}}{\pi} a_{cc} \sqrt{n^2 + nm + m^2}$, which yields for (5,5), 0.67 nm, based on a carbon-carbon bond length $a_{cc} = 0.14$ nm.

---

[41] S. Lepri et al., Phys. Rev. Lett., **78**, 1896 (1997).

A nanotube is a hexagonal network of carbon atoms that has been rolled up to make a seamless cylinder. Its structure and diameter are characterized by two integers, n and m. The integer pair (n,m), which is (5,5) in Figure 1.26, denotes the number of vectors $\vec{a}_1$ and $\vec{a}_2$ along two main directions in the honeycomb crystal lattice of graphene. For $m = 0$ and $n = m$, the nanotubes are called zigzag or armchair nanotubes, respectively. Otherwise, they are referred to as chiral. The diameter of a nanotube can be calculated from (n,m), according to

$$d = \frac{\sqrt{3}}{\pi} a_{cc} \sqrt{n^2 + nm + m^2} \tag{1.82}$$

Figure 1.27 provides one of the many (often disparate) simulation plots for the heat conduction coefficient as a function of the length of single-walled (10/10) CNT. If compared to the current literature, its extrapolated k_c value of around 6500 W/m · K for a nanotube of length $L = 1$ mm with $\beta = 0.3515$ (and prefactor 573.24) fits well with quantum mechanical theoretical work,[42] and the correction to data based on experimental work.[43] Based on these findings and in comparison with the macroscopic graphite (HOPG) k_c value of 1700 W/m · K, the heat conductivity for long CNTs exceeds the bulk value multiple times. An estimate for the determination of β is discussed in the Worked Problem below.

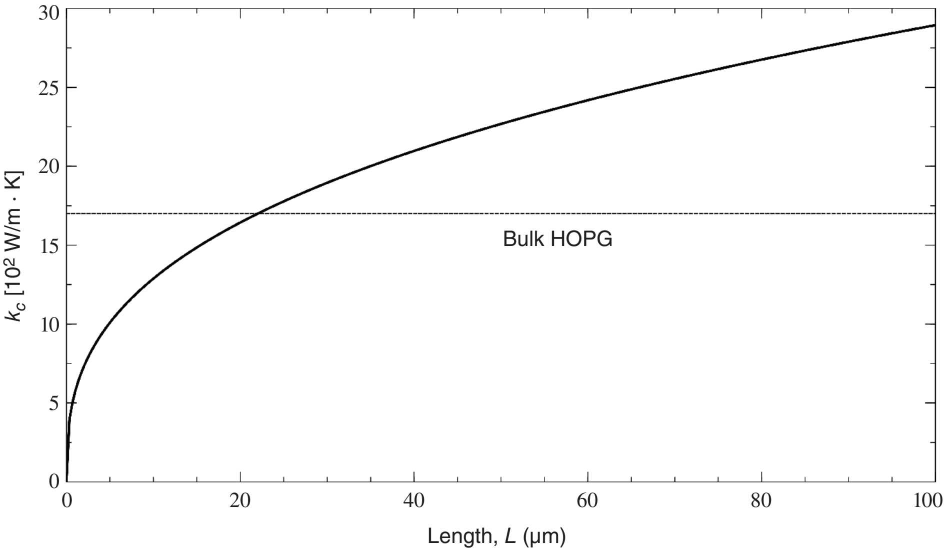

Figure 1.27 (5,5) Thermal conduction coefficient as function of the length of a single-walled (10,10) CNT. $k_c \sim L^{\beta}$ with $\beta \approx 0.35$.[44]

---

[42] D. Bruns et al., Phys. Rev. B, **101**, 195408 (2020).
[43] X. Zhang et al., Phys. Rev. Lett., **119,** 179601 (2017).
[44] G. Zhang et al., J. Chem. Phys., **123**, 114714 (2005).

The reason for the substantial increase in k_c in lower dimensions compared to the bulk is due to a decrease in the phonon scattering sites, and with it, a reduction in energy fluctuations. As some of the phonon scattering processes found in 3D are suppressed in 1D, the resistance to phonon motion is reduced, and heat conduction increases. For short tubes, however, prominent scattering at the tube ends results in an increase in the scattering sites and, thus, can yield a lower thermal conductivity compared to the bulk. At exactly what critical tube size L, k_c of the tube falls below the bulk value is still debated. Based on the $k_c(L)$ plot in Figure 1.27, it appears to occur around 20 μm. However, as per a recent more involved theoretical treatment[42] that yields a power law distorted thermal conductivity of the form

$$k_c = k_c^{\infty}/(1 + \lambda_{\text{eff}}/L), \tag{1.83}$$

the critical tube length is found at around 100 nm.

Another parameter that affects heat transfer in CNT is the tube diameter D and the temperature. In both cases, the thermal conductivity decreases when either of the two parameters is increased. Lastly, it shall be noted that a similar discussion on scaling for 2D systems (such as graphene), yields a thermal conductivity that exhibits a logarithmic dependence with size.

Worked Problem 1.8.3

Background: The chirality $\vec{c} = n\vec{a}_1 + m\vec{a}_2$ of the rolled-up sheet that results in a CNT is expressed by the pair (n,m), and the basis vectors $\vec{a}_1$ and $\vec{a}_2$. It is depicted here as well as in Figure 1.26 for $(n,m) = (5,5)$. In a Cartesian system $(\vec{e}_x, \vec{e}_y)$, the two basis vectors can be expressed as

$$\vec{a}_1 = a\left(\sqrt{3}a/2, -1/2\right) \text{ and } \vec{a}_2 = a\left(\sqrt{3}a/2, 1/2\right)$$

whereby we introduced and defined $a \equiv \sqrt{3}a_{c-c}$ with $a_{c-c} = 1.421$ Å, the shortest carbon-carbon distance. The diameter d of the CNT can be simply obtained from the chirality, as $d = |\vec{c}|/\pi$, and thus,

$$d = \frac{a}{\pi}\sqrt{n^2 + nm + m^2}$$

Problem: We shall estimate the thermal conductivity from the two limiting boundary cases, i.e., the 1D atom chain with $d = 0$ ($\beta = 0.45$) and the graphene sheet with $D = \infty$ ($k_c = 3500$–5000 W/m · K), and use the value of β for the (10,10) single wall CNT, discussed in the text.

Solution: For the armchair (10,10) CNT for which a power law exponent of $\beta = 0.3515$ was determined (see text), the diameter is obtained from the equation above, as

$$d_{(n,n)} = \frac{\sqrt{3}n}{\pi}a = \frac{3n}{\pi}a_{c-c} \xrightarrow[n=10]{} d_{(10,10)} = 1.36 \text{ nm}$$

An upper bound for β (d) is obtained from the 1D atom chain as $\beta_{1D} \approx 0.45$.

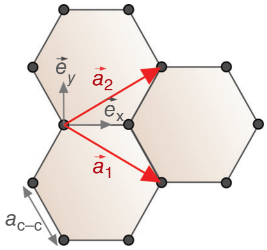

Figure P1.8.3a Graphene structural elements.

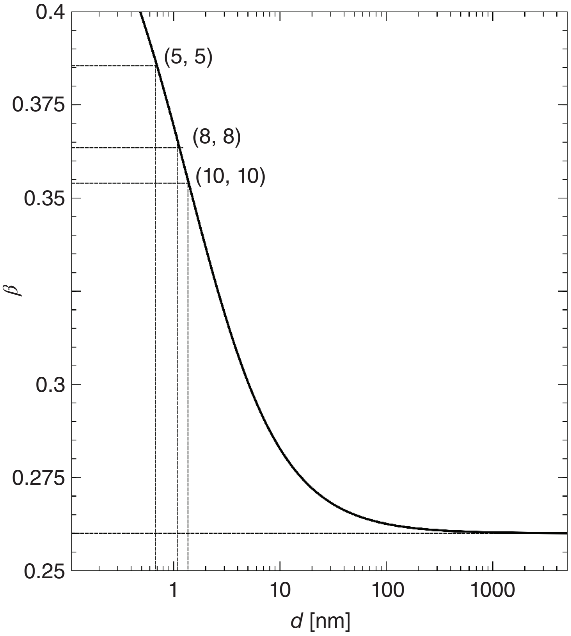

Figure P1.8.3b Power law coefficient as a function of the CNT length.

Next, we consider that for $d \to \infty$, the nanotube is converging into a graphene sheet, for which k_c is 3500–5000 W/m · K, i.e., lower than the one found for a long carbon nanowire (>6500 W/m · K). Hence, we can expect for β a lower bound value, which we shall denote as β_{2D}. A typical function in nature that smoothly connects limiting boundaries of that sort is

$$\beta = \beta_{2D} + \frac{\beta_{1D} - \beta_{2D}}{1 + \left(\frac{d}{d_{50}}\right)^n}$$

where d is the CNT diameter, and n and D_{50} are two fitting parameters. At d_{50}, β is in the middle of the two bound values, i.e., $\beta(d_{50}) = (\beta_{1D} - \beta_{2D})/2$. We set $n = 1$, as we have no justification to do otherwise in our rough estimate of β (d). We use the (10,10) CNT tube diameter of 1.36 nm for d_{50}, which yields for β_{2D} a value of 0.26. This value accommodates the thermal conductivity range provided for graphene. Also, the relative β value differences (see figure) between (5,5), (8.8), and (10,10) diameter CNTs are approximately matched by observation in the literature.

1.9 Organization and Outlook for Nanoscience and Nanotechnology

We commenced this introductory chapter on nanoscience and molecular engineering by exploring commonly held perceptions of our world and expressing opinions on the potential benefits of the nanoscale. Likewise, we recognized that a majority of mankind's technological progress involving molecules has been based on trial-and-error approaches, lacking, in many cases, a deductive rational approach toward engineering.

Following these inaugural observations, we meandered through the unique realm of lower dimensionalities and explored the mechanical, acoustic, thermal, and electronic properties of materials under constraints. In so doing, we differentiated between size constraints, interfacial constraints, and dimensional constraints, all of which, we found to impact our current perception of transport properties often expressed by empirically derived laws describing 3D bulk system responses. We critically assessed the scaling laws derived from bulk phenomenological observations and found them to be inadequate under the mentioned constraints. Specifically, we contrasted scaling law expectations with nanoscale observations and provided some background and explanations of why bulk perceptions of the world break down on the nanoscale.

In this final section of the chapter, we will provide a concise exploration of how the expansive field of nanoscience and its associated technologies can be classified, as well as the areas they currently impact or are expected to influence in the near future. We will refrain from revisiting the topic of molecular engineering, which we previously discussed in the first section of this chapter, where we emphasized the advantages of a deductive, rational approach over trial-and-error methods.

1.9.1 Classification of Nanoscience and Nanotechnology

A proper classification of aspects and fundamentals within science and technological disciplines is pivotal for streamlining a discipline toward education as well as integrating new findings into an existing framework so that its implications are most effective. Before we address the subclassification of nanoscience, it is essential to first examine its position within the current scientific landscape. Evidently, nanoscience is an interdisciplinary field that encompasses the three principal science disciplines: physics, chemistry, and biology. Given that physics serves as the foundational driver of nanoscience, we will begin by exploring its role within the expansive domain of physics.

Physics has been characterized within the first quarter of the 20th century by its underlying theories into classical mechanics, thermodynamics and statistical mechanics, electrodynamics, relativistic physics, and, quantum mechanics. Older branches of physics, such as optics and acoustics, were incorporated within these five principal branches. Considering the makeup of matter, another classification emerged over the past 50 years that differentiates between *atomistic physics, nuclear physics, quantum physics, relativistic physics*, and *cosmology*.

Atomistic physics focuses on the structure of atoms, electronic energy states, atom-atom interactions, and the interplay involving electric and magnetic fields. By extension considering the molecule, i.e., covalently bound atoms, *molecular physics* focuses on the physical properties of molecules and molecular dynamics. The solely microscopic perspective of matter taken by atomistic and molecular physics is expanded to the macroscopic world via *solid-state physics* or, more general, *condensed matter physics*.

Condensed matter physics explores the connection between the atomistic structure of matter and its macroscopic phase (solid, liquid, and gas) properties. The forces that are of foremost interest in condensed matter physics and that differentiate it from *particle physics* and *astrophysics* are generally of EM nature found between atoms, when forming molecules, and between molecules in particle condensed phase systems. A subdiscipline of condensed matter physics is the field of *mesoscopic physics*, which considers predominantly phase systems on the submicrometer scale and includes aspects of nanoscience below the 100 nm scale.

While mesoscopic physics is loosely defined as addressing size-related issues that deviate from bulk phenomenological descriptions, it has focused since Rolf Landauer and Markus Büttiker in 1957 and 1990,[45] respectively, primarily on electronic properties of size and dimensionally confined metals and semiconductors. Taking a more general perspective, mesoscopic physics considers transport phenomena with classically modified or exchanged fluctuations underlying particle propagation. For instance, in the case of electron transport through a conductive media composed of quantum particles (artificial atoms), sintered together, quantum fluctuations dominate thermal fluctuations. Thus, quantum effects can bring forward the phase characteristics of electrons and, with it, invite phase coherence. Classically, in a macroscopic system, electron scattering at the crystal lattice (electron-phonon scattering), between electrons and impurities and defects within the crystal lattice, makes the electrons behave like incoherently moving particles. By considering, however, a system in which electronic energy levels exceed thermal noise ($k_B T$), the electron wave character emerges allowing electrons to move coherently. Such mesoscopic behavior comes into play when critical dimensions (e.g., system particle dimensions) are on the order of or smaller than the relevant effective length scale (e.g., the distance between scattering events).

Nanoscience significantly expanded the scope of mesoscopic physics on the sub-100-nm scale, not only by encompassing molecular condensed systems and expanding to organic and biological materials but also by incorporating aspects of surface and interfacial sciences. Entropic transport aspects, as well as unique phase behavior and transitions involving molecules under confinement, became the cornerstones of this new science field that found traction toward the end of the 20th century and has shown a substantial impact on emerging technologies within the first two decades of this century. This was elucidated at the beginning of this chapter when we addressed the combined deductive rational nanoscience and molecular engineering approach to combat COVID-19 with a heterogeneous molecular nanosystem. This fourth generational stage of nanotechnological product development followed by the development of first passive nanostructures (e.g., nanoparticles), second active nanostructures (e.g., amplifiers), and third 3D nanosystems (e.g., guided self-assembly), marks the beginning of the diffusion of this new technology into emerging industries and services.[46]

Having pinpointed the area in which nanoscience can be placed within physical sciences, we are now equipped to attempt a classification of this multidisciplinary field. We recognize the importance of external physical constraints, as well as the prominent properties that are affected. We can differentiate between two principle classes of constraints, namely

- **i.** *external* constraints that include *dimensional* constraints and *interfacial* constraints and
- **ii.** *internal* constraints comprised of atomistic and molecular *structural* constraints and *entropic* constraints.

---

[45] R. Landauer, IBM J. Res. Develop., **1**, 223 (1957); M. Büttiker, Phys. Rev. B, **41**, 7906 (1990).

[46] M.C. Roco, J. Nanopart. Res., **25**, 197 (2023).

Table 1.6 Topics related to transport phenomena under nanoconstraints.

Transport phenomena	**Constraints**			
	Internal		***External***	
	Dimensional	***Interfacial***	***Structural***	***Entropic***
Acoustic	wavelength vs. object size	phonon vibrations	wave modification	entanglement entropy, phonon-phonon scattering
Electronic	scattering length vs. object size	electronic band structure	wave modification	spin coupling, quantum entanglement, quantum fluctuation
Energetic	fluctuations vs. object size	vibrational modes	resistance	mode coupling, thermal fluctuation
Mass	permeate size vs. transport dimension	concentration gradient	resistance	permeate clustering
Momentum	mean free path vs. system dimension	pressure fluctuations	boundary layer dominance	cooperative motion (“structuring”)

The prominent properties affected by the mentioned constraints belong to the five transport phenomena, namely, *acoustic, electronic, energetic* (heat), *mass*, and *momentum* transport. In Table 1.6, the four subclasses of constraints are contrasted to the five transport phenomena with some specific input on critical size and impact.

Some of the aspects that Table 1.6 eludes to, have been addressed in this chapter, such as critical size considerations, when we compared the electron wavelength to the object size in electronic systems, dimensional constraints, when we discussed the thermal conductivity increase in carbon nanotubes and the decrease in scattering sites, and, interfacial effects, in our discussion of polymer confinement in nanocomposites in reference to gas diffusive mass transport, and our discussion of shear momentum transport within liquid boundary layers. Discussions on aspects related to structural and entropic confinements are still outstanding and will be picked up in later chapters. In particular, the electronic nature of matter will be investigated over several chapters, starting with the building block, the atom, the wave characteristics of particles, and the effect of dimensionality of electronic transport that will finally culminate in a physical understanding of modern technological applications, such as diodes and solar cells. We will explore the electronic structure of molecules, their degrees of freedom, and their interactions, which brings forward the aspect of entropy. Entropic constraints are found to affect the collective behavior of the transport “intrinsic elements.” We shall see that the term entropy is not always used in an

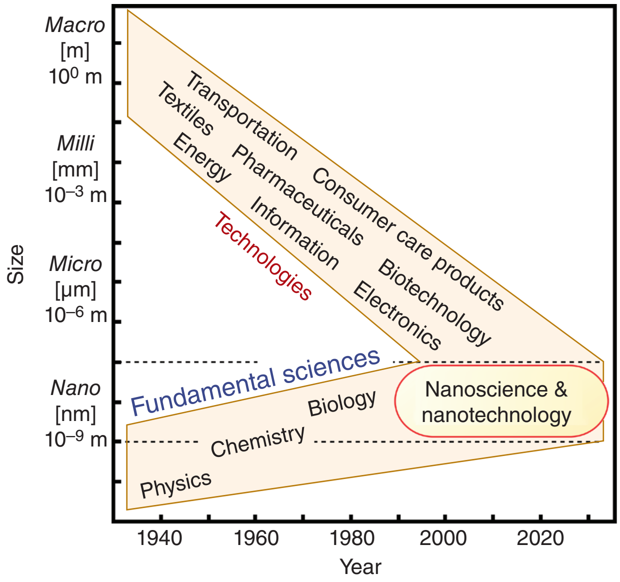

Figure 1.28 Technologies meet fundamental sciences on the nanoscale.

energy dissipative context but also as structural force when we discuss cooperative entropy or entanglement entropy.

Today, nanoscience and nanotechnology manifest the culminating interface, where industrial needs converge with fundamental sciences involving the mesoscale between atomistic and phenomenological theories. As illustrated in Figure 1.28, nanoscience research, starting from physics, chemistry, and biology, provides an important and improved understanding of nature on the mesoscale that has benefitted emerging technologies in electronics, biotechnology, pharmaceuticals, and energy-related disciplines since the beginning of this millennium.

Study Problems to Chapter 1

1.1 Nanometer Scale

The length of a C—C single bond in graphene is 1.42 Å (1 Å = 10^{-10} m). Determine

- **a.** the area of a C—C hexagon in graphene in nm^2,
- **b.** the number density of carbon atoms in a graphene layer in nm^{-2},
- **c.** the surface density of a single graphene layer in ng/cm^2 (1 ng = 10^{-9} g), and
- **d.** the density of bilayer graphene in g/cm^3, assuming a layer distance of 0.335 nm.

1.2 Molecular Engineering

- **a.** Briefly describe the difference between *trial-and-error-based* engineering and *deductive rational* molecular engineering.
- **b.** List at least two pros and cons for each of the two engineering approaches mentioned in (a).

c. The rubber vulcanization process by Charles Goodyear belongs to which one of the two named engineering approaches? What is the fundamental aspect of it?
d. Provide from your knowledge or the literature one or more examples of successful trial-and-error approaches.
e. Name one of the most striking examples of molecular engineering that was paired with nanotechnology.

1.3 Apparent Material Behavior

What do we understand under the term apparent material behavior and why is it important for nanoscience and nanotechnology?

1.4 Dimensionality

Provide examples of the following dimensionalities: 0D, 1D, 2D.

1.5 Dimensionality and Transport Effects

How can constrained dimensions affect the transport properties? Offer a few examples.

1.6 Perfect Liquids and Solids

When describing rheological material behavior, we typically classify the possible responses to external forces. In that context, rheological solid-like and liquid-like behaviors should neither be confused with the thermodynamically described intrinsic solid nor be confused with the liquid phase. How would you formally describe solid-like and liquid-like behavior, and why do you think it is of greater importance when moving to the nanoscale?

1.7 Atomic Force Microscopy – Solid-like Deflective Response

An AFM, also known as scanning force microscope, is a nanoscopic imaging and force-measuring tool widely used in nanoscience-related research and quality control in nanotechnological applications. It consists of a cantilever with an integrated "atomically" sharp conical or pyramidal tip, as depicted. The lever material is either silicon or silicon nitride with typical length dimensions of a bar-shaped lever of $100 \times 10 \times 0.5$ μm (length, l, width, w, thickness, d). The deflection of the lever is measured with a focused light (low-power laser) beam. The AFM force sensitivity is on the order of 0.1 nN. The lever spring constants can be determined from

$$\text{normal z-bending: } k_z = \frac{Ewd^3}{4l^3}$$

$$\text{lateral x-bending: } k_x = \frac{Ew^3d}{4l^3}$$

$$\text{torsional bending: } k_t = \frac{Gwd}{3lr^2}$$

based on the dimensions and the elastic material properties (E Young's modulus, G shear modulus) of a bar-shaped cantilever. The corresponding forces are obtained as $F_\xi = k_\xi \, \Delta\xi$ ($\xi = z, x, t$).

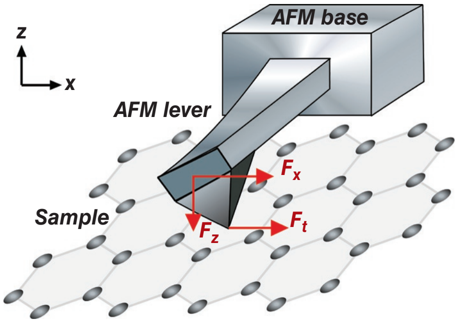

Figure SP1-1 Cantilever and forces

Determine the three spring constants for a lever of dimension, $100 \times 10 \times 0.6$ μm, for a silicon lever with $E = 1.65 \times 10^{11}$ Pa and a Poisson ratio ν of 0.65. The integrated tip shall have a length (radius) r of 12.5 μm.

1.8 Activation Energy for Viscous Flow of Simple Fluids

Determine the activation energy for viscous flow of water between 1 °C and 90 °C at the normal atmospheric pressure (101.3 kPa) using the NIST database and compare your result to the hydrogen bond strength in bulk water of 7.95 kJ/mol, as per K. A. T. Silverstein, A. D. J. Haymet, and Ken A. Dill, J. Am. Chem. Soc., **122**, 8037–8041 (2000).

1.9 Activation Energy in Polymer Melts of High Molecular Weight

Investigate the viscous response in high molecular weight polystyrene (MW: 135k) close to the glass transition at $T_g \approx 100\ ^\circ$C and the melting transition at $T_m \approx 240\ ^\circ$C, given (Table 1.7 below) viscosities values at and between the two transition values, by answering the following question:

- **a.** Does the viscosity follow an Arrhenius behavior if plotted versus the inverse absolute temperature?
- **b.** Determine the activation energy in kcal/mol at $T_1 = 100\ ^\circ$C and $T_2 = 240\ ^\circ$C from an Arrhenius-like data plot, i.e., ln $\eta(1/T\ [\mathrm{K}])$.
- **c.** Discuss your result in light of the following molecule-specific energies:[47]
  - ○ γ-relaxation: ~8 kcal/mol (phenyl rotation)
  - ○ β-relaxation: ~18 kcal/mol (isolated crankshaft motion in backbones)
  - ○ α-relaxation: ~90 kcal/mol (cooperative crankshaft motion)

Table 1.7 Viscosity values in the melt phase of polystyrene (MW 135k).

Temperature, T [°C]	Viscosity, η [Pa · s]	Temperature, T [°C]	Viscosity, η [Pa · s]
100	19,131.797	180	46.074
120	1822.381	200	24.019
140	354.328	220	14.562
160	109.427	240	9.846

---

[47] J. Knorr et al., J. Chem Phys., **129**, 074504 (2008).

1.10 Melting Temperature of Low Molecular Weight Polystyrene

Estimate the melting temperature in °C of low molecular weight polystyrene (MW 35k), based on the averaged viscosity-temperature fit

$$\ln\eta = 0.0059e^{3075.5(1/T)} \text{ with } \eta \text{ [Pa} \cdot \text{s] and } T\text{[K]}$$

to a wide variety of experimental viscosity data provided above 110 °C. Assume that the activation energy at the melting point is 20 kcal/mol, i.e., matched approximately by the backbone crankshaft rotational energy of polystyrene.

1.11 Electrical Conductance and Resistance

Provide the definitions for electrical conductance, resistance, and conductivity as well as the electric resistivity.

1.12 Heat Transfer of Molecular Gases

Comparing the relevant heat transfer coefficients of two quiescent gases at standard ambient conditions based on their molecular weight and size, which one is more efficient in conducting heat – the gas composed of smaller or larger molecules? Support your answer by calculating and comparing k_c at 300 K for

a. argon (Ar) and helium (He), and,

b. carbon dioxide (CO_2) and ammonia (NH_3).

Use appropriate equations to solve these problems and compare your results to literature data found in Table 1.3. Discuss your findings and address with appropriate disagreements.

1.13 Molecular Velocities in Gases

Derive analytically the

a. Maximum velocity, $v_{\max}$ (Ans.: $v_{\max} = \sqrt{2k_BT/m}$)

b. Average velocity, $\langle v\rangle$ (Ans.: $\langle v\rangle = \sqrt{8k_BT/\pi m}$)

c. The *rms* velocity, v_{rms} (Ans.: $v_{\text{rms}} = \sqrt{3k_BT/m}$)
for a gas system based on the Maxwell-Boltzmann velocity distribution $f(v)$.

d. Plot the Maxwell-Boltzmann velocity distribution at 300 K for CO_2 and CO, and include graphically the probability density functions $f(v)$ according to the three velocities.

e. Lastly, determine the fractions of CO gas molecules moving with $v_{\max}$ $\langle v\rangle$, or v_{rms}, and, the corresponding numbers of molecules for three velocities for 1 mole of gas.

Background:

The maximum velocity $v_{\max}$ stands for the most probable velocity magnitude of all system gas molecules. It is obtained from

$$\left.\frac{\mathrm{d}f(v)}{\mathrm{d}v}\right|_{v_{\max}} = 0$$

The average velocity $\langle v \rangle$ reflects the mean velocity magnitude for all molecules in the gas. It is computed as

$$\langle v \rangle = \int_0^\infty v f(v)\, dv$$

The *rms* velocity v_{rms} measures the speed at which all the molecules have the same total kinetic energy compared to their actual speed. It is obtained from

$$v_{\mathrm{rms}}^2 = \int_0^\infty v^2 f(v)\, dv$$

Hint: Use for the determination of v_{rms} the following identity:

$$\int_0^\infty x^{2n} \mathrm{e}^{-x^2/a^2} dx = \sqrt{\pi} \frac{(2n)!}{n!} \left(\frac{a}{2}\right)^{2n+1}$$

1.14 Average Relative Velocity in a Gas

A quantity of great importance in determining the mean free path of molecules in a gas is the *average relative velocity* $\langle v_{\mathrm{rel}} \rangle = \left| \left\langle \vec{v}_{\mathrm{rel}} \right\rangle \right|$. For the determination of the mean free path, one has to take into account that the system velocity to which the molecular speed is compared is not given by the boundary (i.e., contrasted to the perspective of a stationary observer) but the average speed of the molecular counterparts (i.e., related to the reference frame of a moving observer). That said, consider the relative velocity between a molecule of speed $\vec{v}$, with an arbitrarily unrelated molecule of velocity $\vec{v}'$, both speeds are from the perspective of the system boundary, and thus,

$$\vec{v}_{\mathrm{rel}} = \vec{v} - \vec{v}'$$

and determine the average relative velocity. (Ans.: $\langle v_{\mathrm{rel}} \rangle = \sqrt{2} \langle v \rangle$)

Hint: Note that for uncoordinated arbitrary motions of particles, $\left\langle \vec{v} \cdot \vec{v}' \right\rangle = 0$.

1.15 Mean Free Path

As per definition, the mean free path λ manifests the average distance between collisions for a gas molecule in a gas system. In an ideal gas, these collisions are elastic, and thus, there is no energy dissipated. This allows us to picture molecules as rigid particles. For simplicity, they shall be spherical with diameter d. For two molecules to collide, they have to be a distance d apart, measured from their centers of mass. Hence, at the collision distance d, we can infer an effective collision area of $A = \pi d^2$. Consider now a corridor ("cylinder") of cross-sectional area A with molecules distributed within the corridor given by the molecular number density ρ_N of the gas under given temperature and pressure conditions. The molecules are only represented by their position without size, as the size is already captured by the conduit dimension. Now the cross-section shall move over time t with the average relative velocity $\langle v_{\mathrm{rel}} \rangle$. Determine analytically with the parameters provided

a. the distance traveled in terms of the average velocity $\langle v \rangle$,
b. the volume of interaction, in terms of the average relative velocity, and
c. the mean free path. (Ans.: $\lambda = \dfrac{1}{\sqrt{2} \rho_N \pi d^2}$).

1.16 Bulk Behavioral Limitation Based on System Size

Consider a system size L of 100 nm filled with oxygen gas at ambient standard conditions (25 °C and 101 kPa). (a) Determine if, under these confining conditions, oxygen still behaves bulk-like. (b) Calculate the thermal conductivity. In the case of a necessary Knudsen correction, consider $\beta = 1.5$.

1.17 Electron Number Density

With knowledge of the mass number A and the valency of the atoms making up a pure metal, derive the following analytical expression

$$n = \frac{N_A(\text{atoms})(Z - Z_{\text{core}})\rho}{A \times [\text{g/mol}]}$$

for the electron number density n.

1.18 Electron Number Density of Selected Metals

Calculate the electron number densities for Ag, Au, and Al based on their valencies, mass densities, and mass numbers.

1.19 Electron Mobility and Electrical Conductivity of Gold

i. Based on gold's (Au) electron relaxation time $\tau_m = 36.8$ fs (femtoseconds) at an unknown temperature and effective mass ratio $m^* = m/m_e = 1.1$, where m_e stands for the electron rest mass, and the following expression

$$\mu_e = \frac{e}{m}\tau_m$$

determine the value for the electron mobility, μ_e.

ii. The electron mobility is typically defined by

$$v_d \equiv \mu_e E$$

where v_d stands for the electron drift velocity in an electric field E. Show with physical unit matching that the two expressions in (i) and (ii) are equivalent, regarding the electron mobility.

iii. With the electron mobility value from (i) and the electron number density n_e from the prior problem determine the electrical conductivity σ_e in units of Siemens per meter.

iv. The electric resistivity ρ_e of Au can be linearly fit to the temperature T, within 200 K and 500 K,

$$\rho_e\left[10^{-8}\ \Omega \cdot \text{m}\right] = 0.0084\left[\frac{\Omega \cdot \text{m}}{\text{K}}\right]T\,[\text{K}] - 0.2343\left[10^{-8}\ \Omega \cdot \text{m}\right]$$

Use this fit to determine the temperature for which the electrical conductivity in (iii) was determined.

1.20 Backscattering in Carbon Nanotubes

The mean free path of backscattering λ_B in a SWCNT of length $L = 1$ μm shall be investigated based on the provided current-voltage (I-V) characteristics (see plot below) at high fields (low resistant contacts to the electron reservoirs). Consider the scattering probability to be constant (i.e., independent on V). Furthermore, the transport shall be assumed ballistic for $L \gg \lambda_B$ within 0.3 V.

a. We start the problem with some general questions:
  - **i.** Is the temperature within the SWCNT constant during current flow for an applied voltage within the linear regime of the I-V curve?
  - **ii.** Within the linear regime of the I-V curve, the electrical resistance along the SWCNT originates from energy dissipations within the wire or within the connected electron reservoirs? This question is related to (i).
  - **iii.** If we assume ideal contacts, what could be the reason for the current saturation for large voltages (>5 V)?

b. Determine the backscattering length λ_B according to the linear regime obtainable from the presented I-V curve. Note that SWCNT possess two subbands.

1.21 Phase Discrepancy Between Waves

Consider two electron waves entering a system with intensities I_1 and I_2. At the exit of the system, their superimposed intensity is measured at a particular location on a screen. Originally, the two superimposed waves leaving the system are uncorrelated ($\delta = 90$ deg., or more general: $\delta = (2n + 1)\pi/2$, $n = 0, \pm 1, \pm 2, \ldots,$). After the path (relative distance to screen) of one wave has been altered, the measured superposition intensity on the screen is altered by a factor $1/\xi$ from its original value.

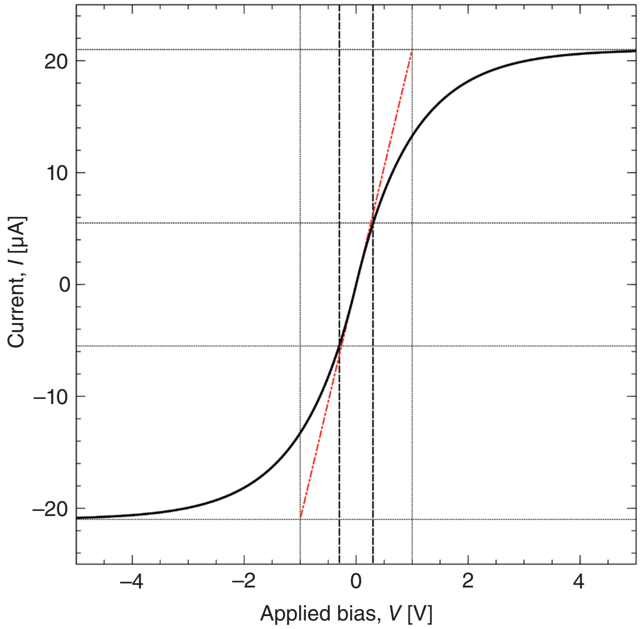

Figure SP1-2 I-V characteristic of multiwall CNT fit to literature data.[48]

---

[48] Z. Yao et al., Phys. Rev. Lett., **84**, 2941 (2000).

i. Describe analytically the phase lag situation described here using the intensities I_1 and I_2 of the single beams, as well as the factor ξ.

ii. Determine the induced phase shift in degrees, having altered the original path, for $\xi = 2$, and $I_1/I_2 = 1/3$.

iii. Assume that $I_1 = I_2$, and a change to the path so that the two waves are in-phase (perfectly correlated). How big is $1/\xi$?

1.22 Quantum Conductance

A 1D quantum wire exhibits a conductance of 29.8 mS. Determine the number of modes of perfect transmission probability through which electrons can travel.

1.23 Charging of a Quantum Dot

Estimate in electron volts the required energy for charging an arsenide QD that carries $n = 5$ electrons with an additional electron. Given is a charge polarization toward the gate of $\sim 10^{-19}$ C, caused by the existing charges on the QD, and the material and geometry-specific QD capacitance of 7×10^{-18} F.

1.24 2D vs. 3D Acoustic Waves

What is one of the main challenges for acoustic wave pulse submissions in 2D?

1.25 1D Acoustic Wave

The displacement of a string of length L follows the 1D acoustic wave equation with the fixed-end boundary condition $y(0,t) = 0$ and $y(L,t) = 0$ and the initial condition

$$y(x,0) = \sin\left(\frac{2\pi}{L}x\right)\cos\left(\frac{2\pi}{L}x\right)$$

with $\dfrac{\partial y(x,0)}{\partial t} = 0$. Derive the resulting displacement of

$$y(x,t) = \frac{1}{2}\sin\left(\frac{4\pi}{L}x\right)\cos\left(\frac{4\pi}{L}vt\right).$$

1.26 Electromagnetic Planar Wave and Phonon Dispersion Relation

Consider the 1D wave equation with the phase velocity c (speed of light) for the EM planar wave $\vec{E}(z,t)$

$$\vec{E}(z,t) = \vec{E}_o e^{i(kz-\omega t)}$$

where $k = 2\pi/\lambda$ is the wave number, and $\omega = 2\pi\nu$ is the circular frequency. Find the relationship between the ω and k, also known as the *phonon dispersion relation*. Details about the 1D wave equation are provided in Appendix A.3.

1.27 Electron Particle Wave

To extend the wave equation to particle waves, we have to add an energy term to the wave equation that considers the nonzero rest mass m_o of the particle (electron), i.e.,

$$\frac{\partial^2}{\partial x^2}\psi(x,t) = \frac{1}{c^2}\frac{\partial^2}{dt^2}\psi(x,t) + \frac{m_o c^2}{\hbar^2}\psi(x,t)$$

where c and $\hbar$ stand for the speed of light and the Planck constant divided by 2π, respectively. We again assume a planar wave moving in the x-direction, i.e.,

$$\psi(z,t) = Ae^{\frac{i}{\hbar}(pz - Et)}$$

where A is a constant, p is the linear momentum, and E is the particle energy. The momentum and energy of the particle are related to the wave number k and the circular frequency ω via

$$p = \hbar k$$
$$E = \hbar\omega$$

Determine the relationship between the ω and k, also known as the *particle dispersion relation*. Provide a comparative sketch of $\omega(k)$ for photon waves and particle waves. For the photon wave, consider the earlier EM wave problem.

1.28 Volume Fraction and Polymer Nanocomposite of Cuboidal Impermeable Particles

Consider instead of spherical particles, cuboidal particles of aspect ratio $\alpha = w/l$, where w represents the width of the square particle surface that is oriented perpendicular to the flux direction, and l is the cuboidal length along the flux direction.

a. Derive the Niessen extension of the Maxwell equation for nonspherical particles, which is

$$\frac{P_{\text{eff}}}{P_{\text{o}}} = \frac{1 - \varphi}{1 + \alpha\left(\frac{\varphi}{2}\right)}.$$

b. Plot the Niessen extension for $a = 0.5$, 1, 2 and 7.

1.29 Volume Fraction and Polymer Composites with Permeable Dispersed Phases

A further extension of Maxwell's model is required if the dispersed phases are permeable to the permeates. We shall label the permeability of the dispersed phases as P_d. The following equation that addresses the permeability of the dispersed phases has been introduced by Lewis and Nielsen, as

$$\frac{P_{\text{eff}}}{P_{\text{o}}} = \frac{1 + \frac{2\varphi(P_d - P_{\text{o}})}{P_d + 2P_{\text{o}}}}{1 - \frac{\psi\varphi(P_d - P_{\text{o}})}{P_d + 2P_{\text{o}}}};\ \text{with}\ \psi \equiv 1 + \left(\frac{1 - \varphi_m}{\varphi_m^2}\right)\varphi.$$

The additional volume fraction parameter φ_m stands for the maximum packing fraction, which is unity for a system that can pack void-free.

Show that the Lewis–Nielsen equation reduces to Maxwell's equation if we assume perfect packing of impermeable dispersed phases.

1.30 Permeability of Hydrogen Through Nanocomposite PTMSP Membrane

Provided are the reduced gas parameters $a_A = 0.120$ and $b_A = -0.3103$ of $A = H_2$ (hydrogen) that determine the reduced gas permeability P_r through PTMSP/SiO_x, as a function of the particle wt %, and, the permeability values of nitrogen (N_2) of 3800 barrer and hydrogen (H_2) of 10300 barrer through a virgin (particle-free) PTMSP membrane. Determine the permeability of H_2 though PTMSP/SiO_x for $\varphi = 30$ wt %. As an estimate, you may assume that the original drop in permeability from zero to 10 % filler content, follows the Maxwell equation.

$1 \text{ barrer} = 1 \text{ mol/(m s Pa)}$ in SI units.